NASA-CR-203875

The spectral and statistical properties of turbulence generated by a vortex/blade-tip interaction

Final technical report to NASA Langley on research performed under the grant NAG-1-1539 entitled *Flow structure generated by perpendicular blade–vortex interaction and implications for helicopter noise prediction* for the period ending 18th January 1997

William J. Devenport (Principal Investigator)
Kenneth S. Wittmer (Research Associate)
Christian W. Wenger (Undergraduate Researcher)

Departmant of Aerospace and Ocean Engineering
Virginia Polytechnic Institute and State University
Blacksburg, VA 24061

The spectral and statistical properties of turbulence generated by a vortex/blade-tip interaction

William J. Devenport (Principal Investigator)
Kenneth S. Wittmer (Research Associate)
Christian W. Wenger (Undergraduate Researcher)

(Abstract)

The perpendicular interaction of a streamwise vortex with the tip of a lifting blade was studied in incompressible flow to provide information useful to the accurate prediction of helicopter rotor noise and the understanding of vortex dominated turbulent flows. The vortex passed 0.3 chord lengths to the suction side of the blade tip, providing a weak interaction. Single and two-point turbulence measurements were made using sub-miniature four sensor hot-wire probes 15 chord lengths downstream of the blade trailing edge; revealing the mean velocity and Reynolds stress tensor distributions of the turbulence, as well as its spanwise length scales as a function of frequency.

The single point measurements show the flow downstream of the blade to be dominated by the interaction of the original tip vortex and the vortex shed by the blade. These vortices rotate about each other under their mutual induction, winding up the turbulent wakes of the blades. This interaction between the vortices appears to be the source of new turbulence in their cores and in the region between them. This turbulence appears to be responsible for some decay in the core of the original vortex, not seen when the blade is removed. The region between the vortices is not only a region of comparatively large stresses, but also one of intense turbulence production. Velocity autospectra measured near its center suggests the presence quasi-periodic large eddies with axes roughly parallel to a line joining the vortex cores.

Detailed two-point measurements were made on a series of spanwise cuts through the flow so as to reveal the turbulence scales as they would be seen along the span of an intersecting airfoil. The measurements were made over a range of probe separations that enabled them to be analyzed not only in terms of coherence and phase spectra but also in terms of wave-number frequency (k-ω) spectra, computed by transforming the measured cross-spectra with respect to the spanwise separation of the probes. These data clearly show the influence of the coherent eddies in the spiral wake and the turbulent region between the cores. These eddies produce distinct peaks in the upwash velocity k-ω spectra, and strong anisotropy manifested both in the decay of the k-ω spectrum at larger wave-numbers and in differences between the k-ω spectra of different components. None of these features are represented in the von Karman spectrum for isotropic turbulence that is often used in broadband noise computations. Wave-number frequency spectra measured in the cores

appear to show some evidence that the turbulence outside sets up core waves, as has previously been hypothesized. These spectra also provide for the first time a truly objective method for distinguishing velocity fluctuations produced by core wandering from other motions.

Other publications produced under this grant

This report describes work done in the final year of a three year research grant. The following is a complete list of other reports and publications produced under this grant including all results from the first two years.

NASA Reports

K. S. Wittmer and W. J. Devenport. Flow structure generated by perpendicular blade–vortex interaction and implications for helicopter noise prediction. Technical report to NASA Langley on research performed under the grant NAG-1-1539 for the period ending 18th January 1996.

Journal Publications

K. S. Wittmer, W. J. Devenport, and M. C. Rife. Perpendicular blade vortex interaction. *AIAA Journal*, 33(9):1667–1674, September 1995.

K. S. Wittmer, W. J. Devenport, J. S. Zsoldos, and G. J. Follin. A four-sensor hot-wire probe system for three-component velocity measurements. Under review by *Experiments in Fluids*. December 1996.

K. S. Wittmer and W. J. Devenport. Turbulence structure resulting from a vortex/blade-tip interaction. Submitted to *AIAA Journal*, February 1997.

K. S. Wittmer and W. J. Devenport. Perpendicular airfoil–vortex interaction. Part 1: overall structure. In preparation for *AIAA Journal*, February 1997.

K. S. Wittmer and W. J. Devenport. Perpendicular airfoil–vortex interaction. Part 2: vortex core structure. In preparation for *AIAA Journal*, February 1997.

Conference Publications

W. J. Devenport, C. M. Wenger, S. A. L. Glegg, and J. A. Miranda. Wave-number frequency spectra of turbulence in a lifting wake for broadband noise prediction. AIAA Paper 97-1699, May 1997.

K. S. Wittmer and W. J. Devenport. Turbulence structure resulting from a vortex/blade-tip interaction. AIAA Paper 97-0047, January 1997.

K. S. Wittmer and W. J. Devenport. Turbulence structure resulting from a perpendicular airfoil–vortex interaction. AIAA Paper 96-2014, June 1996.

K. S. Wittmer and W. J. Devenport. Interaction of a streamwise vortex with a full–span blade. AIAA Paper 95-2214, June 1995.

C. M. Weisser. Controlling trailing tip vortices. AIAA 1995 Mid-Atlantic Student Conference, George Washington University, NASA Langley Campus, April 1995.

Academic Publications

K. S. Wittmer, *Turbulent flowfield downstream of a perpendicular airfoil–vortex interaction.* PhD thesis, VPI&SU, Blacksburg, VA, November 1996.
Available at http://scholar.lib.vt.edu/theses/public/etd-3125102110964235O/etd-title.html.

Contents

List of Tables

List of Figures

Nomenclature

c	= chord length, 0.203 m
c_l	= local lift coefficient
f	= frequency, Hz
G_{uu}, G_{vv}, G_{ww}	= u, v, w component velocity autospectra respectively
k	= turbulence kinetic energy (see Equation 3.1)
k_x, k_y	= axial and spanwise wave numbers respectively
l	= spanwise length scale (see Equation 3.10)
P	= turbulence kinetic energy production ignoring streamwise derivatives (see Equation 3.2)
R	= a sufficiently large, but finite number
r	= radial distance from vortex core center
r_1	= vortex core radius measured from the core center to the point of peak tangential velocity
Re_c	= Reynolds number based on chord length
Re_θ	= Reynolds number based on momentum thickness
Ro	= Rossby number defined as $U_d/V_{\theta 1}$
U, V, W	= mean velocities in the x, y, z directions respectively
U_d	= axial velocity deficit at vortex core center
U_∞	= free-stream velocity
u, v, w	= fluctuating velocities in the x, y, z directions respectively
V_x	= axial velocity in vortex aligned coordinate system
V_θ	= tangential velocity in vortex aligned coordinate system
V_{θ_1}	= peak tangential velocity of vortex
x, y, z	= coordinates defined in Figure 2.2
α	= angle of attack, positive for right hand rotation about the negative y axis shown in Figure 2.2
δ	= boundary layer thickness
$\delta^\star$	= displacement thickness

Γ = circulation

Γ_1 = vortex core circulation defined as $2\pi r_1 V_{\theta 1}$

θ = momentum thickness

Φ = traditional wave number frequency spectrum (see Equation 3.7)

ϕ = pointwise wave number frequency spectrum (see Equation 3.5)

τ_x = axial shear stress magnitude (see Equation 3.3)

Ω_x = mean axial vorticity

ω = frequency, Hz

Chapter 1

Introduction

An important component of helicopter rotor flows is the interaction of the blades with their own vortex wakes. These interactions are usually thought of in terms of their acoustic effects—the impulsive noise generated when the blade and vortex are nearly parallel and the broadband noise generated when they are nearly perpendicular. However, these interactions also have significant fluid dynamic effects on the subsequent development of the vortex and the flow surrounding it. When the same vortex suffers multiple interactions with the successive blades, these fluid dynamic effects can feed back significantly into both the acoustics and aerodynamics.

The purpose of this paper is to present measurements made in the wake of a perpendicular interaction between a streamwise vortex and the tip of a lifting blade. This work forms part of an broader study of the fluid dynamic effects of perpendicular blade–vortex interactions, see Devenport *et al.* [1], Wittmer *et al.* [2], Wittmer and Devenport [3, 4], and Wittmer [5]; for example. Wittmer and Devenport [3, 4] studied the interaction of a tip vortex with a blade of infinite span, approximating the case where the vortex passes well inboard of the tip. For small blade–vortex separations (less than about 0.25 blade chord lengths) they found the interaction to have a profound effect on the vortex structure. Specifically, the interaction causes negative streamwise vorticity to be shed into the blade wake which, combined with the positive vorticity of the vortex, produces an unstable velocity field. The new turbulence generated by this instability engulfs the vortex core bringing on a rapid growth and decay of its mean velocity field. The result is a much larger weaker vortex core surrounded by a comparatively intense and extensive turbulent region. Effects like these in a helicopter rotor can greatly influence the sound radiated by subsequent parallel or perpendicular interactions. Wittmer *et al.* [2] studied cases where the tip vortex passed the blade approximately one chord length from its tip. For close separations they too observed the interaction to produce a dramatic weakening of the vortex core coupled with an intensification and growth of the surrounding turbulent field. However they also observed some influence of the blade tip vortex; altering the form of the turbulent field and its intensity in the region outboard of the interaction

between the two vortex cores.

In the present study we take this progression one step further and examine the flow structure generated by an idealized perpendicular interaction occurring at the blade tip. While many of the details of such a flow are not obvious in advance, one would expect it to be dominated by the combined influence of both the initial vortex and that shed from the blade tip. The behavior of such co-rotating trailing vortex pairs has been studied in the past primarily because of its relevance to the roll up of transport aircraft wakes. Flow visualizations of the wakes of flapped and split wings (see: Bilanin *et al.* [6, 7], Brandt and Iversen [8], Smits and Kummer [9], Corsiglia *et al.* [10], and Ciffone [11]) have been used to reveal gross behavior of vortex pairs. Equal strength vortices orbit around each other and, depending on initial conditions, merge. For vortices of unequal strength, the weaker vortex becomes wrapped into an annulus around the stronger vortex core. Quantitative measurements in equal strength vortices shed by split wings have been made by Corsiglia *et al.* [12], Smits and Kummer [9], Zsoldos and Devenport [13, 14], and Vogel *et al.* [15, 16]. The data of Zsoldos and Devenport and Vogel *et al.* show that long before merger, the co-rotating vortex cores distort each other into ellipses and become turbulent. Their combined influence also leads to the generation of a new turbulence in an 'S' shaped region that bridges the vortex cores. This region ultimately forms the center of the merged vortex. Merger produces a large region of near axisymmetric turbulence surrounding the new core.

The remainder of this document is organized as follows. Chapter 2 includes a description of idealized configuration used to generate the vortex/blade-tip interaction and the instrumentation used to document the turbulence structure of its wake. The results and discussion, presented in Chapter 3, concentrate on turbulence measurements made in a cross section 15 chord lengths downstream of the blade trailing edge, and two-point spectral measurements here used to infer the length scales of the turbulence as a function of frequency. Chapter 4 summarizes the major findings of this study.

Chapter 2

Apparatus and instrumentation

2.1 Wind tunnel

Experiments were performed in the Virginia Tech Stability Wind Tunnel (Figure 2.1); a closed-circuit facility powered by a 600 horsepower axial fan. The test section has a square cross section 1.83 m×1.83 m and a length of 7.33 m. Flow in the empty test section is closely uniform with a turbulence intensity of less than 0.05% at 20 m/s. A slight favorable pressure gradient ($\partial C_p/\partial x = -0.003/\text{m}$) exists along the test section due to boundary layer growth which causes some convergence of the streamlines. Flow angles are small near the middle of the section but increase to about 2° near the walls Choi and Simpson [17]).

The free stream dynamic pressure and flow temperature are monitored continuously during operation of the wind tunnel. The former is measured using a pitot-static probe located at the upstream end of the test section connected to a Barocell electronic manometer. The latter is sensed using an Omega thermocouple located within the test section boundary layer—there is no significant temperature gradient across the boundary layer.

2.2 Blades

Untwisted NACA 0012 blades were used: one to generate the vortex and the other to interact with it. Both had a rectangular planform of 0.203 m chord (c) and both were set to a geometric angle of attack of 5° (clockwise rotation about the positive y axis shown in Figure 2.2). Effective boundary layer trips were placed on both blades. These consisted of 0.5 mm diameter glass beads glued in a random pattern along the entire span between the 20% and 40% chord locations. The resulting turbulent boundary layers were documented by Devenport *et al.* [18] (see Table 2.1).

The vortex generator blade (hereafter simply referred to as the generator) was mounted vertically as a half-wing at the center of the upper wall of the test section entrance with 0.879 m protruding into the flow (Figure 2.2).

The interaction blade was also cantilevered from the tunnel ceiling 14 c downstream of the vortex generator. However, the span and z-wise position of the interaction blade could be varied. Helium bubble flow visualization was used to determine these parameters. Being lighter than air, helium filled soap bubbles centrifuge into the vortex core, marking it clearly. The interaction blade was first positioned as close as possible to the situation where the generator vortex core stagnates on its tip as shown in Figure 2.3. Then it was moved $0.3c$ in the positive z direction so that the generator vortex passed to the suction side of its tip. This distance was selected because it provided a weak downstream interaction between the generator vortex and the interaction blade tip vortex—their mutual induction caused them to rotate about each other once over the 15 chord lengths between the interaction blade trailing edge and the measurement location.

2.3 Hot-wire anemometry

Miniature four-sensor hot-wire probes were used for single and simultaneous two point velocity measurements. Four-sensor probes consisting of two orthogonal X-wire arrays (Figure 2.4)—normally associated with vorticity measurements (Kovasznay [19])—are capable of simultaneous three-component velocity measurements from a relatively compact measurement volume and appear to overcome some of the gradient error problems associated with triple wire probes.

The probes were manufactured by Auspex Corporation (type AVOP-4-100). Eight stainless steel tapered prongs (75 mm in diameter at their tips) position the wires some 40 mm upstream of the main part of the probe (Figure 2.5). The sensors are etched tungsten wire of 5 mm diameter with an approximate length of 0.8 mm giving a length to diameter ratio of 160. The measurement volume of the probes are approximately 0.5 mm^3. The sensors are arranged as two orthogonal X-wire arrays with each wire inclined at a nominal 45° angle to the probe axis.

A block diagram of the measurement system is shown in Figure 2.6. Hot-wire sensors were operated separately using a Dantec 56C17/56C01 constant temperature anemometer unit. Anemometer bridges were optimized to give a frequency response greater than 25 kHz. The output voltages from the anemometer bridges were recorded by an IBM AT compatible computer using an Analogic 12 bit HSDAS-12 A/D converter which contains four separate converters. Hot-wire signals were buffered by four $\times 10$ buck-and-gain amplifiers with calibrated RC-filters to limit their frequency response to 50 kHz thereby providing high frequency noise attenuation. Voltage outputs from a digital thermometer and pressure transducer are also sampled by the A/D converter.

Probes were calibrated frequently for velocity using King's law to correlate the wire output voltages with the cooling velocities. Velocity components were determined from the cooling velocities by means of a direct angle calibration for each probe. To generate this calibration the probe was pitched and yawed over all likely flow angles in a TSI calibrator jet. Comparing the known pitch

and yaw angles with the probe outputs gives the true relationship between the cooling velocities and the flow angle. Hot-wire signals were corrected for ambient temperature drift using the method of Bearman [20]. A complete description of the hot-wire method used can be found in Wittmer [5].

One possible drawback of this calibration method is the implicit assumption that the angle calibration is independent of velocity. However, Wittmer [5] shows that for ±15% velocity variations—typical of small deficit flows such as the one studied here—the angle calibration changes by less than 0.5%.

2.4 Traversing mechanisms

Probe positioning inside the wind tunnel was aided by two computer controlled traverses. A two-axis (y and z) traverse, accurate to approximately 0.25 mm, was used to position a small one-axis sting mounted traverse (Figure 2.7). The sting mounted traverse contains two mounting blocks for the four-sensor hot-wire probes and could be rotated to allow traversing in along a single axis in the y-z plane. The mount closest to the sting was fixed relative to the sting, while the other mount could be traversed over a range of approximately one chord with an accuracy of about 0.1 mm. For single point measurements, a four-sensor probe was placed in the fixed mount and the moveable mount was empty. For the two point measurements, a four-sensor probe was placed in each mount and the probes were angled towards each other with an included angle of approximately 4° so that the probe tips (which were 0.13 m ahead of the mounting blocks) could be positioned as close as 2.5 mm.

	Pressure side	Suction side
$\delta/c \times 100$	4.41	5.92
$\delta^*/c \times 100$	0.98	1.54
$\theta/c \times 100$	0.57	0.82
Re_θ	1398	2023

Table 2.1: Boundary layer properties for the generator at 5° estimated from near-wake profile measurements at $x/c = 1.05$, $y/c = 1.2$. Data from Devenport *et al.* [18].

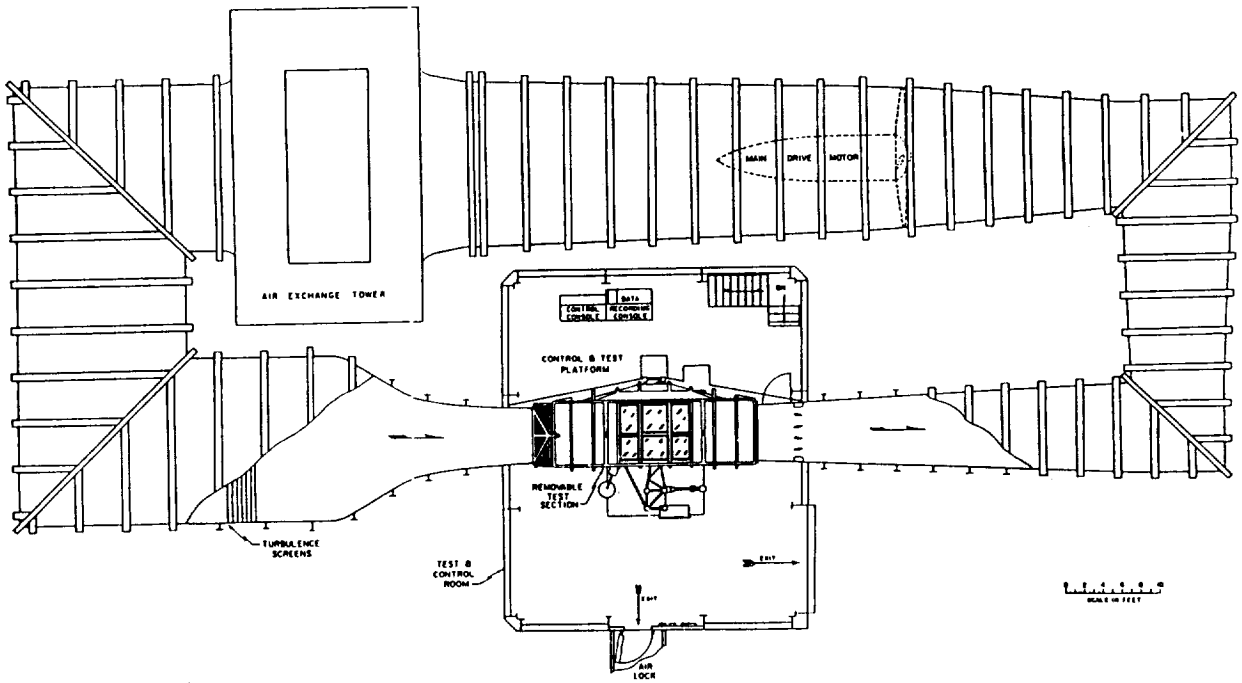

Figure 2.1: Virginia Tech Stability Tunnel

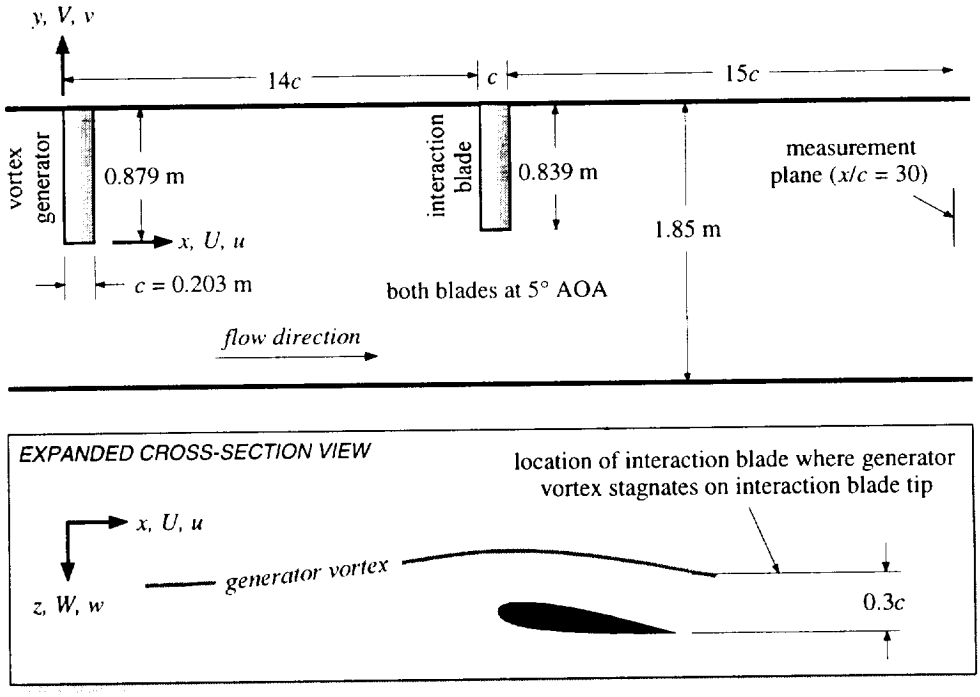

Figure 2.2: Wind tunnel schematic and coordinate system

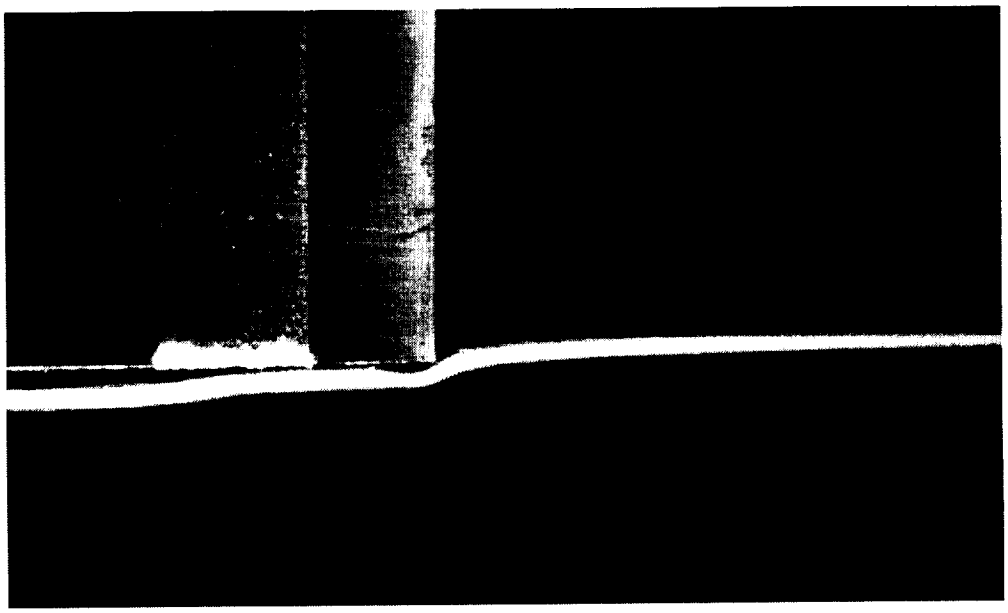

Figure 2.3: Close-up of helium bubble flow visualization showing vortex core nearly stagnating on interaction blade tip. Flow from right to left.

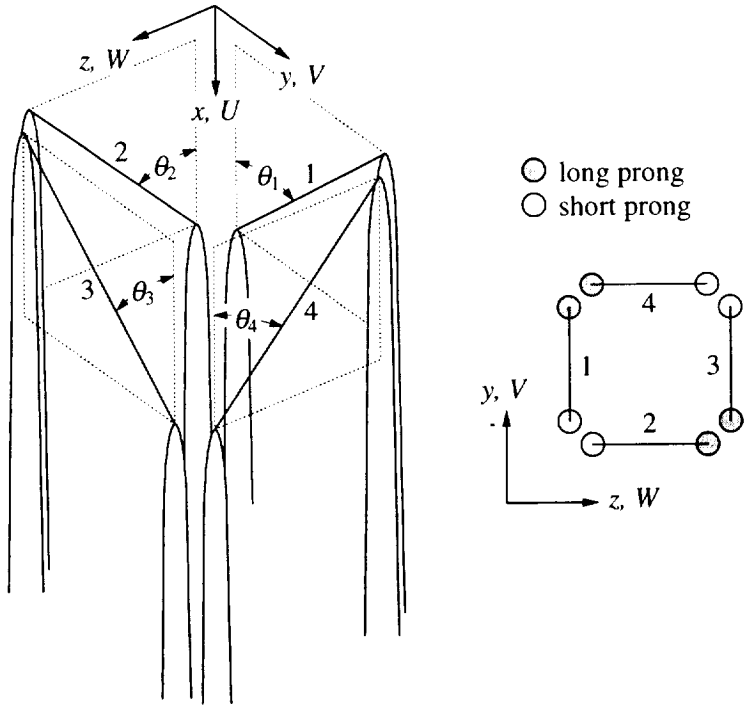

Figure 2.4: Four-sensor probe prong geometry

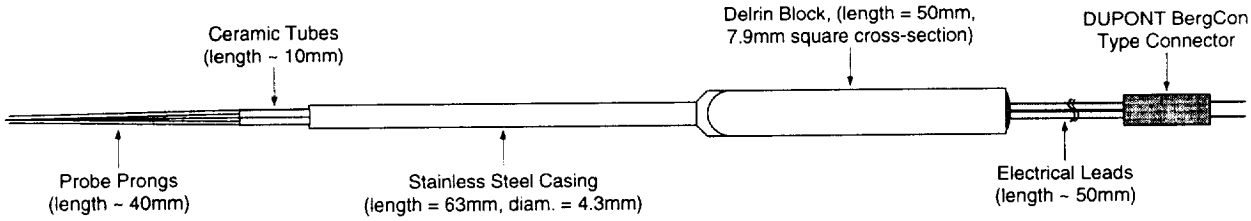

Figure 2.5: Auspex Corporation four-sensor probe (type AVOP-4-100) construction

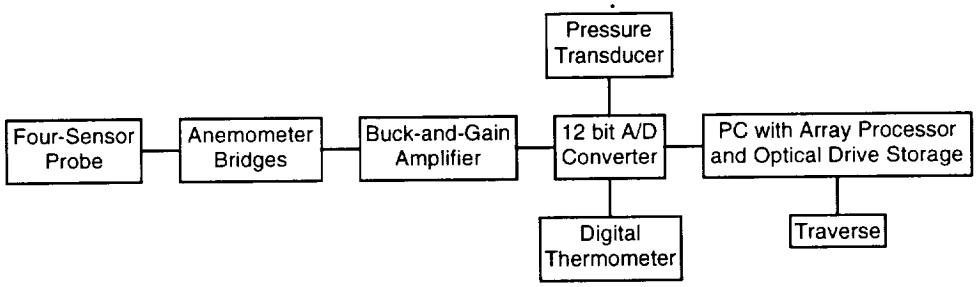

Figure 2.6: Measurement system block diagram

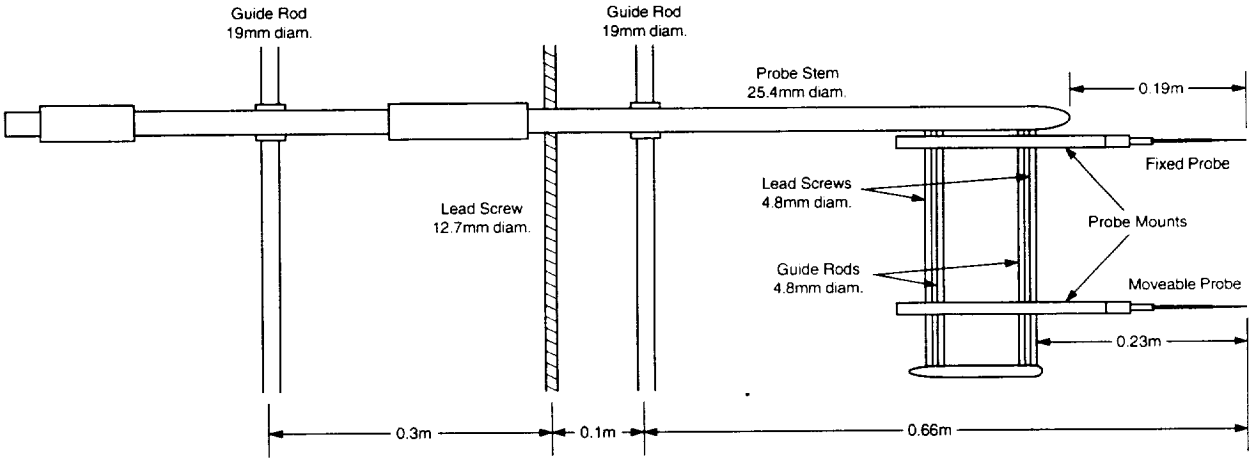

Figure 2.7: Sketch of traversing mechanisms

Chapter 3

Results and discussion

Measurements are presented in the wind-tunnel aligned coordinate system (x, y, z) shown in Figure 2.2. Coordinate x is measured downstream from the generator leading edge, y inboard from its tip, and z completes the right-handed system. The mean velocity components U, V, W; and fluctuating components u, v, w; are defined in the x, y, z directions respectively. In this system, the leading edge of the interaction blade is at $x/c = 14$. Measurements are presented in non-dimensional form normalized on the free-stream velocity (U_∞) indicated by the wind tunnel pitot-static probe, and blade chord (c).

All measurements were made in the y-z plane 15 chord lengths downstream of the interaction blade trailing edge ($x/c = 30$) at a chord Reynolds number of 260,000 ($U_\infty \approx 20\,\mathrm{m/s}$). Single point measurements were made throughout this plane to document the cross-sectional turbulence structure of the flowfield. These measurements also included detailed y direction profiles through the vortex cores. Uncertainty estimates for the single point velocity measurements are given in Table 3.1. To further investigate the turbulence structure in the vicinity of the vortices, measurements were made with two probes simultaneously. Two point measurements were made for a range of probe separations allowing the calculation of time and space correlations.

3.1 Single point measurements

3.1.1 Overall flowfield

Mean cross flow velocity vectors at the measurement locations are shown in Figure 3.1. The overall form of the mean and turbulent flowfield at $x/c = 30$ is represented by the contours of: mean streamwise vorticity (Ω_x), mean axial velocity (U), axial normal turbulence stress ($\overline{u^2}$), summed cross flow normal turbulence stresses ($\overline{v^2} + \overline{w^2}$), turbulence kinetic energy (k), turbulence kinetic energy production (P), and axial shear stress magnitude (τ_x) shown in Figures 3.2–3.8 respectively.

Definitions of k, P (ignoring streamwise derivatives), and τ_x are given in Equations 3.1–3.3.

$$k = \frac{1}{2}(\overline{u^2} + \overline{v^2} + \overline{w^2}) \tag{3.1}$$

$$P = -\overline{v^2}\frac{\partial V}{\partial y} - \overline{w^2}\frac{\partial W}{\partial z} - \overline{uv}\frac{\partial U}{\partial y} - \overline{uw}\frac{\partial U}{\partial z} - \overline{vw}\left(\frac{\partial W}{\partial y} + \frac{\partial V}{\partial z}\right) \tag{3.2}$$

$$\tau_x = \sqrt{\overline{uv}^2 + \overline{uw}^2} \tag{3.3}$$

The core edges of the generator and interaction blade tip vortices have been added to several of the figures with the assumption that they are circular. The radii are determined in Section 3.1.2.

As anticipated, these figures show the flow to be dominated by the two tip vortices and their interaction. At this location the generator tip vortex, centered at $y/c = 0.419, z/c = -0.013$, lies above the center of the blade tip vortex at $y/c = 0.369, z/c = 0.206$ (see Figure 3.3)—the two have rotated once about each other over the 15 chord lengths downstream of the blade. The distance between the two, some $0.225c$, is only slightly less than the nominal generator vortex/blade-tip separation of $0.3c$. This suggests that the vortices are only slowly approaching each other, if at all. The contours show the cores to be embedded in a turbulent region formed by the roll up of the two spiral wakes. Interestingly, away from the vortex cores the blade and generator wakes appear to have merged, producing a single spiral. Closer to the cores the two wakes can only be distinguished by the region of low turbulence levels to their right, near $y/c = 0.65, z/c = 0.17$ (see Figure 3.6 for example). This is apparently free-stream fluid trapped between the generator wake (wrapping around the outside of this region) and the blade wake (pássing between it and the cores). Based upon measurements in the undisturbed vortex at the blade location (Devenport *et al.* [22]), we know that for a blade vortex separation of $0.3c$ the bulk of the generator wake must pass to the pressure side of the blade. As a result a region of free-stream becomes trapped between the two vortices as they evolve, giving rise to the structure seen in the present measurements.

The contours of axial normal stress and turbulence kinetic energy (Figures 3.4 and 3.6) show particularly elevated turbulence levels along a ridge that joins the two vortex cores. While wandering is undoubtedly an important contributor to the turbulence stresses in the core, its influence between the cores should be fairly small since the local mean velocity gradients are comparatively weak here. This feature, which is therefore real, bears a striking resemblance to the region of elevated turbulence levels found to link the cores of co-rotating vortices undergoing merger seen by Vogel *et al.* [16]. They hypothesized that this region is formed by the same mechanism that produces the braid seen between adjacent spanwise eddies in a two-dimensional mixing layer (*e.g.* Lasheras *et al.* [21]). Specifically, the combined mean velocity fields of the two vortices produce high mean strain rates that tend to organize and intensify turbulent structures with axes roughly parallel to a line joining the vortex centers. Vogel *et al.*'s speculation is confirmed to some extent

by an analysis of the same data set by Zsoldos [14] which shows broad but distinct peaks in velocity spectra measured midway between the cores—consistent with presence of quasi-periodic large scale eddies with this orientation. The peak frequency in Zsoldos' data suggests a preferred streamwise spacing roughly equal to the distance between the vortex centers. Autospectra of v component velocity fluctuations at point B midway between the present vortex cores (Figure 3.9) show a peak similar to that in Zsoldos' data, at a non-dimensional frequency $fc/U_\infty = 3$. Assuming Taylor's hypothesis this implies a streamwise spacing of any organized turbulent eddies of 0.33 chord lengths, approximately the sum of the distance between the vortex centers and their radii. Note that the spectral peak seen in Figure 3.9 is almost absent from the corresponding w velocity component spectrum. This anisotropy is also consistent with organized eddies with axes roughly parallel to a line joining the vortex cores.

3.1.2 Core structure

The contours of mean-flow and turbulence quantities are of limited value in the interpretation of the flow structure in the vortex cores themselves because of the effects of wandering. Wandering motions expose a fixed probe to a range of positions with in the vortex, smoothing the measured mean-velocity field and producing apparent velocity fluctuations that swamp the true turbulence stresses. Devenport *et al.* [22] provide a method for estimating the amplitude of wandering motions and for correcting the effects that smoothing has on the measured core parameters. To apply this method, the proportion of the measured stress level at the core center due to wandering must be known. If it is assumed that 100% of the stress is the result of wandering motions, an upper limit to the effects is established. However in the present work it was possible to obtain a more accurate estimate. Specifically, the simultaneous two-point measurements discussed in Section 3.2.2 below show that the bulk of velocity fluctuations produced by wandering are at non-dimensional frequencies $fc/U_\infty < 1.4$. Therefore, the proportion of measured stresses due to wandering can be determined by filtering the velocity signals before computing the stresses.

Figures 3.10– 3.13 show the turbulent stress profiles on the lines S1 and S2 (illustrated in Figure 3.6) that pass through the generator and blade tip vortex cores. Unfiltered data and data high-pass filtered at $fc/U_\infty = 1.4$ are presented.[1] These data show that roughly 75% of the stresses at the generator vortex core center, and 50% for the interaction blade vortex, were produced by wandering. Using the formulae of Devenport *et al.* [22] we therefore estimate the r.m.s. wandering amplitudes (σ) of the generator and interaction blade tip vortex cores to be 0.7%c and 0.8%c, respectively.

Mean velocity profiles measured through the two cores on lines S1 and S2 are shown in Figures 3.14 and 3.15. The estimated tangential velocity ($V_\theta(r)$) fields derived from rotating the profile

[1]The filtering could be performed by re-processing the data since full velocity time-histories were recorded during the measurement.

data into a core aligned coordinate system are shown in Figure 3.16. These profiles should be interpreted in the light of the wandering motions discussed above in Section 3.1.1, which would have smoothed them. Using the formulae of Devenport *et al.* [22] we estimate that wandering would have introduced errors no greater than $0.5\%U_\infty$ and $0.7\%U_\infty$ in the tangential and axial velocity profiles respectively for the generator tip vortex core, and $0.2\%U_\infty$ and $0.3\%U_\infty$ for the blade tip vortex core. Using the same formulae to correct core parameters inferred from these profiles we obtain the following values for the generator tip vortex core: core radius, $r_1 = 0.049c$; peak tangential velocity, $V_{\theta_1} = 0.215U_\infty$; and centerline axial velocity deficit, $U_d = 0.147U_\infty$. A summary of the core parameters is given in Table 3.2. These data imply a core circulation ($\Gamma_1 = 2\pi r_1 V_{\theta_1}$) of $0.066U_\infty c$ and a Rossby number ($Ro = U_d/V_{\theta_1}$) of 0.68. According to the analysis of Mayer and Powell [23] a Rossby number of less than 1 should produce an stable vortex core. It is interesting to compare these measurements with those made by Devenport *et al.* [22] in the same tip vortex, at the same location, but with no interaction blade. After correction they report values of $V_{\theta_1} = 0.295U_\infty$ and $r_1 = 0.044c$. The difference suggests that the interaction with the blade tip and the vortex it sheds stimulates some decay and growth of the tip vortex core.

After correction for wandering effects the interaction blade tip vortex core parameters are: $r_1 = 0.074c$, $V_{\theta_1} = 0.132U_\infty$, and $U_d = 0.103U_\infty$. Even though the interaction blade vortex core radius is 1.5 times the size of the generator vortex core, the core circulation ($0.061U_\infty c$) is almost the same because of the lower tangential velocity (see Table 3.2). The difference in core size may be a result of the non-uniform inflow induced on the interaction blade by the passing vortex. Using the velocity distribution of the generator vortex at $x/c = 10$ measured by Devenport *et al.* [22], and assuming the non-uniform inflow has the same effect as blade twist, lifting line theory can be used to estimate the interaction blade span loading as shown in Figure 3.17. The effect of the vortex is to diminish the angle of attack of the blade inboard of its tip, reducing its loading, and thereby reducing the amount of shed vorticity near the tip. This provides a simple explanation for the weak vortex core. Since the undisturbed vortex shed from a wing with the same loading was not measured, the downstream effects due to the interaction with the generator vortex cannot be isolated.

The contours and profiles of the turbulence stresses reveal little of the turbulence structure of the core. Even with wandering filtered out, the stress profiles through the core do not reflect 'true' turbulence levels because, as discussed by Devenport *et al.* [22], intense velocity fluctuations in the core may also be produced by inactive motions generated as the core is buffeted by the turbulence that surrounds it. One of the best methods of examining the true turbulence structure is to plot velocity autospectra measured on a radial profile to the core center. Figures 3.18 and 3.19 show velocity autospectra at selected points along profile S1 leading to the generator vortex core at $y/c = 0.419, z/c = -0.013$; and Figures 3.20 and 3.21 show points along profile S2 leading towards

the interaction blade vortex core at $y/c = 0.369, z/c = 0.206$. Both sets of spectra show the same behavior. Far from the core, in the surrounding turbulent region, the spectra display a turbulent wake-like form (see for example Wygnanski *et al* [24]). Moving toward the core center, spectral levels at all frequencies rise. The rise in spectral levels at low frequencies ($fc/U_\infty < 20$) is likely due to wandering and inactive motions of the vortices (see Section 3.2.2). At high frequencies ($fc/U_\infty > 20$) where the small scale turbulence structures should account for most of the velocity fluctuations, spectral levels in the core are much higher than points outside the core. This is in contrast to the findings of Devenport *et al.* [22] in their study of the isolated generator vortex where high frequency spectral levels in the vortex core fell to levels significantly lower than those in the surrounding wake. Devenport *et al.* took this as evidence of a laminar vortex core. The contrary behavior in the present vortices suggest these cores are turbulent, and a significant portion of the velocity fluctuations measured in the core region are the result of turbulence.

A similar increase in core turbulence levels also occurred downstream of the interaction between a vortex and an infinite span blade studied by Wittmer and Devenport [4] and Wittmer [5]. For the infinite span interaction blade configuration, high frequency turbulent fluctuations in the vortex core increased for blade–vortex separations less than about 0.25 chord lengths, although the change was seen to occur several chord lengths downstream of the interaction. Vogel *et al.* [15, 16] also measured increased levels of high frequency fluctuations compared to an isolated vortex in their study of co-rotating vortex pairs of equal strength.

3.1.3 Modeling

Although the vorticity field surrounding the vortices is very complex (see Figure 3.3), a simple inviscid model will be used to describe their motion. Considering two line vortices of equal strength Γ separated by a distance of $0.225c$,[2] the following relation states that the time it takes for the vortices to travel $15c$ downstream is equal to the time required for the vortices to rotate about each other once under their mutual influence.

$$\frac{15c}{U_\infty} = \frac{\pi(0.225c)}{\frac{\Gamma}{2\pi(0.225c)}} \tag{3.4}$$

Solving this equation for the strengths of the line vortices results in $\Gamma = 0.067 U_\infty c$. Interestingly, this value is nearly the same as the estimated core circulations of the generator and interaction blade tip vortices: $\Gamma_1 = 0.066 U_\infty c$ and $\Gamma_2 = 0.061 U_\infty c$ respectively. Therefore it appears that the motion of each vortex cores can be approximated by a line vortex with strength equal to the vortex core circulation.

[2]Note that in Section 3.1.2 it was found that the vortex cores are separated by $0.225c$ with nearly equal circulations.

3.2 Two-point measurements

Simultaneous measurements were made using two four-sensor hot-wire probes to judge the scales of the turbulence associated with the interacting vortices and to provide insight into the turbulence structure from the perspective of broadband noise prediction. Data was taken on a series of horizontal (y-wise) lines through the flow, shown on Figure 3.4, so as to reveal the flow as it would be seen by following blade cutting through the vortex pair. Measurements on each line were made with one of the probes fixed at the location marked with the filled circle. The other probe was then traversed relative to it to a number of points along the line. At each probe separation, one hundred, 3072 point records were recorded for each of the 8 simultaneous sensor signals at a sampling frequency of 50 kHz over a total measurement time of approximately one minute.

By angling the probes towards each other by about 2° each, it was possible to make measurements with the center points of the measurement volumes separated by only 2.5 mm ($0.0125c$).[3] Ideally, a very small minimum separation is desirable when making two point measurements. It enables one to fully define the cross-spectrum as a function of separation even at high frequencies. However, closer approach of the present probes was considered too risky; and given the 0.8 mm diameter of their measurement volumes, unlikely to produce meaningful results. Furthermore, the minimum probe separation was not found to be a limiting factor in determining wave-number frequency spectra as demonstrated below. Measurements were made to a maximum probe separation of $0.75c$ on both sides of the fixed probe at a total of 94 separations.

Extensive probe interference studies using the two probe support were performed by Miranda and Devenport [25]. The support and probes were placed at various locations around and within the tip vortex shed from a single rectangular wing at 5° angle of attack and chord Reynolds number of 320,000. Helium filled soap bubbles were used to visualize the center of the vortex core, which appeared completely undisturbed by the probes and their support at the measurement point. Miranda and Devenport also made velocity measurements to this end. They did find a small interference effect which produced at most a 0.7% change in the measured mean velocity for the smallest probe separation. Interestingly, the approximate magnitude of this effect was predicted by Devenport *et al.* [22] using a potential flow model of a single probe.

3.2.1 Coherence and phase

The two-point measurements were processed first by computing the cross-spectra of the velocity components. Figures 3.22–3.22 show selected results for horizontal line T1 that passes between the cores. Coherence and phase between velocity fluctuations of the same component at the fixed probe

[3]The instantaneous velocity vectors measured by the probes were, of course, rotated back during processing to account for this misalignment.

location A (midway between the core centers) and a representative set of traversing-probe locations 1 though 6 (see Figure 3.4) are shown. Note that spectra are shown for all velocity components. In the context of broadband noise production by a hypothetical blade cutting this turbulent flow at the location of the line T1, the upwash component is w (shown in Figure 3.24).

These results clearly show no coherence at any frequency or in any component between velocity fluctuations at A and 1, and at A and 6. This suggests that the turbulent velocity fluctuations between the cores are largely uncorrelated with the turbulence in outer parts of the surrounding spiral wake, ruling out the (rather remote) possibility that the coherent turbulent eddies in this flow are long, convoluted structures that instantaneously connect the core regions to the surrounding wakes. Significant correlation is, however, seen at closer spacings. Moving closer to point A from the right, the coherence remains zero until point 2 is reached. Here, an in-phase peak begins to appear in v (Figure 3.23) centered at a frequency fc/U_∞ of about 3. The separation of points A and 2 suggests this peak must be produced by structures with a spanwise scale of some $0.23c$. Assuming Taylor's hypothesis, the peak frequency suggests a streamwise scale of about $0.33c$. These implied scales and aspect ratio suggest that the largest turbulent eddies are comparable in size to the region of most intense turbulence kinetic energy that surrounds the cores. Moving toward point A from the left, the coherence remains zero until point 5 where a similar in-phase peak appears in v. For locations closer to the fixed probe (3 and 4), the coherence around $fc/U_\infty = 3$ increases dramatically in all components, reaching maxima in excess of 0.8 in v. The preference for organized v velocity fluctuations could be taken as indicative of roughly vertically aligned turbulent eddies, such as might be generated by stretching between the vortex cores (see discussion in Section 3.1.1).

Quite a different picture emerges with the fixed probe in the center of the interaction blade tip vortex core (location B, traverse T2). Figures 3.25–3.27 show representative coherence and phase spectra between the core center velocity fluctuations recorded at B and fluctuations at locations 7 through 12. Moving in from the right (locations 7, 8, and 9) or the left (12, 11, 10) significant coherence is first seen at the very lowest frequencies ($fc/U_\infty < 0.5$); so low in fact that they are not fully resolved by the present analysis. This is almost certainly the result of vortex wandering and demonstrates conclusively (and for the first time) that the phenomenon of wandering is not just coherent over the core, but over a substantial cross section of the surrounding flow—as assumed by the analysis of Devenport *et al.* [22]. The lack of coherence at frequencies $fc/U_\infty > 1$ between the core center and points 7, 8, 11, and 12; and, for that matter, any other points outside the core suggests that turbulent structures spanning the boundary of the vortex core must be weak if present at all. With the both probes inside the core edge (locations 9 and 10) the coherence associated with wandering becomes very large, particularly in the v and w components (Figures 3.26 and 3.27). The region where significant coherence is seen also broadens encompassing higher frequencies up to about $fc/U_\infty = 10$, and there are some signs of peaks around $fc/U_\infty = 3$ and $fc/U_\infty = 7$; perhaps

indicating some indirect connection between the turbulent eddies that span the region between the cores and velocity fluctuations at the core center.

In terms of these coherence and phase measurements the structure of the generator tip vortex core and its relationship to its surroundings appears very similar to that for the blade-tip vortex core. Figures 3.28–3.30 show coherence and phase measurements between core-center velocity fluctuations at point E and selected points along line T5. At separations large enough for the traversing probe to be outside the core (locations 25, 26, 29, and 30) there is no significant coherence except that associated with wandering. At separations small enough to put the traversing probe inside the core, the coherence associated with wandering is large but there is also some coherence at higher frequencies suggesting that other mechanisms may be producing velocity fluctuations here.

Figures 3.31–3.36 show coherence and phase calculations for lines T3 and T4 that cut through the bottom and top of the turbulent region that surrounds the vortices. Results for these two lines are essentially the same. At smaller separations they both show significant coherence at the lowest frequencies associated with wandering (particularly in the v component, Figures 3.32 and 3.35) and coherence apparently associated with organized turbulent motions at higher frequencies. The w component spectra (Figures 3.33 and 3.36) show a distinct peak at around $fc/U_\infty = 3$—the same preferred frequency seen on profile T1 passing between the cores. The preference for w component velocity fluctuations suggests that this peak may be produced by eddies aligned roughly horizontally, consistent with the orientation of the spiral wake where it is cut by T3 and T4.

3.2.2 Wave-number frequency spectra

Coherence and phase spectra are a revealing but inefficient way of presenting the near continuous two-point measurements that were made. A much more compact representation of the turbulence length scales and their variation with frequency can be obtained by taking the double Fourier transform of the data. Specifically, we define a 'pointwise' wave-number frequency spectrum about the fixed probe location y as

$$\phi_{ww}(y, k_y, \omega) = \frac{1}{2\pi} \int_{-\infty}^{\infty} G_{ww}(y, y', \omega) \mathrm{e}^{-jk_y y'} \, dy' \tag{3.5}$$

where y' denotes the probe separation, ω the angular frequency, and $G_{ww}(y, y', \omega)$ the cross-spectrum between w component velocity signals at y and $y + y'$ defined as,

$$G_{ww}(y, y', \omega) = \lim_{T \to \infty} \frac{\pi}{T} E[w(y, \omega) w(y + y', \omega)] \tag{3.6}$$

Similar expressions may of course be written for v and u.

It is important to realize that this pointwise spectrum differs from the traditional wave-number frequency spectrum used to characterize homogenous turbulent flows in, for example, broadband noise prediction schemes (*e.g.* Amiet [26]). This traditional spectrum is defined as the double Fourier transform of the space-time velocity autocorrelation function, *i.e.*

$$\Phi_{ww}(\omega, k_y) = \frac{1}{4\pi^2} \int_{-\infty}^{\infty} \int_{-\infty}^{\infty} \lim_{T\to\infty} \frac{1}{RT} \int_{-T/2}^{T/2} \int_{-R/2}^{R/2} w(y,t)w(y+y',t+\tau)\, dydt\, e^{-j\omega\tau} e^{-jk_y y'}\, d\tau dy' \tag{3.7}$$

This equation may be re-written in terms of the two-point cross-spectrum $G_{ww}(y, y', \omega)$ as

$$\Phi_{ww}(\omega, k_y) = \frac{1}{2\pi R} \int_{-\infty}^{\infty} \int_{-R/2}^{R/2} G_{ww}(y, y', \omega)\, dy\, e^{-jk_y y'}\, dy' \tag{3.8}$$

and thus we see that

$$\Phi_{ww}(\omega, k_y) = \frac{1}{R} \int_{-R/2}^{R/2} \phi_{ww}(y, k_y, \omega)\, dy \tag{3.9}$$

That is, the traditional wave-number frequency spectrum is the spanwise average of the 'pointwise' spectrum used here. In homogenous turbulence this averaging would have no effect since ϕ_{ww} would be independent of y. In the strongly inhomogenous turbulent flow produced by the tip vortices, however, ϕ_{ww} is likely to be a strong function of the fixed-probe location y and the averaging that has not been performed should be borne in mind when interpreting results.

In principle it would be possible to fully measure Φ_{ww} by placing the fixed probe at a complete range of y locations and measuring ϕ_{ww} for each. However, such a measurement would be prohibitively time-consuming and, it could be argued, of questionable value in understanding the turbulence structure since much information about inhomogeneity and coherent eddies would be averaged out.

The Fourier transform in Equation 3.5 was performed by FFT. To apply the FFT algorithm it was necessary to interpolate the data to equal intervals in y' and zero-pad it to give a number of intervals equal to an integer power of 2—in this case 128. The smallest spanwise measured spanwise separation was $0.0125c$. Since all other separations were integer multiples of this value the data was linearly interpolated to y' intervals of this size.

At all separations except the smallest, the resolution and range in y' before interpolation was easily sufficient to capture the shape of G_{ww} and its complete decay to zero at larger separations. However, the smallest separation of $0.0125c$ was too large to resolve the variation in $G_{ww}(y, y', \omega)$

at small y' for higher frequencies: this function becomes more and more like a delta function in y' with increase in frequency. To examine the effects of this under-resolution on the estimates of ϕ_{ww}, spectra were re-computed with an increased resolution using an interpolation scheme for small y' based on the Liepmann model of isotropic turbulence (see Amiet [26]). Sample results, presented in Figure 3.37 show the resolution at small y' to have no discernible effect on the final wave-number frequency spectrum. This result was both surprising and welcome since we expected the minimum probe separation to pose a much more serious limit on the measured wave-number frequency spectra.

Figures 3.38–3.52 show the resulting wave-number frequency spectra for each velocity component calculated for all the lines T1 through T5 in terms of both their real and imaginary parts. The spectra are plotted *vs.* normalized spanwise wave-number $k_y c$ and frequency expressed as the nominal streamwise wave-number $k_x = \omega c/U_\infty$. In all plots, spectral levels have been normalized on the mean square fluctuation of the relevant velocity component at the fixed probe location. This ensures that all the real spectra integrate to unity. All the imaginary spectra integrate to zero by definition: both globally and at any given frequency. Note that imaginary parts would not appear if the spectra were averaged with respect to y' since the Fourier Transform of an autocorrelation function must be real.

Figures 3.53–3.55 summarize and directly compare these spectra in terms of spanwise length scale l as a function of frequency. By analogy with Amiet [26] we define l as

$$l(\omega) = \frac{1}{2G_{ww}(y,0,\omega)} \int_{-\infty}^{\infty} G_{ww}(y,y',\omega)\, dy' = \pi \frac{\phi_{ww}(y,0,\omega)}{G_{ww}(y,0,w)} \tag{3.10}$$

with similar expressions for the u and v components.[4] Note that unlike Amiet, we carry the integration from $-\infty$ to ∞ since $G_{ww}(y,y',\omega)$ is not symmetric with y' in the inhomogenous turbulence produced by the vortices. This leads to the extra factor of 2 multiplying the first instance of $G_{ww}(y,0,\omega)$. As indicated, the length scale can be determined either from the wave-number frequency spectrum or by integration of the cross-spectrum as a function of separation y'. Both methods applied to the present data produced identical results. Note that the length scale must be real but can, in principle, be negative.

For comparison with these data we plot a von Karman wave-number frequency spectrum for isotropic homogenous turbulence (Figure 3.56) and the length scale distribution inferred from that (included in Figures 3.53–3.55). The von Karman spectrum is a useful here because it shows how homogeneity and isotropy appear in the wave-number domain (*i.e.* as concentric circles). It is also interesting to compare this spectrum with real data from an anisotropic inhomogenous turbulent

[4]Strictly speaking, Amiet only intended use of this concept with the upwash velocity component. We extend it here to all velocity components since it is a convenient tool for summarizing and comparing the data.

flow since it is often used to represent such flows in broadband noise computations.

We also compare the results with measurements of the spanwise wave-number frequency spectrum (Figures 3.58–3.60) and length scale distribution (Figures 3.53–3.55) of a near-two-dimensional turbulent wake. These measurements were made by Miranda and Devenport [25] and processed in a manner identical to those discussed here. Miranda and Devenport's flow, illustrated in Figure 3.57, was the wake of a rectangular NACA 0012 lifting blade at 5° angle of attack and chord Reynolds number of 320,000.[5] Measurements were made in a cross-sectional plane 10 chord lengths downstream of the wing leading edge. The data presented here are computed from a series of two-point measurements made in the two-dimensional region well inboard of the tip vortex along a spanwise line coincident with the wake centerline and show how anisotropy and organized turbulence structure appear in the spectrum. A two-dimensional turbulent wake is dominated by a quasi-periodic train of spanwise eddies. These produce a strong peak in the w spectrum (the cross-flow component perpendicular on average to the axes of the eddies, Figure 3.60) centered at the eddy-passing frequency—a feature completely absent in the von Karman spectrum. The anisotropy of these eddies and the turbulence in which they are embedded results in quite different spectra in different velocity components (compare Figures 3.58– 3.60) and different length scales in different directions. The squashed appearance of the spectra when compared with the von Karman spectrum results from the fact that the spanwise correlation length scale in a two-dimensional turbulent wake is significantly smaller than that in the streamwise direction.

A significant issue that surfaces when trying to make these kind of comparisons is how the wave-number axes should be normalized. In homogenous turbulence comparisons between wave-number frequency spectra are made by normalizing on the integral length scale—indeed it is necessary to choose such a length scale before the von Karman spectrum can be plotted. This makes sense when the flow is isotropic and there is only one scale. In the present flow, however, the anisotropy and inhomogeneity produce many different candidate scales making the choice of a single length scale somewhat arbitrary. Rather than make this choice we have plotted the von Karman spectra in Figures 3.53–3.56 by retrospectively choosing a length scale that put it as close as possible to the middle of the present measurements. Since the two-dimensional wake data were measured at a similar streamwise location downstream of an identical blade, we have elected to leave these normalized on blade chord.

With the von Karman and two-dimensional wake spectra in mind we now turn to our discussion of the present measurements, beginning with the wave-number frequency spectra for the line T1 that passes midway between the vortices, specifically its v and w components (Figures 3.39 and 3.40). The real parts of these spectra have basically the same form: a region of high spectral levels at small k_x and k_y and a decay at larger wave-numbers. The rate of decay on the k_x axis is roughly

[5]This is the same tripped wing used here as the interaction blade.

consistent with a -1 slope in the spanwise length scale with frequency, when plotted on a log-log scale (see Figures 3.54 and 3.55). The region of high spectral levels in the v spectrum is dominated by a single peak centered at $k_x c = 20$ and $k_y c = 0$ that bears a close resemblance to that seen in the w spectrum of the two-dimensional wake (Figure 3.60). This is the same peak centered at $fc/U_\infty = 3$ seen in the coherence spectra for points 2, 3, 4, and 5 (figure 3) —there being a factor of 2π between these two representations of frequency. The implication is that this peak is produced by quasi-periodic, turbulent eddies structures in the region of stretched turbulence between the cores. The fact that the peak has left-to-right symmetry indicates that, on average, the velocity fluctuations produced by these structures are experienced simultaneously at points along T1 and thus the structures are not skewed with respect to this axis. The fact that the imaginary part of this spectrum is comparatively small is a sign that the velocity signatures produced by these structures are fairly symmetric about point A. The region of high real spectral levels in the w spectrum (Figure 3.40) is dominated by a similar 'coherent structure' peak at the same frequencies and wave-numbers. However, this spectrum also has two peaks at near-zero frequency at $k_y c = \pm 30$. These low frequency motions of finite spanwise length scale are the vortex wandering. The wave-number $k_y c = \pm 30$ implies a spanwise scale of some $0.2c$ consistent with the inference that the wandering motions are coherent over a region that extends well beyond the core edge.

The u component spectrum for T1 (Figure 3.38) is quite different from the other two components and is less easily explained by comparison with the two-dimensional wake. Its imaginary part has two intense lobes arranged antisymmetrically about the k_x axis and roughly centered on the line $k_x c = 20$—the location of the 'coherent-structure' peak in the v component spectrum (Figure 3.39). The real part contains a negative region on the k_x axis in the vicinity of $k_x c = 20$ and most of its positive energy well away from the k_x axis at large spanwise wave-numbers. As a result the spanwise length scales estimated from this spectrum (Figure 3.53) are either negative or very small compared to those of v and w (Figures 3.54 and 3.55) over the entire resolvable frequency range. This behavior in the u spectrum may indicate the following: The coherent structures responsible for the strong peaks in v and w produce correlated velocity fluctuations in u only over comparatively a short spanwise distance surrounding point A, thus the shift of energy to higher spanwise wave-numbers. These fluctuations correlate asymmetrically about A, thus the strong antisymmetric imaginary component. For a substantial range of separations and frequencies, in the fluctuations are in antiphase with fluctuations at A, thus the negative and near-zero real spectral levels on the k_x axis.

Consider next the spectra for lines T2 and T5 taken about points B and E at the centers of the interaction blade and generator vortex cores respectively (Figures 3.41–3.43 and 3.50–3.52). Both sets of spectra show similar features, indicating some similarity in the instantaneous flow structure associated with the cores. The v (Figures 3.42 and 3.51) and w (Figures 3.43 and 3.52) component

spectra appear stretched in the k_y direction compared with those measured between the cores. This is because the spanwise length scales in the cores are much smaller (see Figures 3.39 and 3.40) and the apparent streamwise length scales are somewhat greater. All these spectra show intense peaks or bands at near-zero frequency produced by vortex wandering motions. The influence of wandering is particularly strong in the v component consistent with the orientations of the measurement lines T2 and T5 relative to the primarily tangential velocity fields of the vortex cores. Wandering is not the only feature, however. The v component spectra for both cores show a distinct ridge centered on the line $k_x c = 20$. Peaks are visible at the same frequency in the u spectra (Figures 3.41 and 3.50) at centered near spanwise wave-numbers of $k_y c = \pm 80$. The appearance of features near $k_x c = 20$ implies some connection with the turbulent structures seen in the spectrum measured on line T1. Possibly the cores are being buffeted by the turbulent structures between them, or perhaps the structures are producing waves on the cores of the vortices. This second possibility appears consistent with the form of the u spectra. The two peaks in the real part of the spectra at around $k_y c = \pm 80$ and the lower values found between them near the k_x axis are consistent with a core motion that produces in-phase velocity fluctuations near its center coupled with out of phase fluctuations around its edge ($k_y c = 80$ corresponds to a length scale comparable to the core radii). Motions of this type would be expected in the presence of axisymmetric core waves.

An unexpected characteristic of the wave-number frequency spectra measured on lines T1, T2 and T5 is how they tend to distinguish the velocity fluctuations produced by wandering from other motions; a distinction not seen in a single-point spectrum. Specifically they show that wandering is the dominant contributor to velocity fluctuations at frequencies less than about $k_x c = 9$ ($fc/U_\infty = 1.4$), but is a relatively minor player at higher frequencies. The percentage of measured turbulence stress caused by wandering can therefore be estimated by filtering the data at this frequency. We find, for example, that at point A between the vortex cores, wandering constitutes 12% of the turbulence stress $\overline{w^2}$ but that wandering has a much larger contribution in the blade tip and generator vortex cores (points B and E) where it accounts for at least 66% of $\overline{w^2}$. A more detailed discussion of filtering is given in the discussion of the single-point data (Section 3.1.2).

Finally consider the spectra for lines T3 and T4 that cut through the bottom and top of the turbulent region containing the cores (Figures 3.44–3.49). These two sets of spectra are remarkably alike each other and the two-dimensional wake spectra, indicating a close similarity in instantaneous turbulence structure. On the one hand this similarity might be expected since both T3 and T4 may be thought of as cutting horizontal sections of the spiral wake surrounding the vortices. On the other hand, the spiral wake at T3 and T4 is highly curved and strained by the vortices and its turbulence structure is likely to have been heavily disrupted by the proximity of the cores. This similarity may therefore indicate some insensitivity of the wave-number frequency spectrum to local conditions—a result that may be useful in future modeling efforts. For T3 and T4 both upwash

(w component) spectra show a strong peak near $k_x c = 20$, $k_y c = 0$ and a similar rate of decay at higher (and lower) wave-numbers (Figures 3.46 and 3.49). These peaks would be consistent with the presence of quasi-periodic horizontally aligned turbulent eddies. Interestingly they bear some further resemblance to the v component spectrum seen between the cores on line T1 (Figure 3.39). Likewise the v component spectra for T3 (Figure 3.45) and T4 (3.48) are fairly similar to the w spectrum on line T1 (Figure 3.40). None of the spectra for T3 and T4 are exactly symmetric about the k_x axis: those for T4 being slightly biased to the right (positive k_y) and those for T3 to the left. This asymmetry is an indication that the turbulence structures responsible for these parts of the spectra are skewed and arrive earlier on the negative y side of T4 and on the positive y side of T3 then elsewhere. This skewing is presumably produced by the mean clockwise secondary flow field produced by the vortex pair, Figure 3.1.

We close our discussion with some general observations about the wave-number frequency spectra.

1. None of the spectra bear much if any resemblance to the von Karman spectrum—the anisotropy, inhomogeneity and organized turbulent eddies have a substantial, if not dominant effect on the spectrum.

2. Almost all the spectra measured outside the vortex cores bear close similarity to those measured across the span of a two-dimensional turbulent wake, despite a quite different flow structure. In particular the appearance of coherent eddies in these spectra appears very similar. This similarity may indicate some insensitivity of the wave-number frequency spectrum to local conditions which is a result that may be useful in future modeling efforts.

3. The wave-number frequency spectra of different components can vary greatly, suggesting that in inhomogenous flows it may not be possible to infer the behavior of one component (*e.g.* the upwash) from another (*e.g.* the streamwise).

4. As a whole the wave-number frequency spectra appear to have smaller spanwise than streamwise length scales, leading to spectra that appear stretched in the k_y direction.

Quantity	Uncertainty	
	Wake	Core
U/U_∞	0.015	0.015
V/U_∞	0.015	0.015
W/U_∞	0.015	0.015
$\overline{u^2}/U_\infty^2$	3.1×10^{-6}	1.4×10^{-5}
$\overline{v^2}/U_\infty^2$	9.5×10^{-6}	1.5×10^{-5}
$\overline{w^2}/U_\infty^2$	9.9×10^{-6}	2.0×10^{-5}
$\overline{uv}/U_\infty^2$	4.3×10^{-6}	1.4×10^{-5}
$\overline{vw}/U_\infty^2$	4.5×10^{-6}	2.3×10^{-5}
$\overline{uw}/U_\infty^2$	2.9×10^{-6}	8.5×10^{-6}

Table 3.1: Uncertainties in single point velocity measurements calculated for 20:1 odds at typical locations in wake and core regions

	r_1/c	V_{θ_1}/c	U_d/U_∞	$\Gamma_1/(U_\infty c)$	Ro
Generator blade vortex	0.049	0.215	0.147	0.066	0.68
Interaction blade vortex	0.074	0.132	0.103	0.061	0.78

Table 3.2: Vortex core parameters corrected for wandering at $x/c = 30$

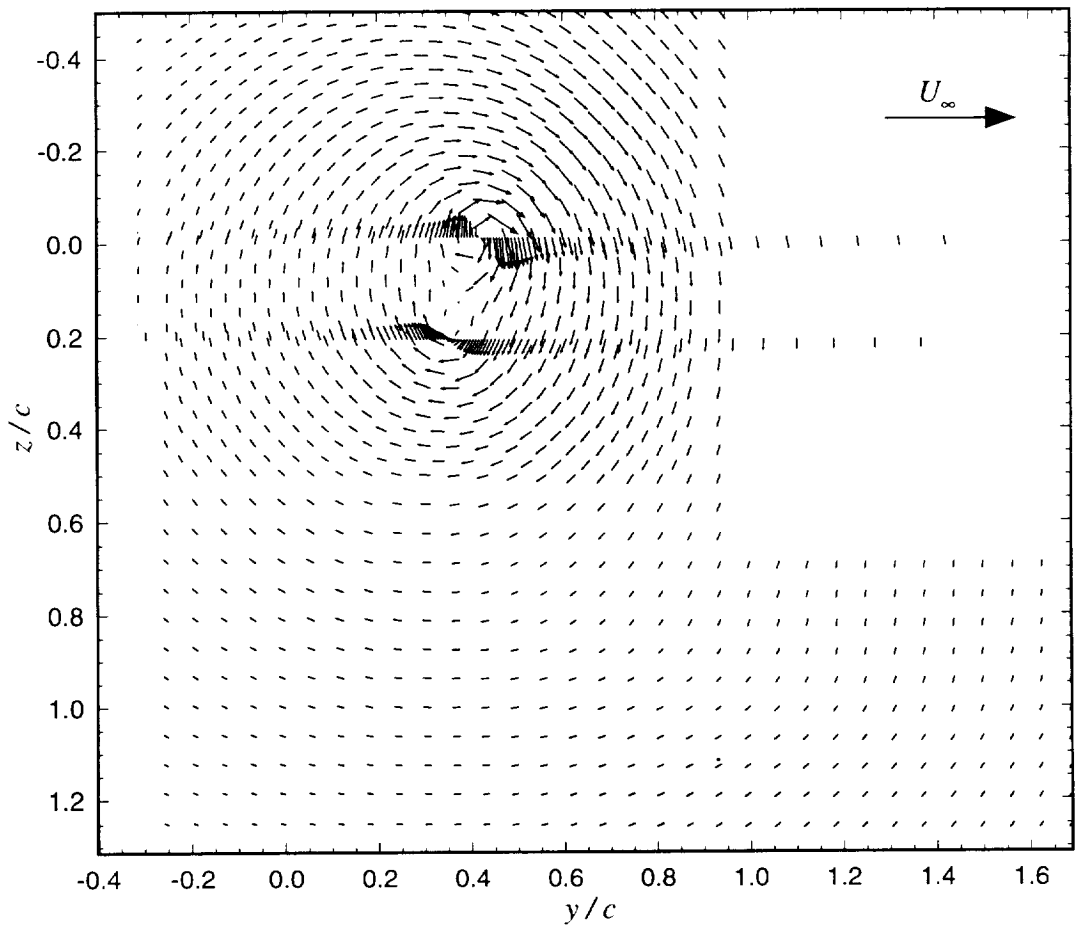

Figure 3.1: Mean cross flow velocity vectors

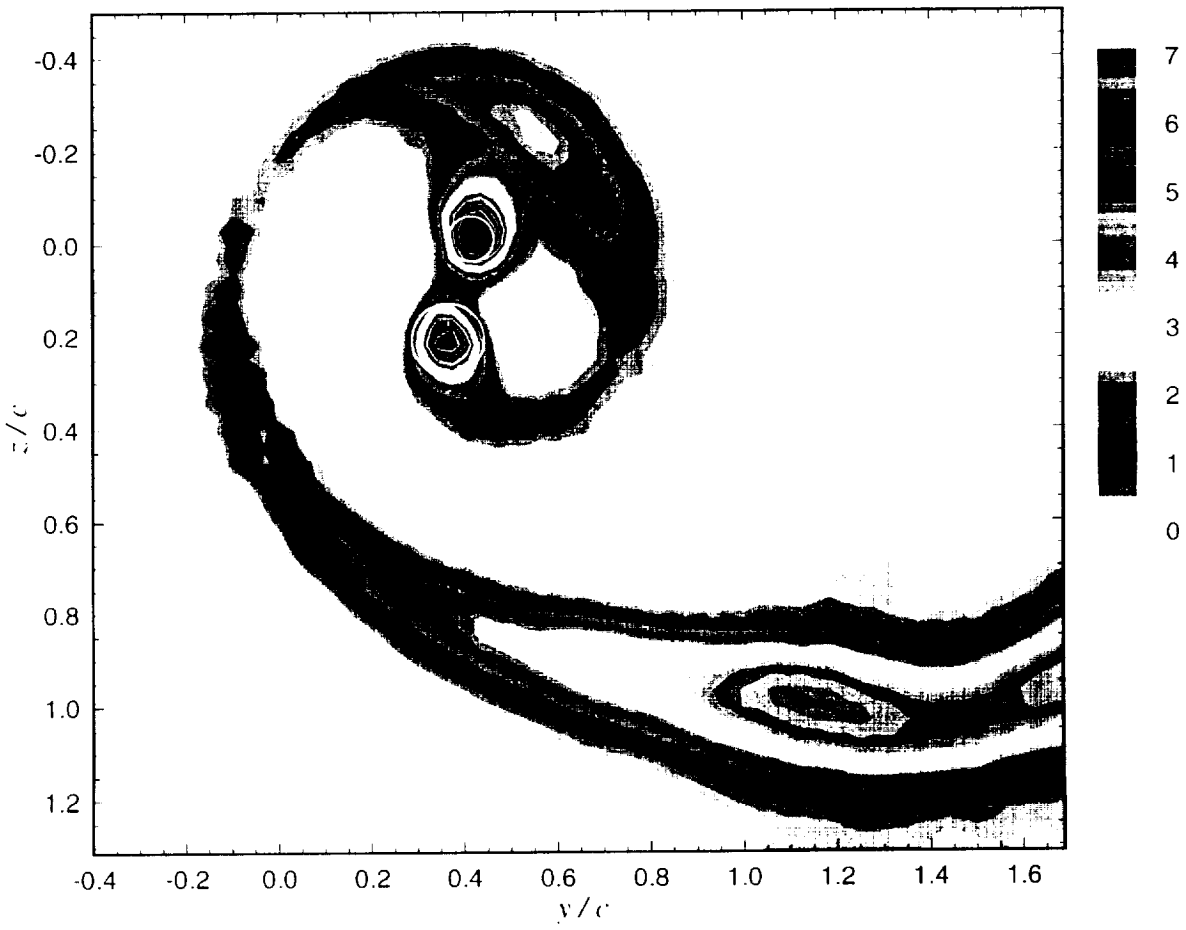

Figure 3.2: Contours of mean axial velocity deficit, $(1 - U/U_\infty) \times 100$. Circles estimate core edges.

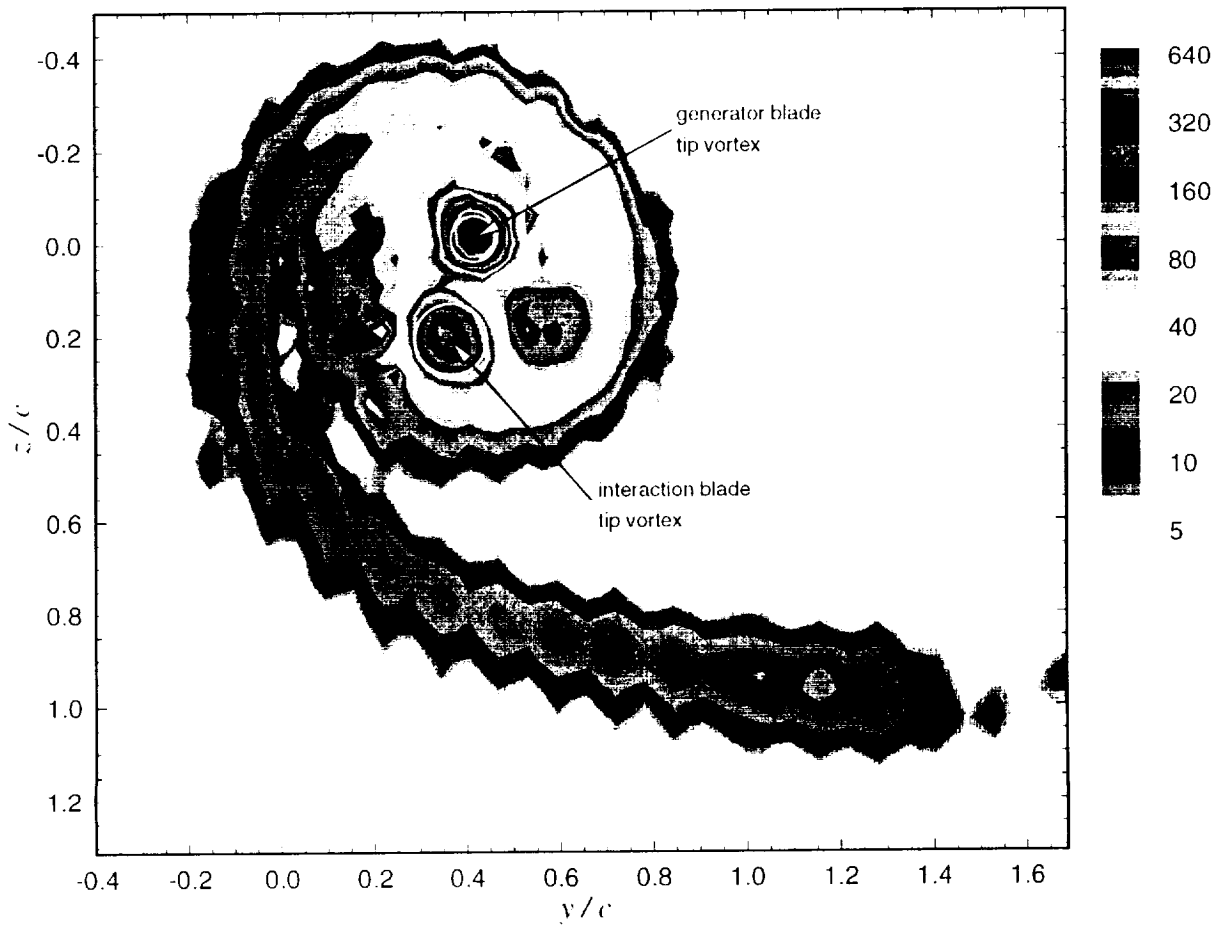

Figure 3.3: Contours of mean streamwise vorticity, $\Omega_x c/U_\infty \times 100$. Circles estimate core edges.

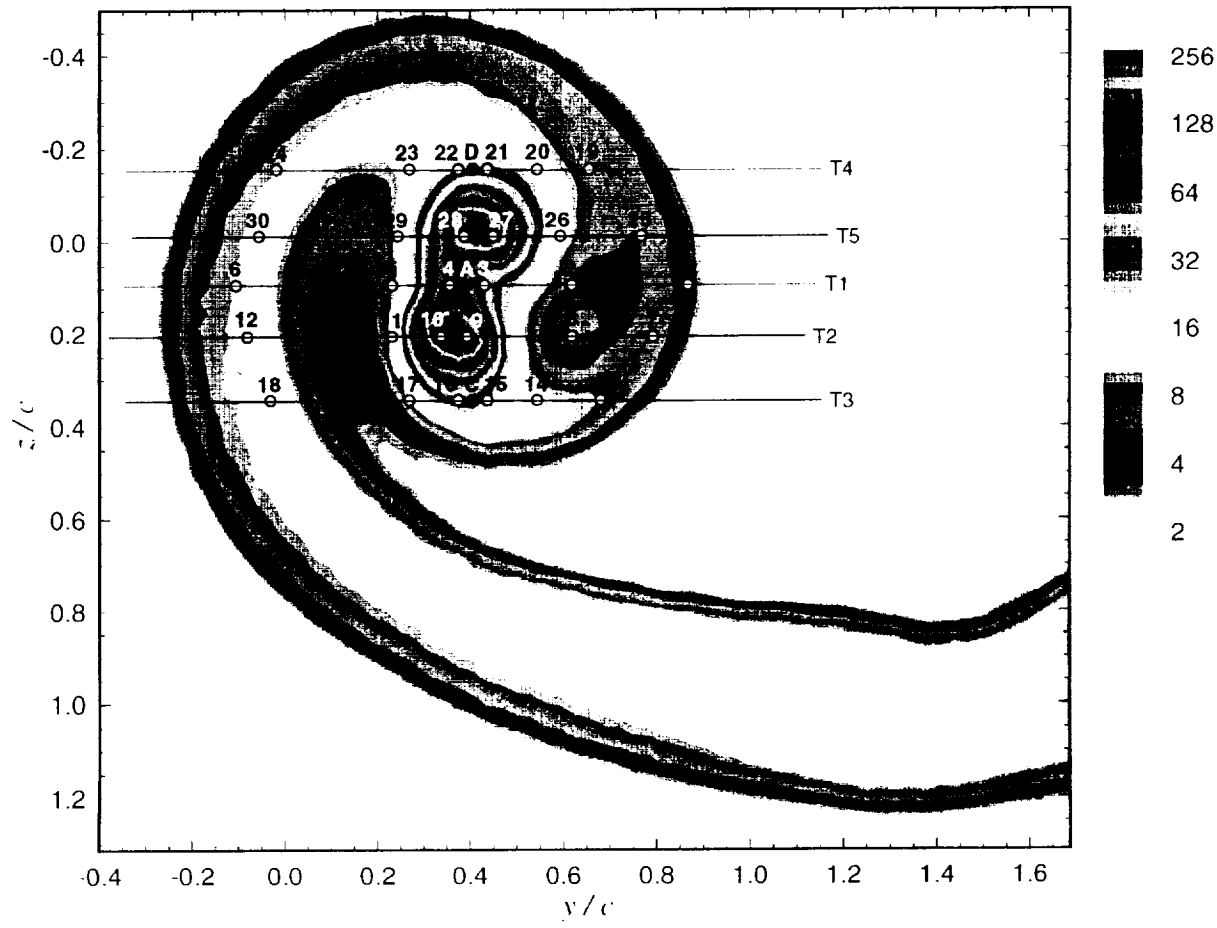

Figure 3.4: Contours of axial normal turbulence stress, $\overline{u^2}/U_\infty^2 \times 10^5$

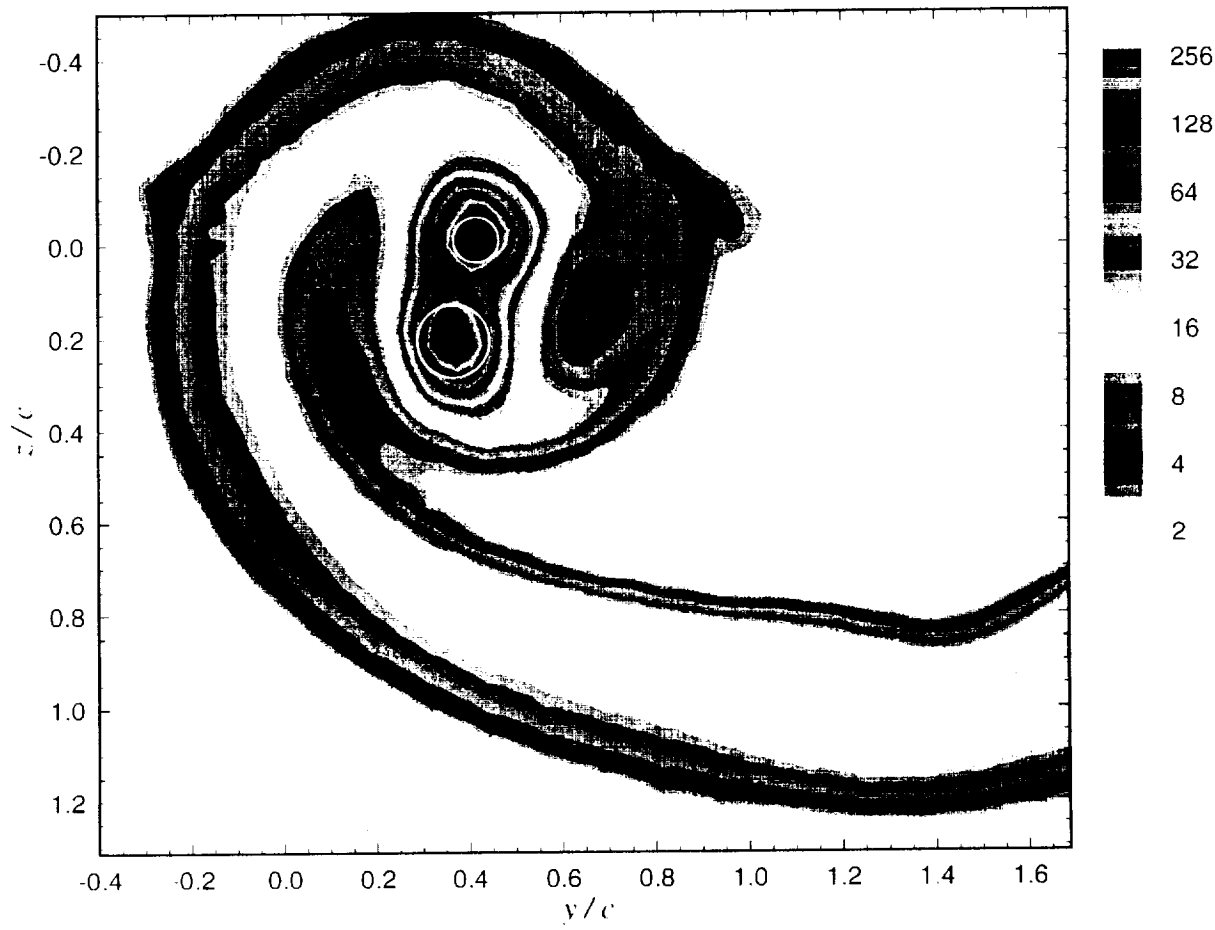

Figure 3.5: Contours of summed cross flow normal turbulent stresses, $\frac{1}{2}(\overline{v^2} + \overline{w^2})/U_\infty^2 \times 10^5$. Circles estimate core edges.

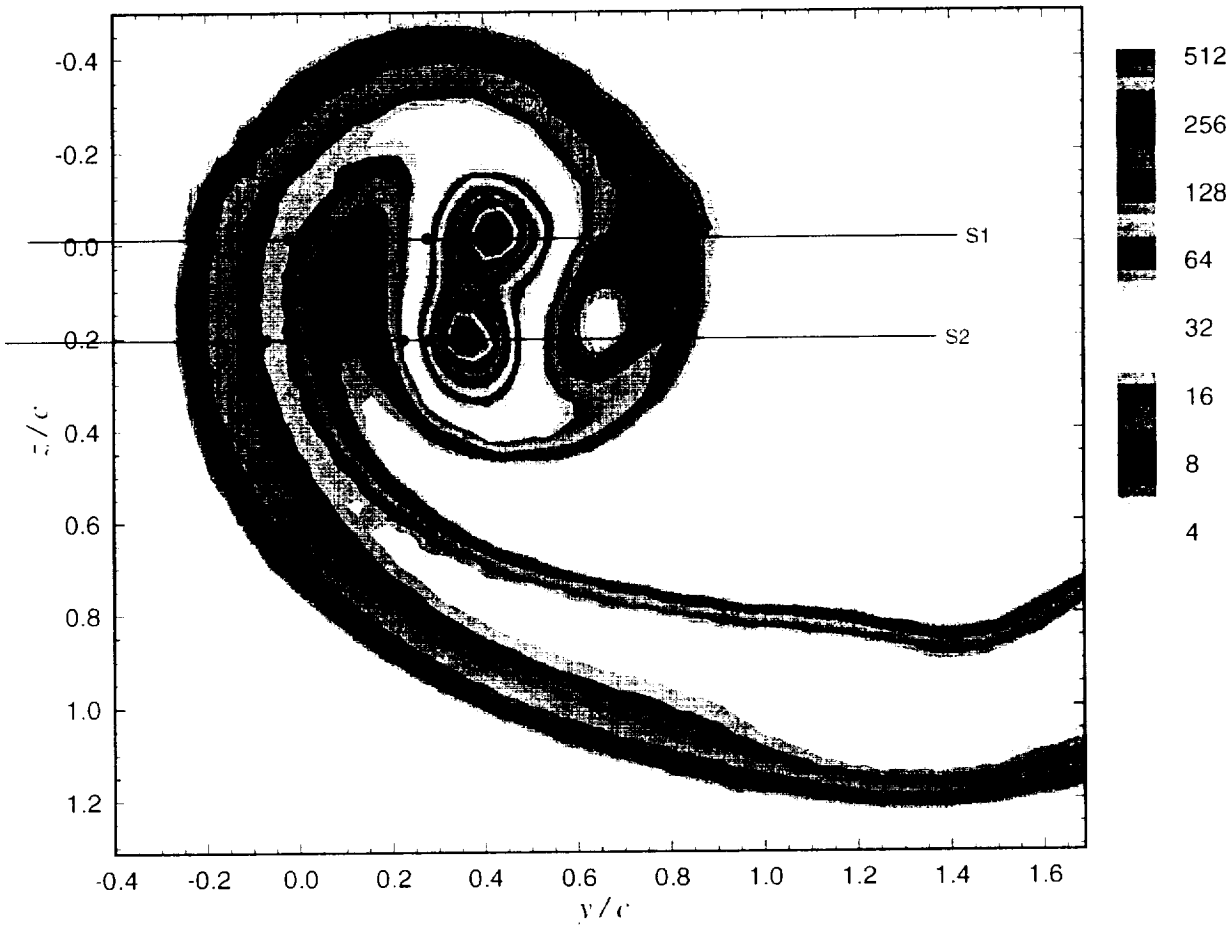

Figure 3.6: Contours of turbulence kinetic energy, $k/U_\infty^2 \times 10^5$

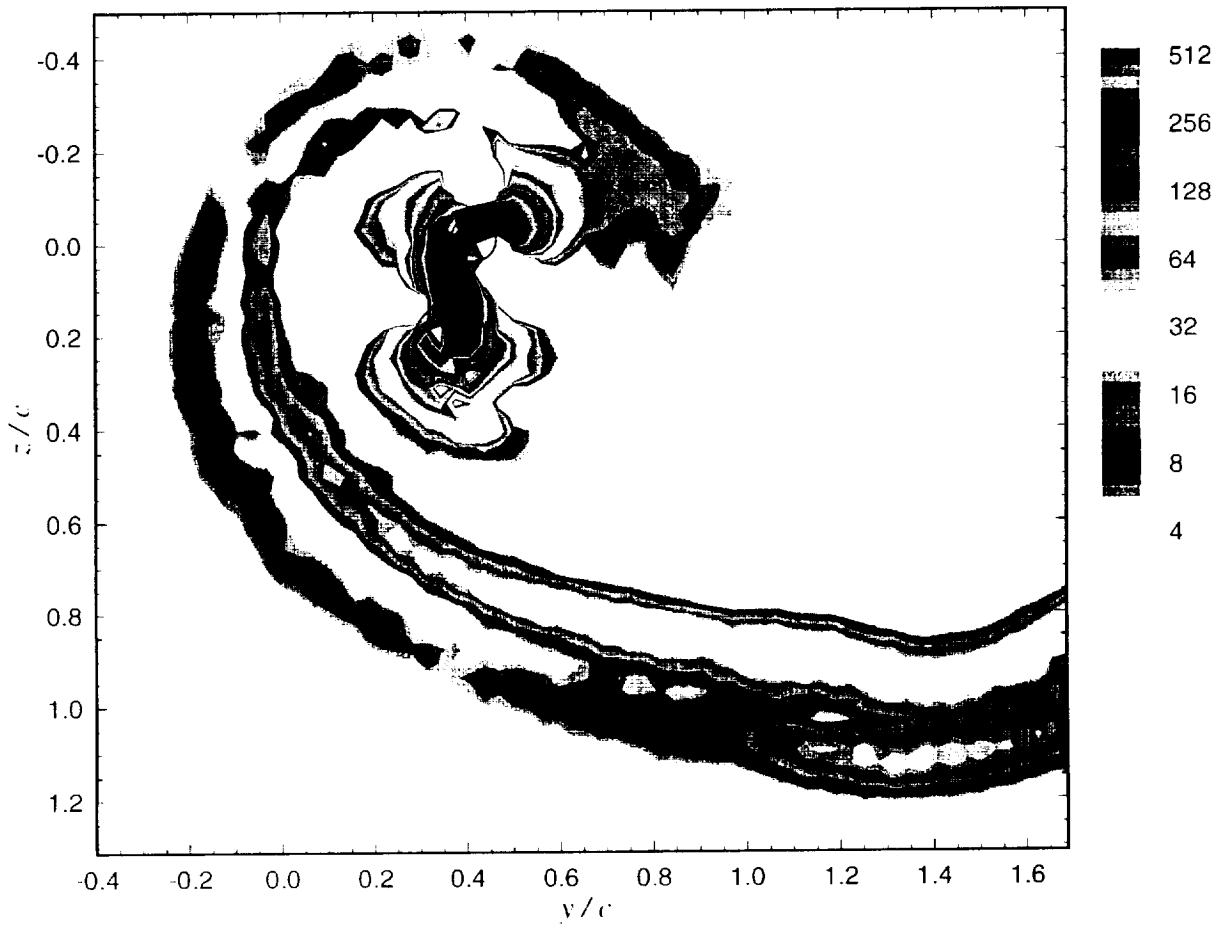

Figure 3.7: Contours of turbulence kinetic energy production, $Pc/U_\infty^3 \times 10^6$. Circles estimate core edges.

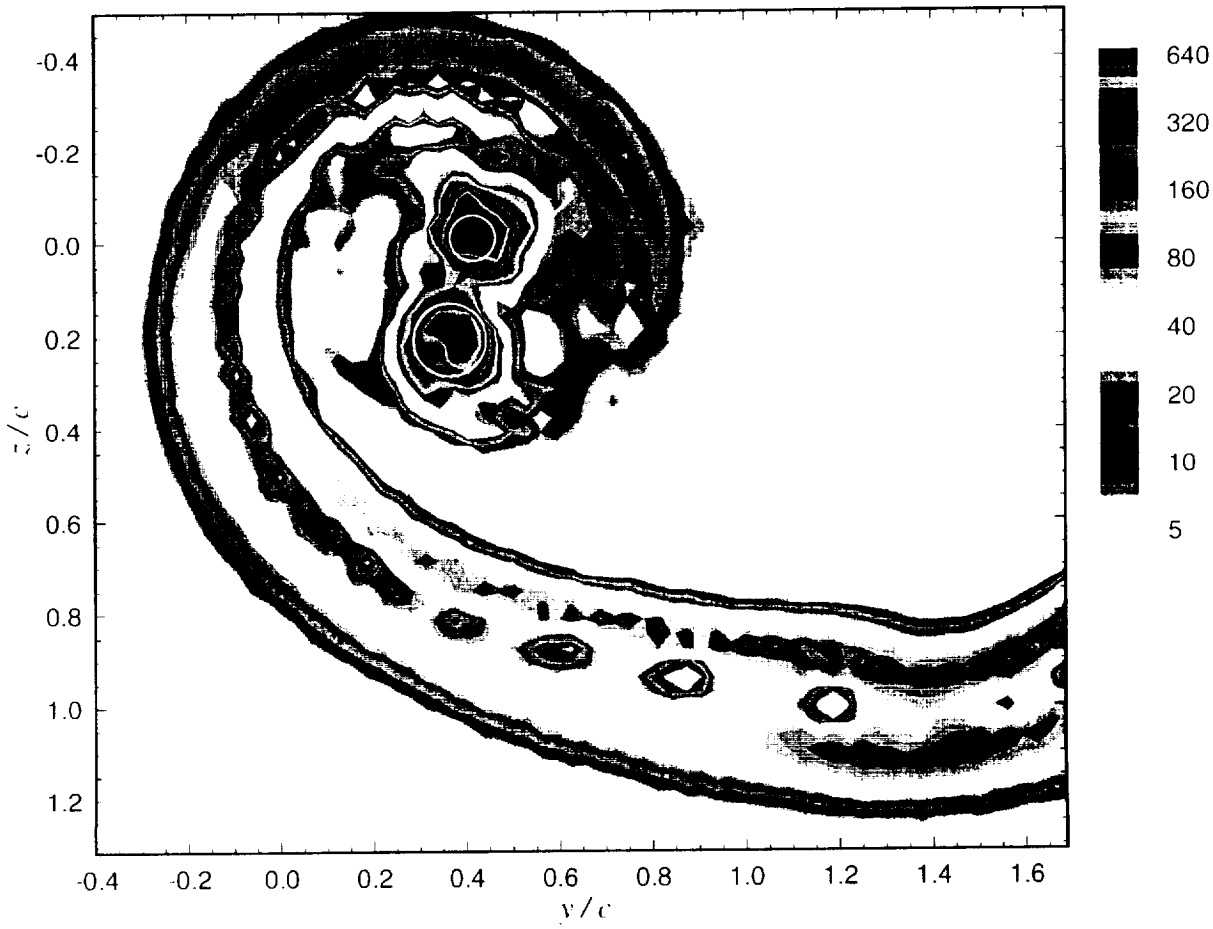

Figure 3.8: Contours of axial shear stress magnitude, $\tau_x/U_\infty^2 \times 10^6$. Circles estimate core edges.

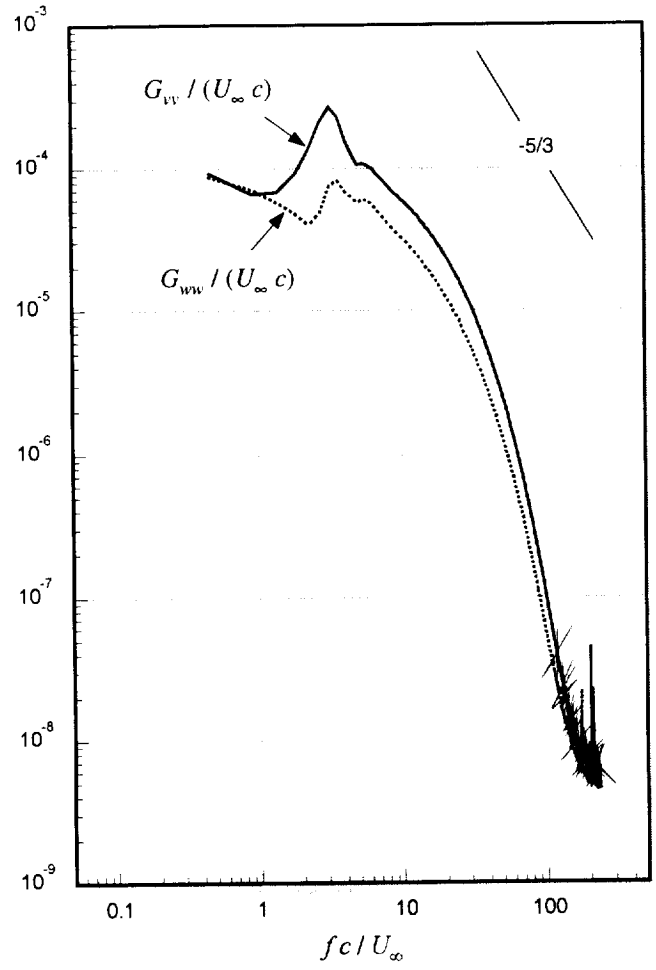

Figure 3.9: Velocity autospectra at location B between the vortex cores shown in Figure 3.4

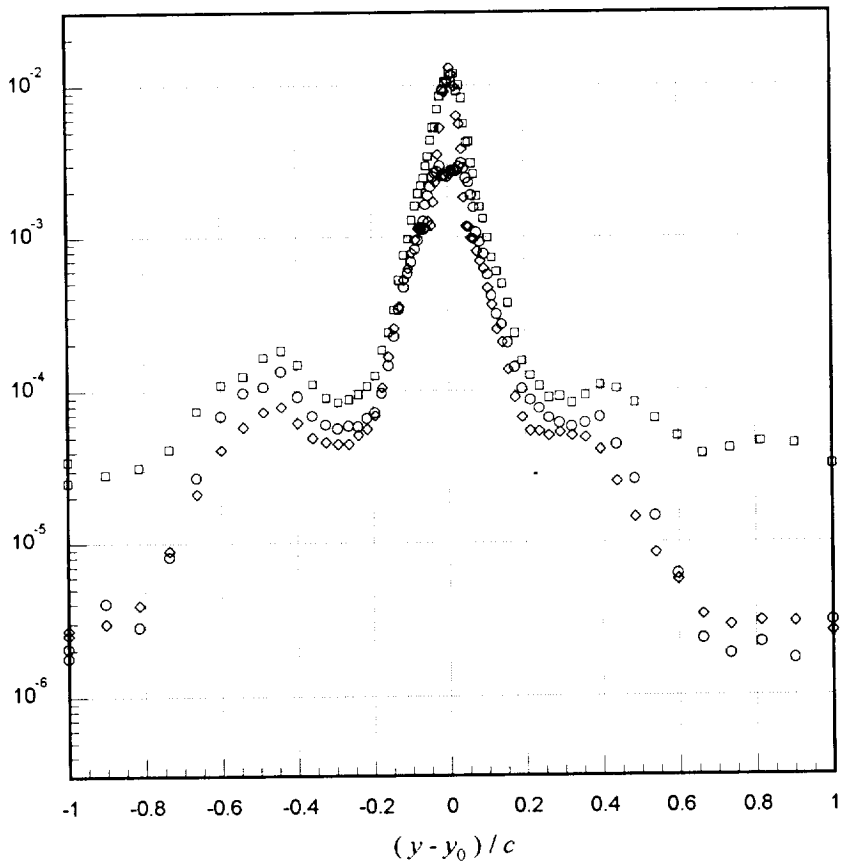

Figure 3.10: Normal stresses ($\overline{u^2}/U_\infty^2 = \bigcirc$, $\overline{v^2}/U_\infty^2 = \square$, $\overline{w^2}/U_\infty^2 = \diamond$) measured along the profile S1 (see Figure 3.6) through the generator blade tip vortex core. Unfiltered data.

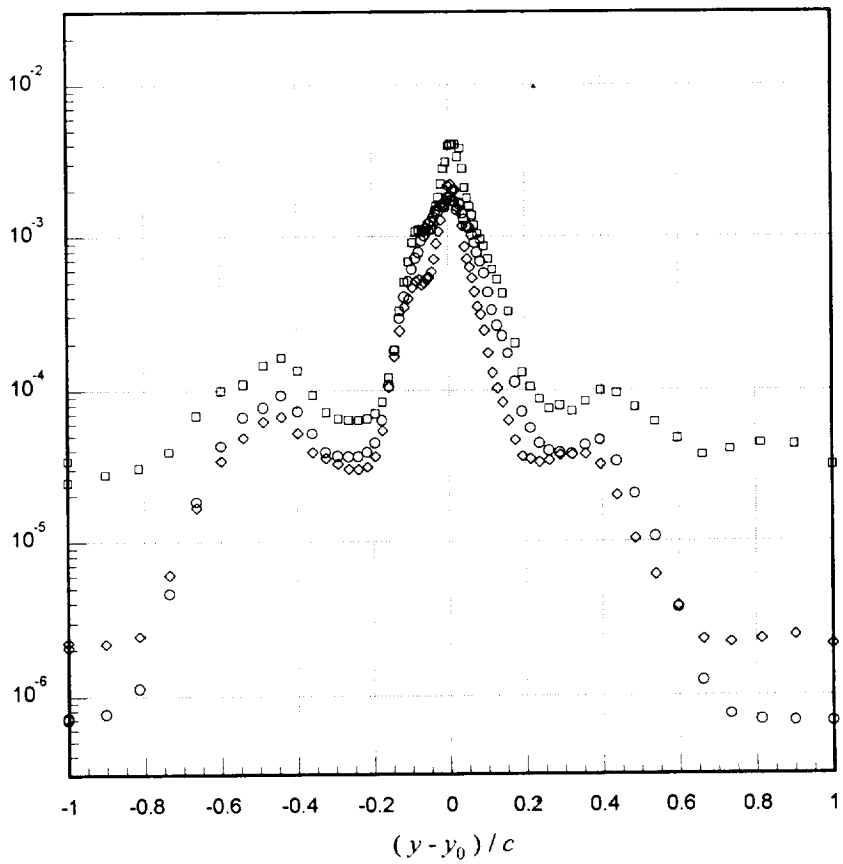

Figure 3.11: Normal stresses ($\overline{u^2}/U_\infty^2 = \bigcirc$, $\overline{v^2}/U_\infty^2 = \square$, $\overline{w^2}/U_\infty^2 = \diamond$) measured along the profile S1 (see Figure 3.6) through the generator blade tip vortex core. Data high-pass filtered at $fc/U_\infty = 1.4$.

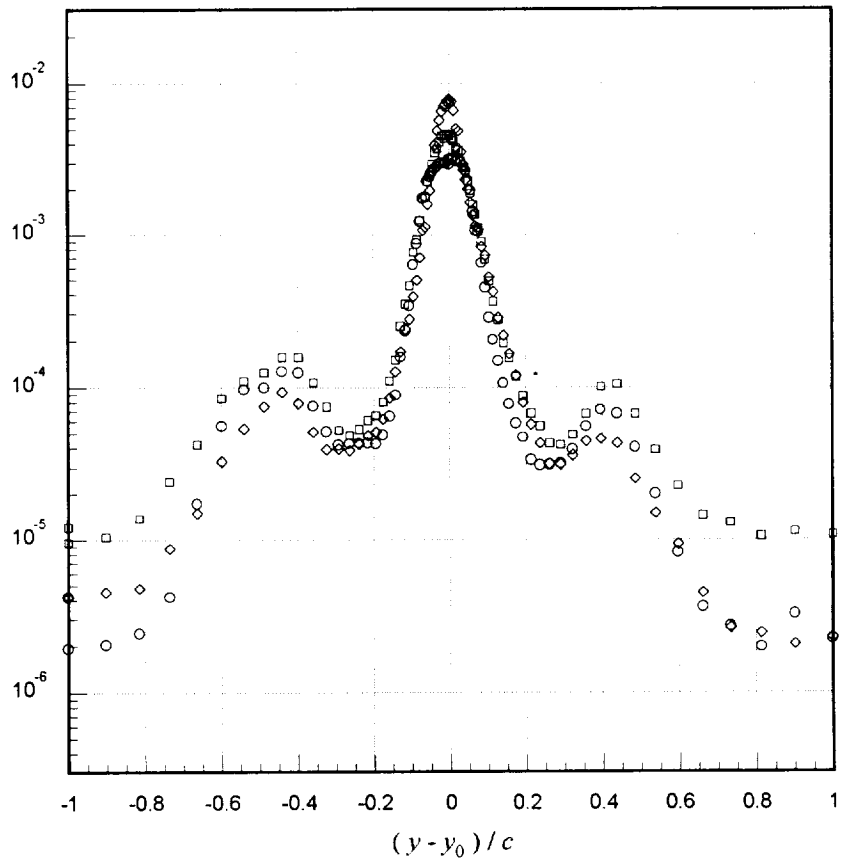

Figure 3.12: Normal stresses ($\overline{u^2}/U_\infty^2 = \bigcirc$, $\overline{v^2}/U_\infty^2 = \square$, $\overline{w^2}/U_\infty^2 = \diamond$) measured along the profile S2 (see Figure 3.6) through the interaction blade tip vortex core. Unfiltered data.

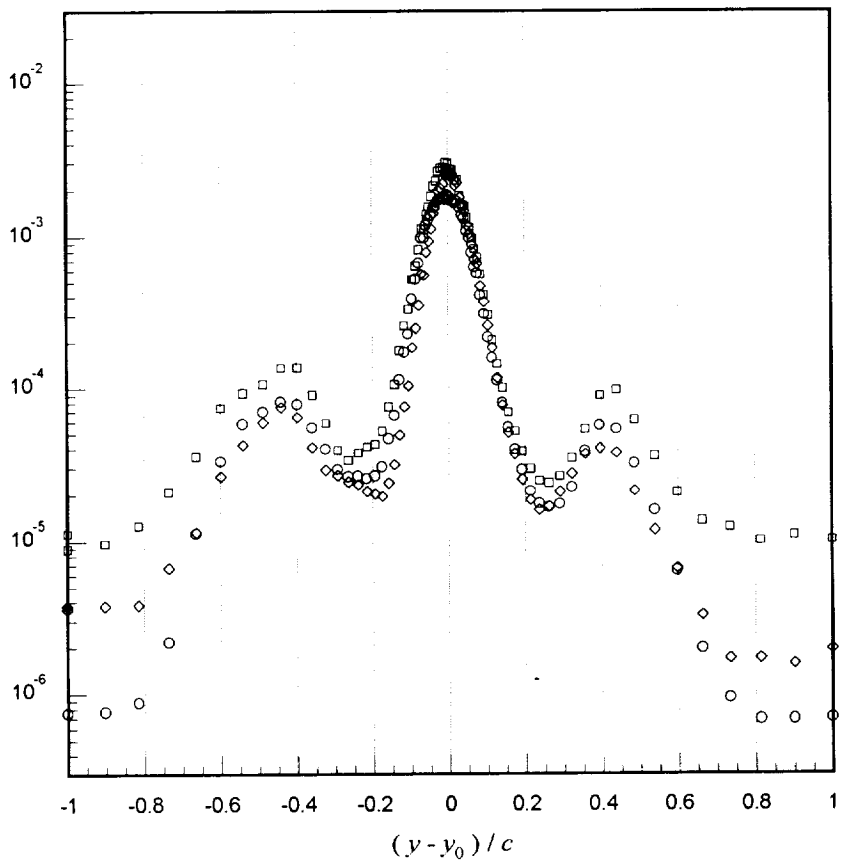

Figure 3.13: Normal stresses ($\overline{u^2}/U_\infty^2 = \bigcirc$, $\overline{v^2}/U_\infty^2 = \square$, $\overline{w^2}/U_\infty^2 = \diamond$) measured along the profile S2 (see Figure 3.6) through the interaction blade tip vortex core. Data high-pass filtered at $fc/U_\infty = 1.4$.

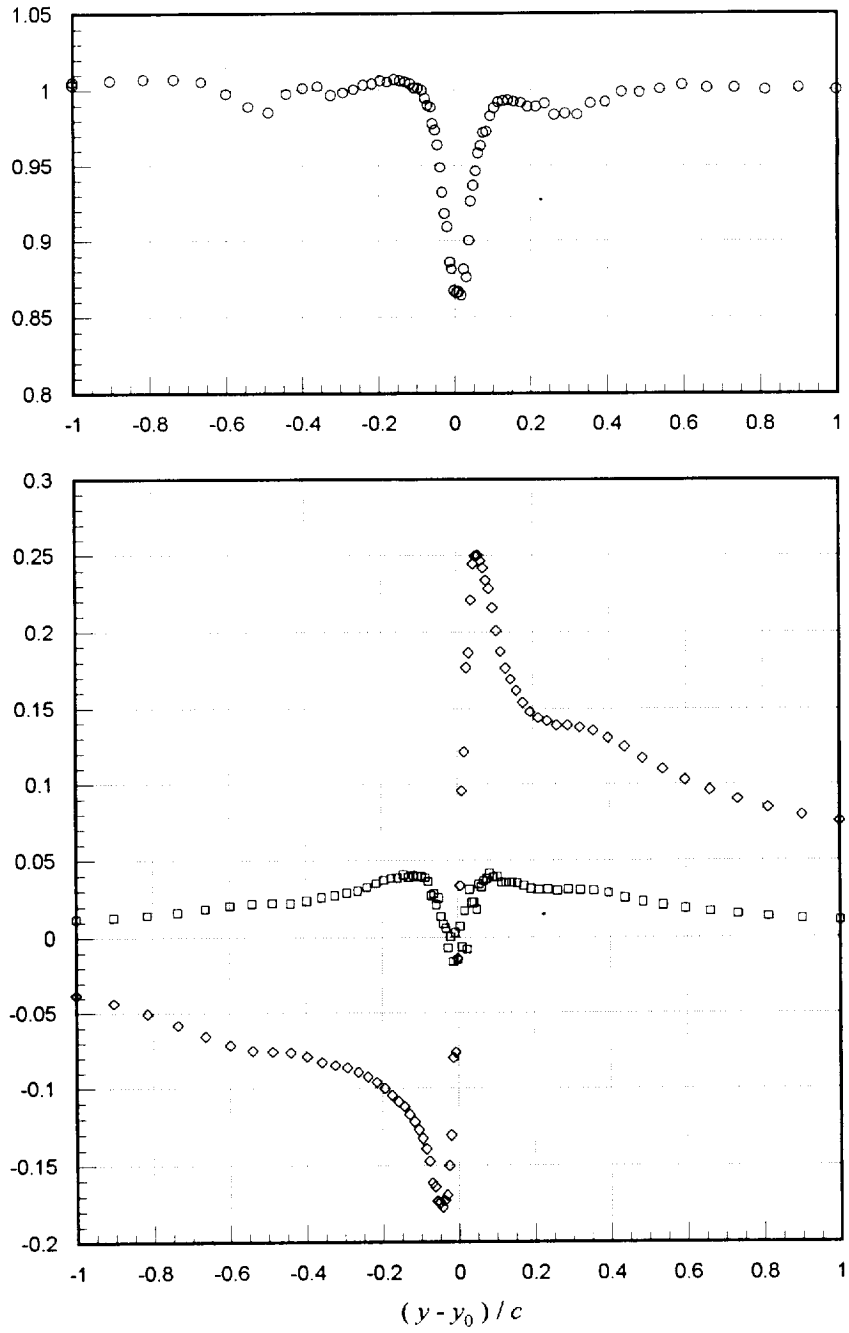

Figure 3.14: Mean velocities ($U/U_\infty = \bigcirc$, $V/U_\infty = \square$, $W/U_\infty = \diamond$) measured along the profile S1 (see Figure 3.6) through the generator blade tip vortex core

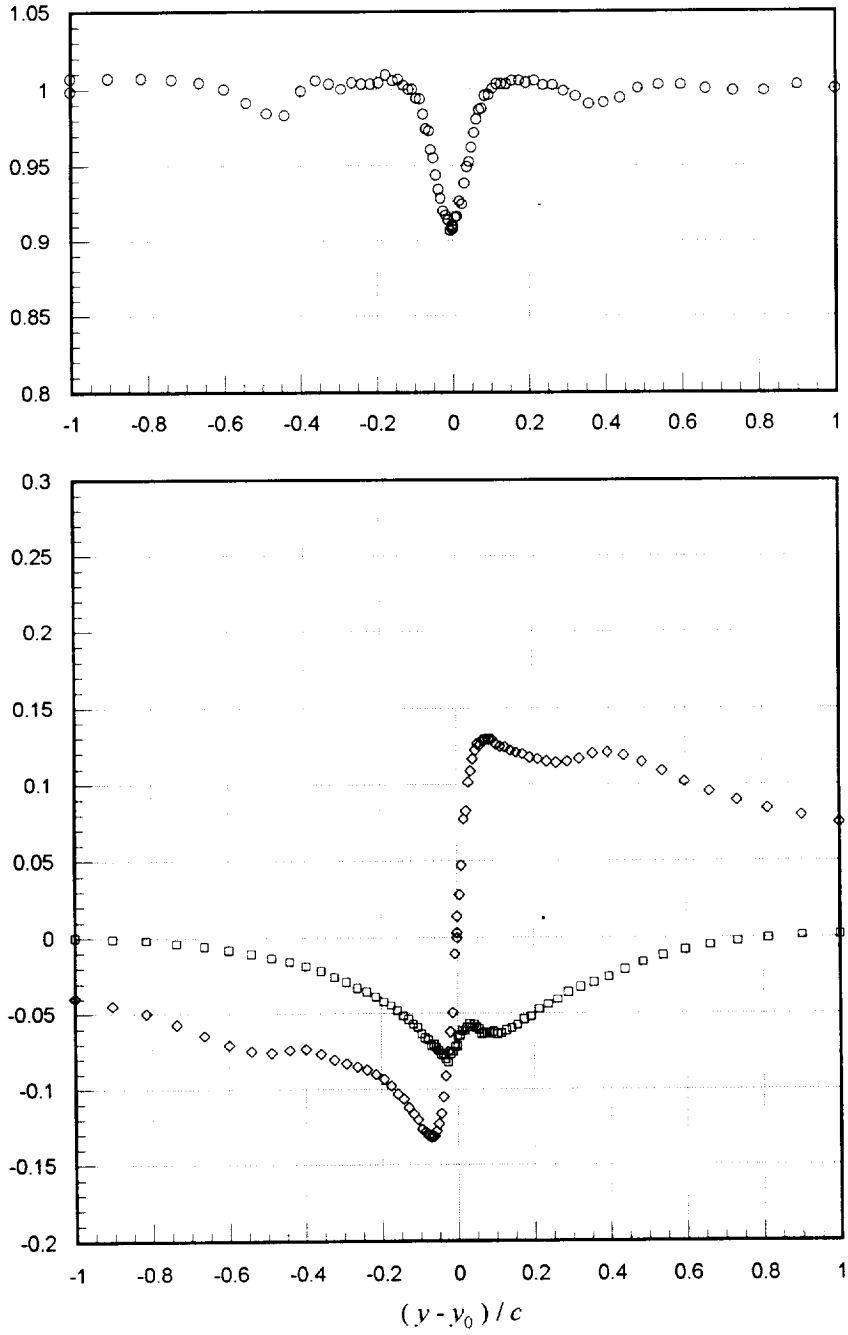

Figure 3.15: Mean velocities ($U/U_\infty = \bigcirc$, $V/U_\infty = \square$, $W/U_\infty = \diamond$) measured along the profile S2 (see Figure 3.6) through the interaction blade tip vortex core

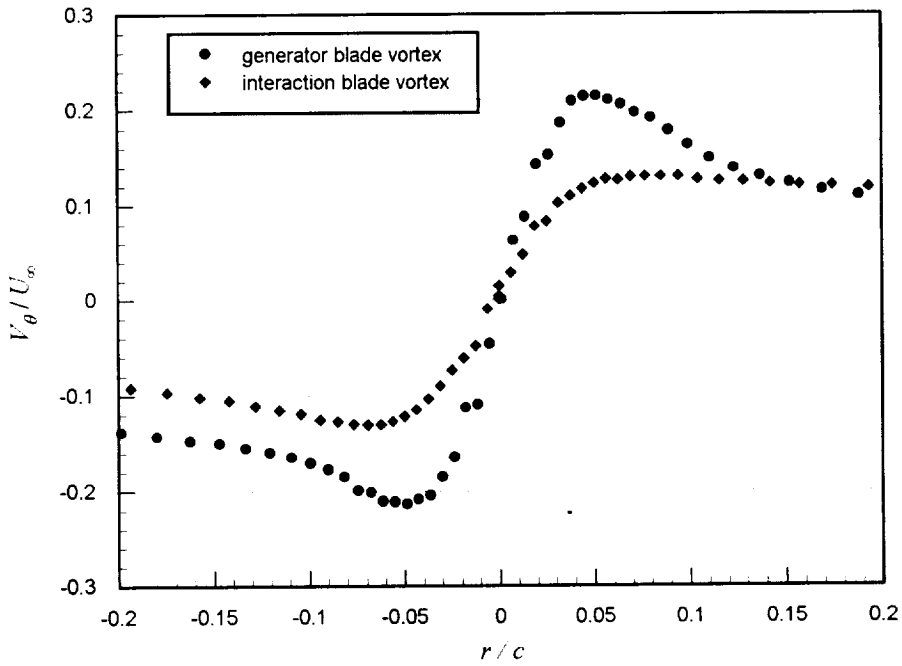

Figure 3.16: Vortex core tangential velocity field, $V_\theta(r)$, estimates from the profiles S1 and S2 shown in Figure 3.6

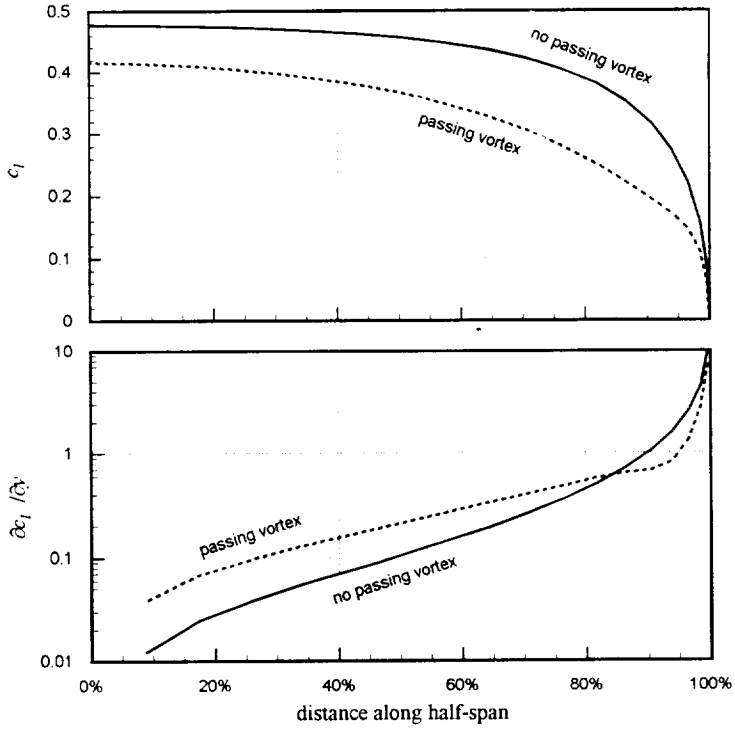

Figure 3.17: Lifting line theory estimates of interaction blade loading with and without passing vortex

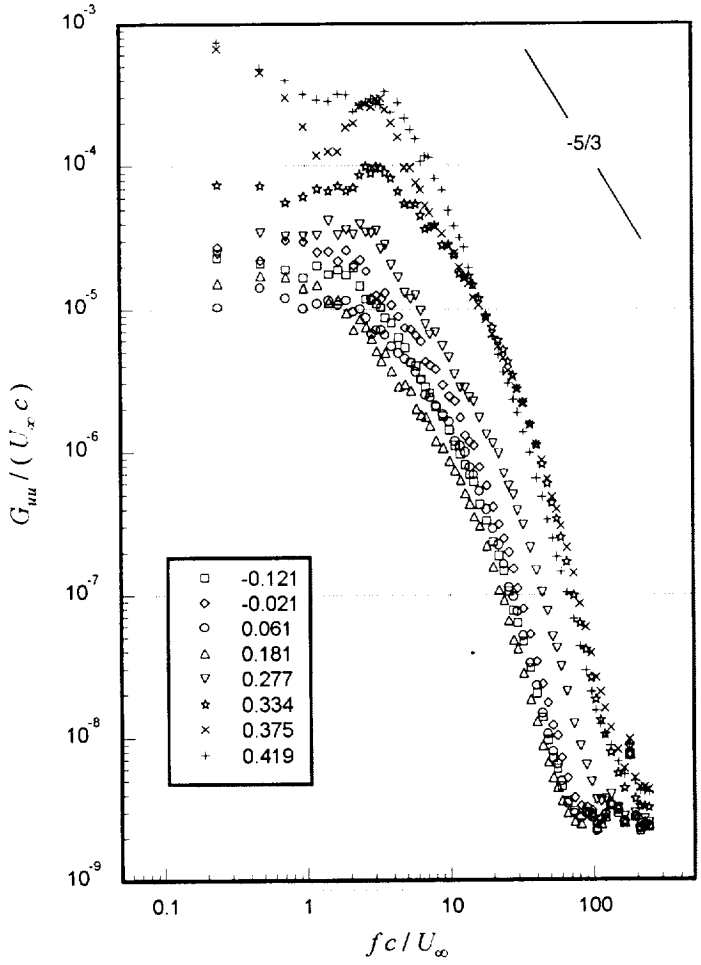

Figure 3.18: Axial component velocity autospectra at locations along the profile S1 shown in Figure 3.6 ($z/c = -0.013$). Legend lists y/c values.

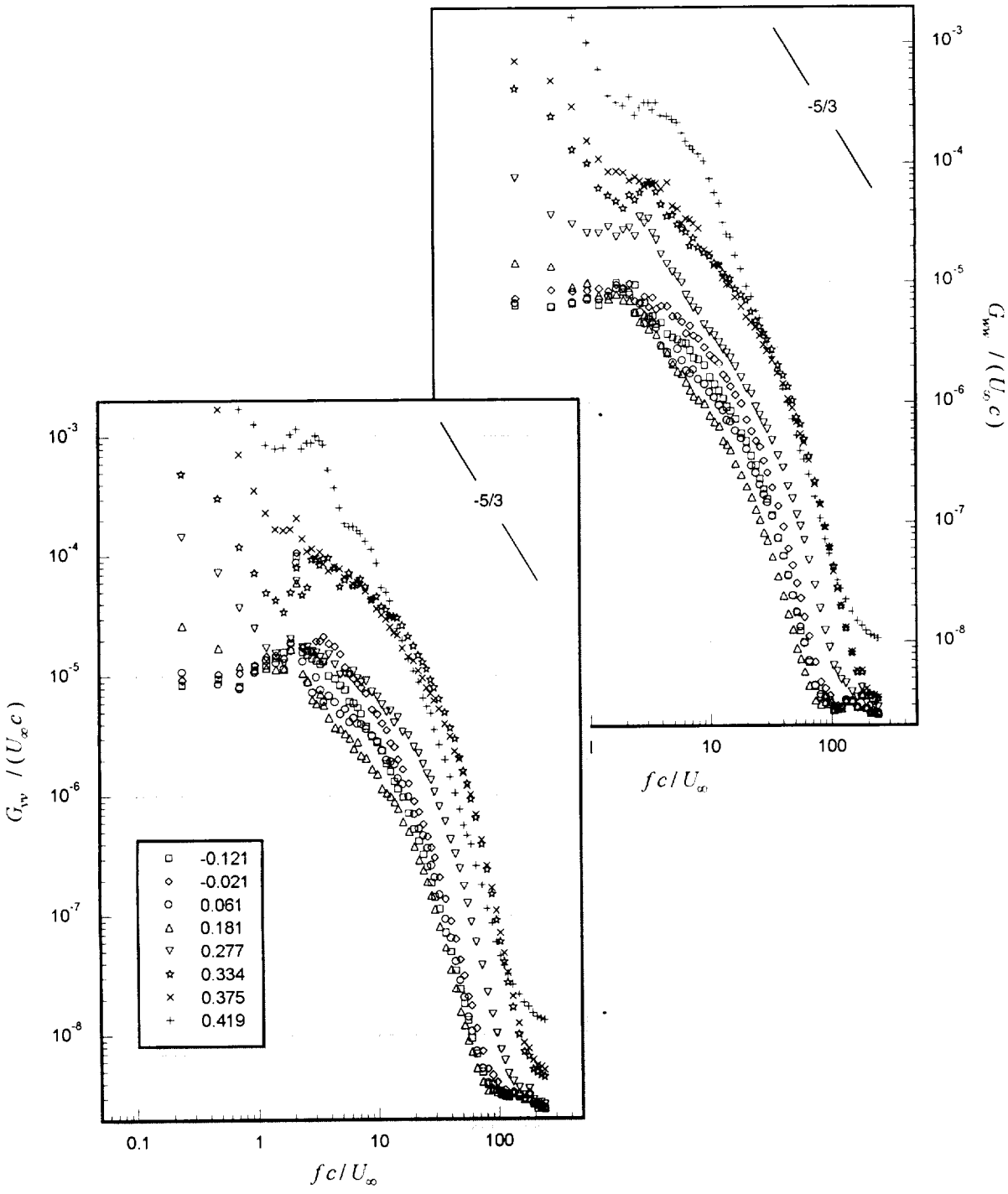

Figure 3.19: Axial component velocity autospectra at locations along the profile S1 shown in Figure 3.6 ($z/c = -0.013$). Legend lists y/c values.

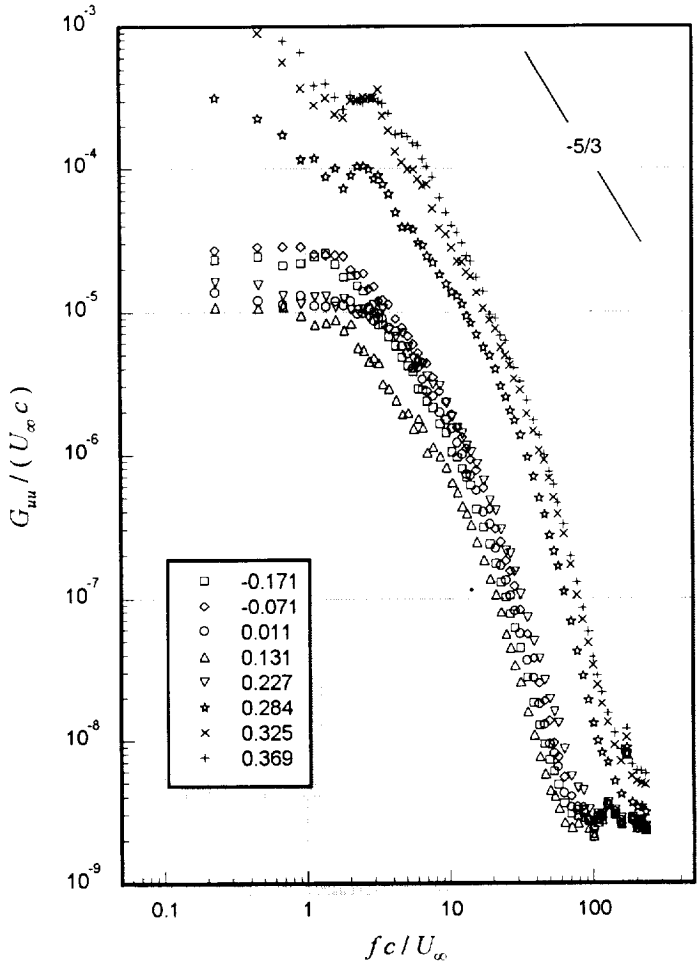

Figure 3.20: Axial component velocity autospectra at locations along the profile S2 shown in Figure 3.6 ($z/c = 0.206$). Legend lists y/c values.

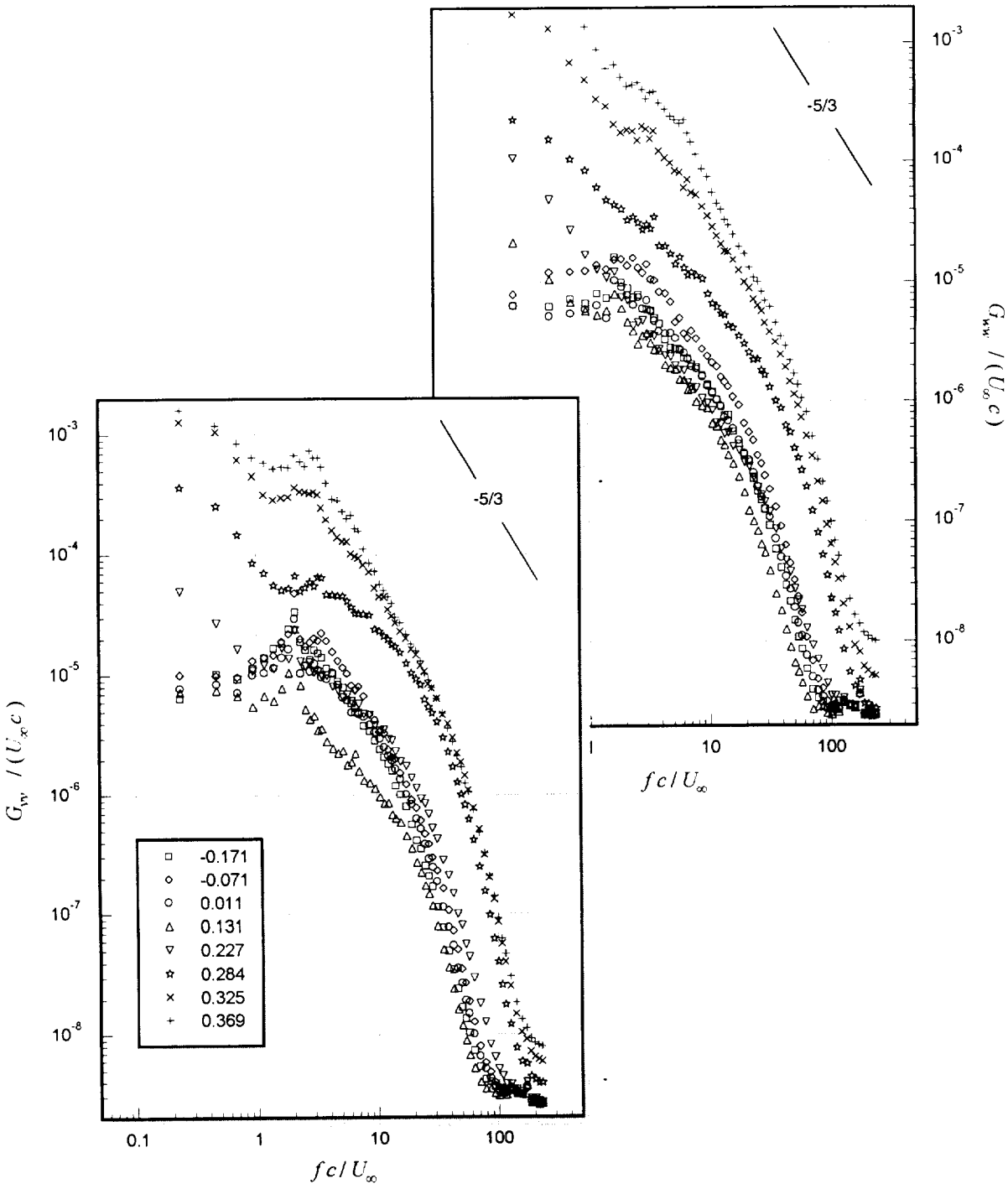

Figure 3.21: Axial component velocity autospectra at locations along the profile S1 shown in Figure 3.6 ($z/c = -0.013$). Legend lists y/c values.

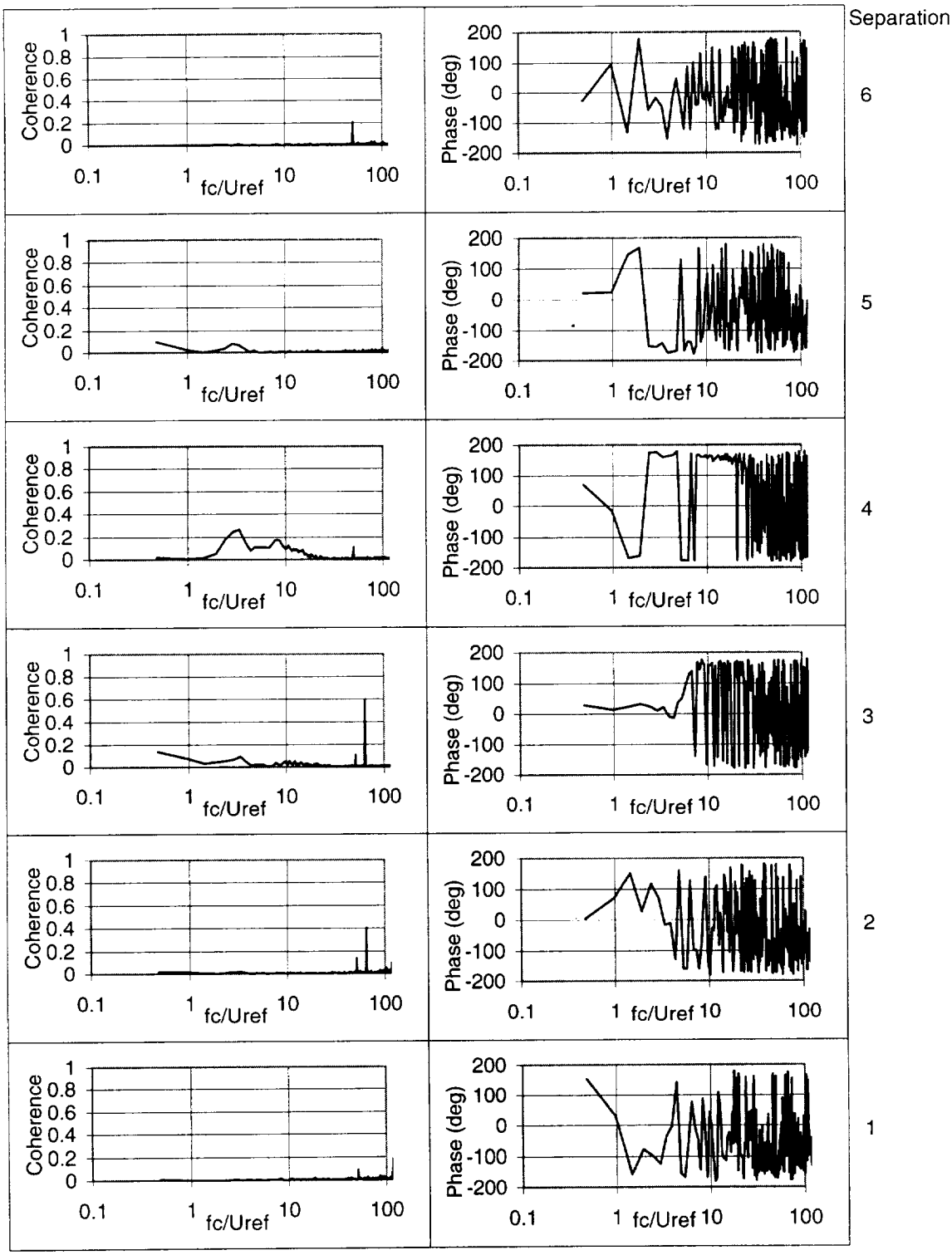

Figure 3.22: Coherence and phase between the axial (u) velocity component between selected locations along profile T1 and location A (see Figure 3.4)

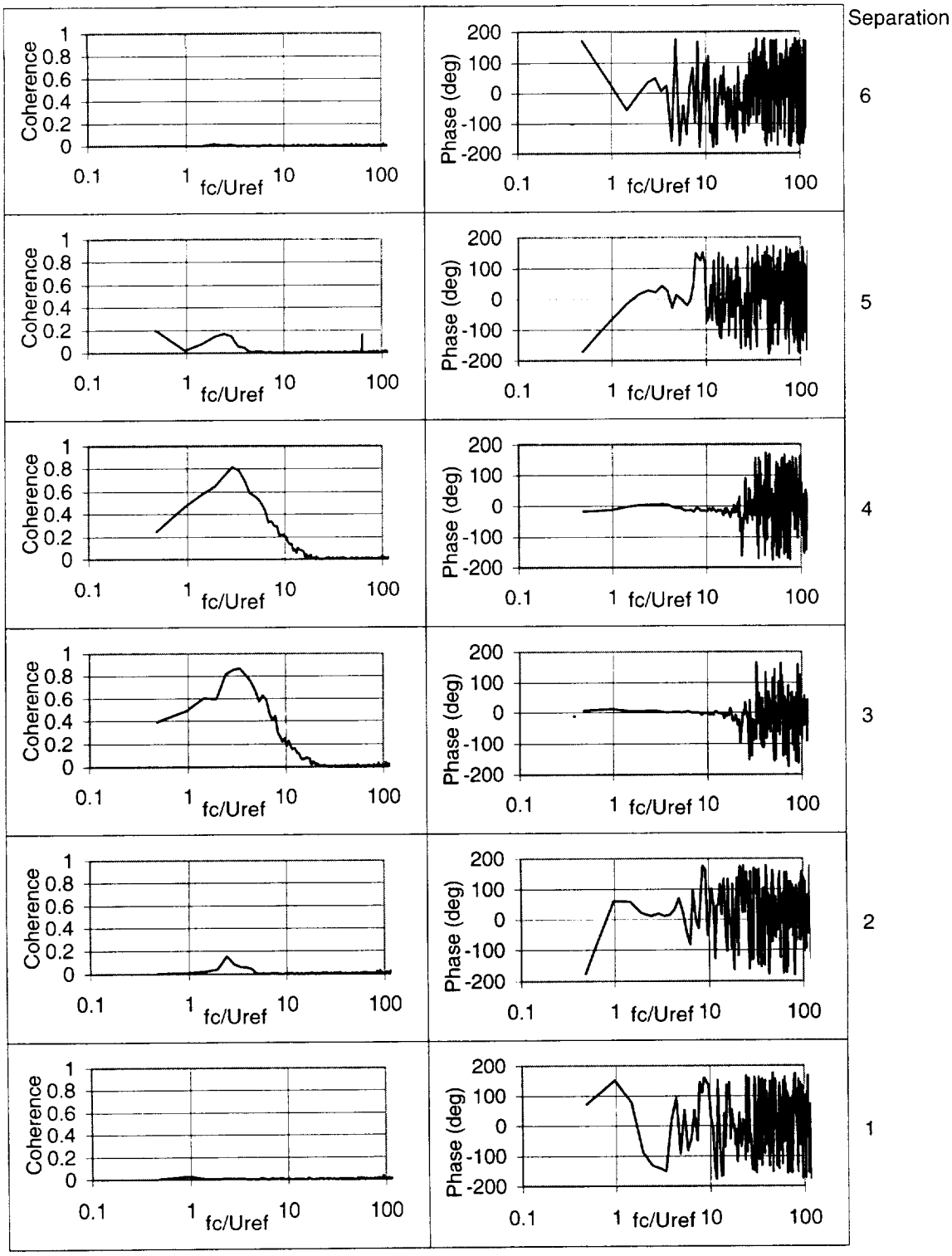

Figure 3.23: Coherence and phase between the spanwise (v) velocity component at selected locations along profile T1 and location A (see Figure 3.4)

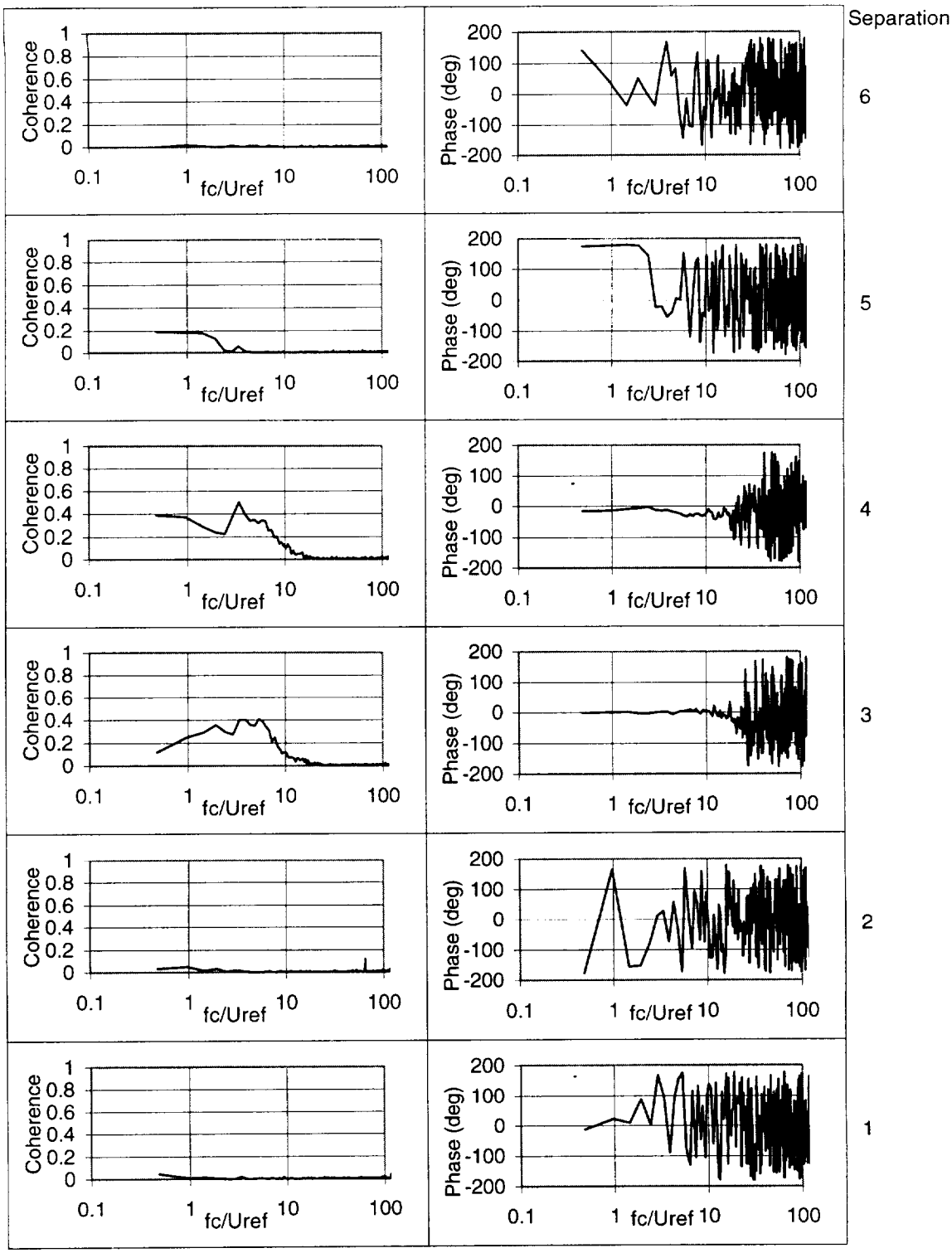

Figure 3.24: Coherence and phase between the upwash (w) velocity component at selected locations along profile T1 and location A (see Figure 3.4)

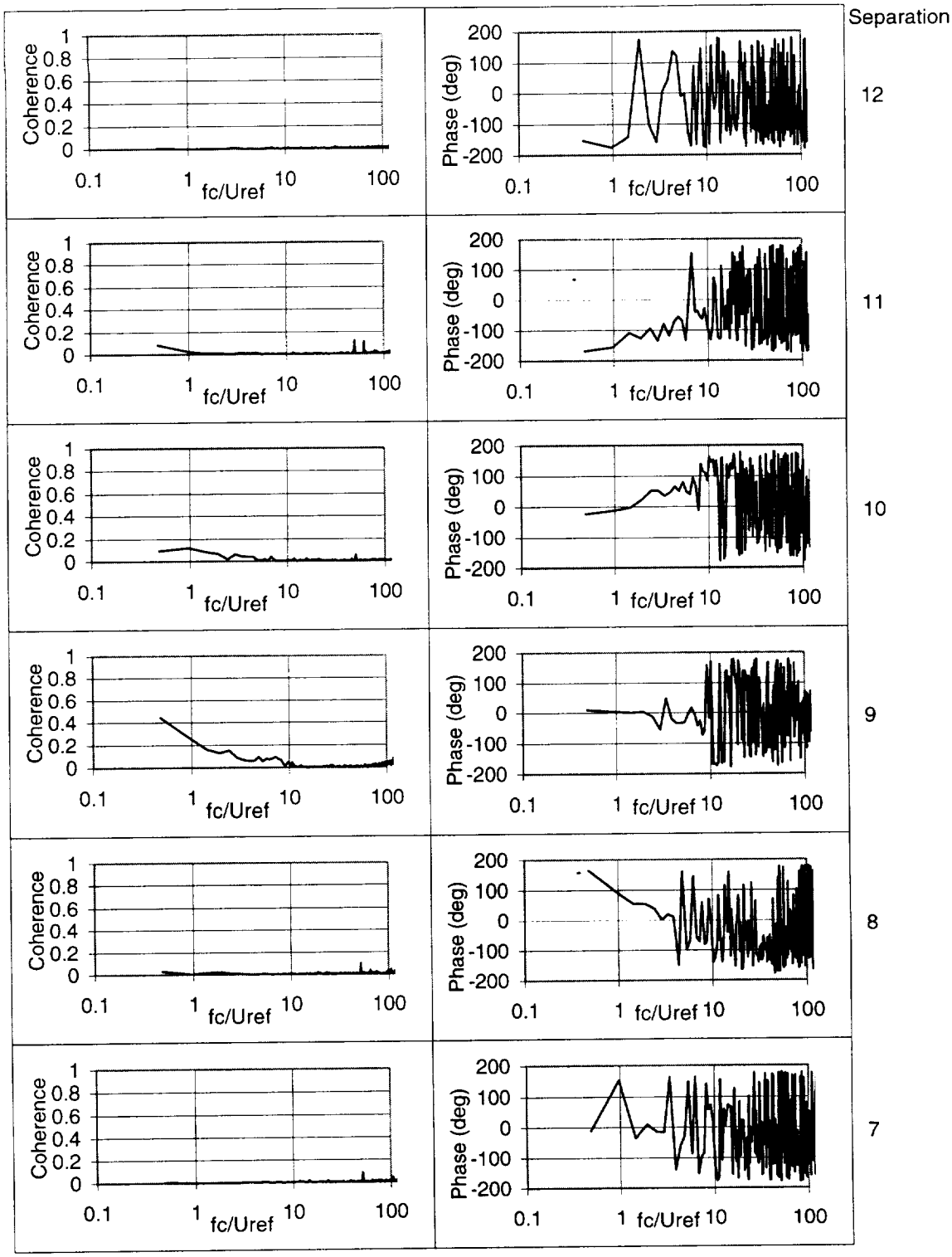

Figure 3.25: Coherence and phase between the axial (u) velocity component between selected locations along profile T2 and location B (see Figure 3.4)

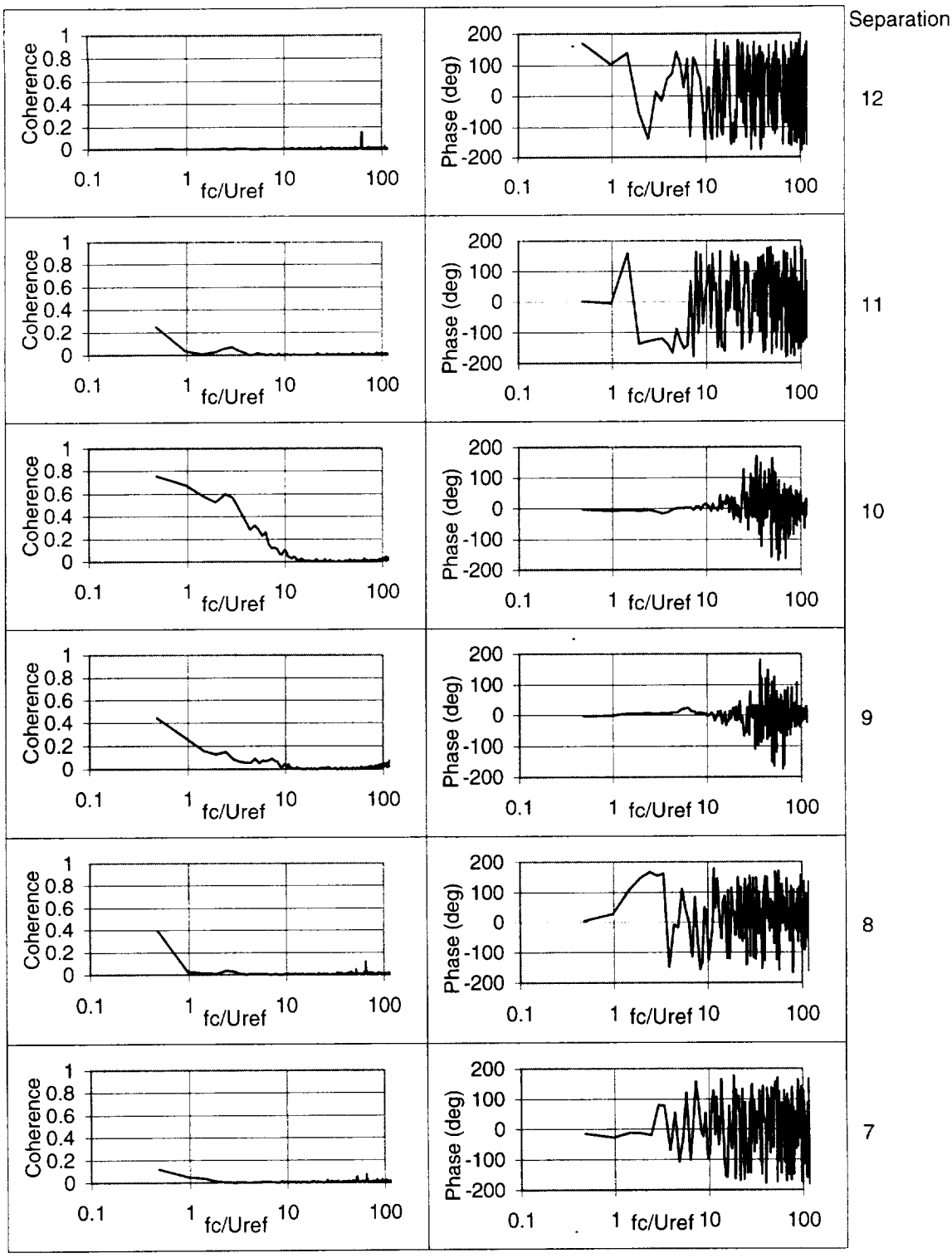

Figure 3.26: Coherence and phase between the spanwise (v) velocity component at selected locations along profile T2 and location B (see Figure 3.4)

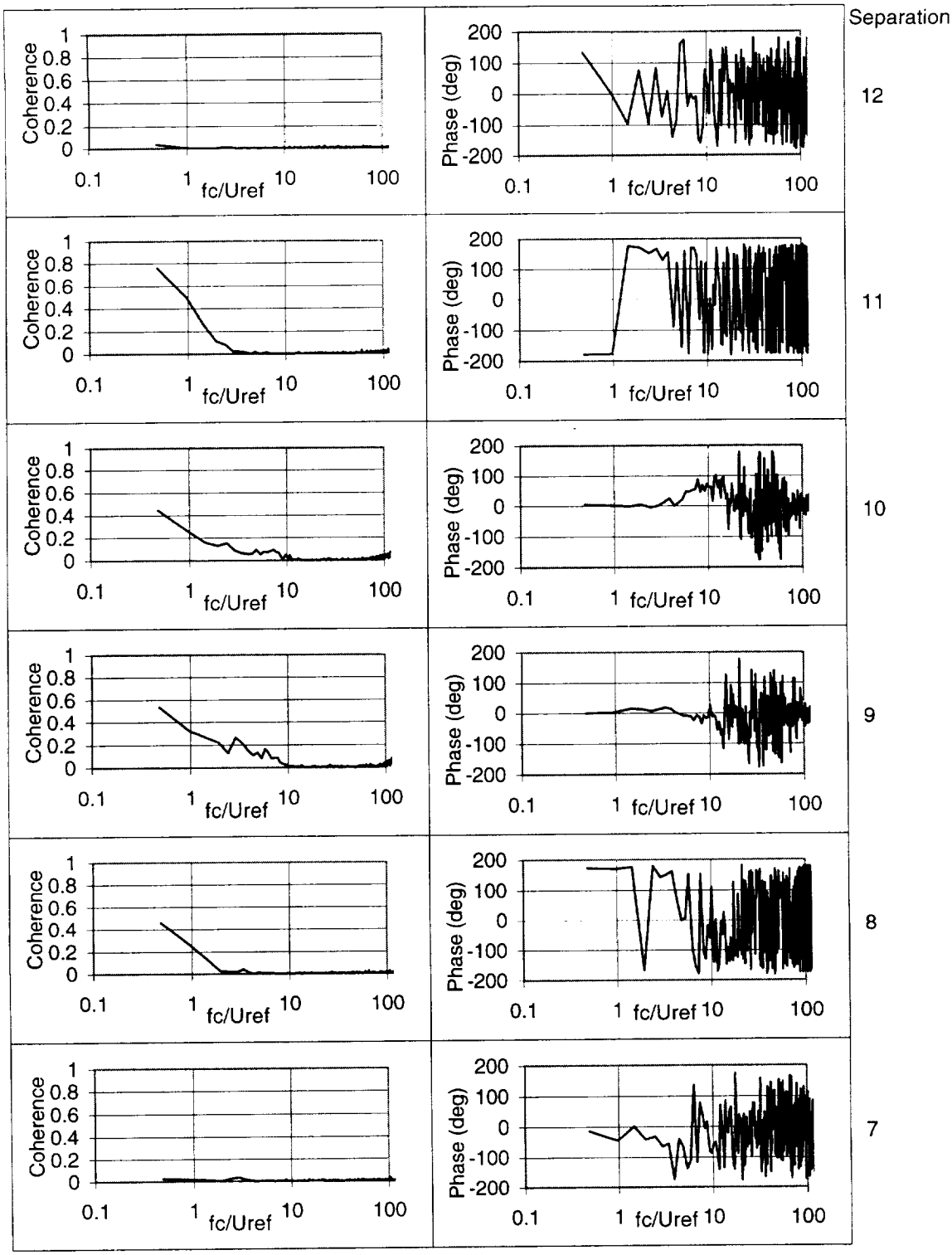

Figure 3.27: Coherence and phase between the upwash (w) velocity component at selected locations along profile T2 and location B (see Figure 3.4)

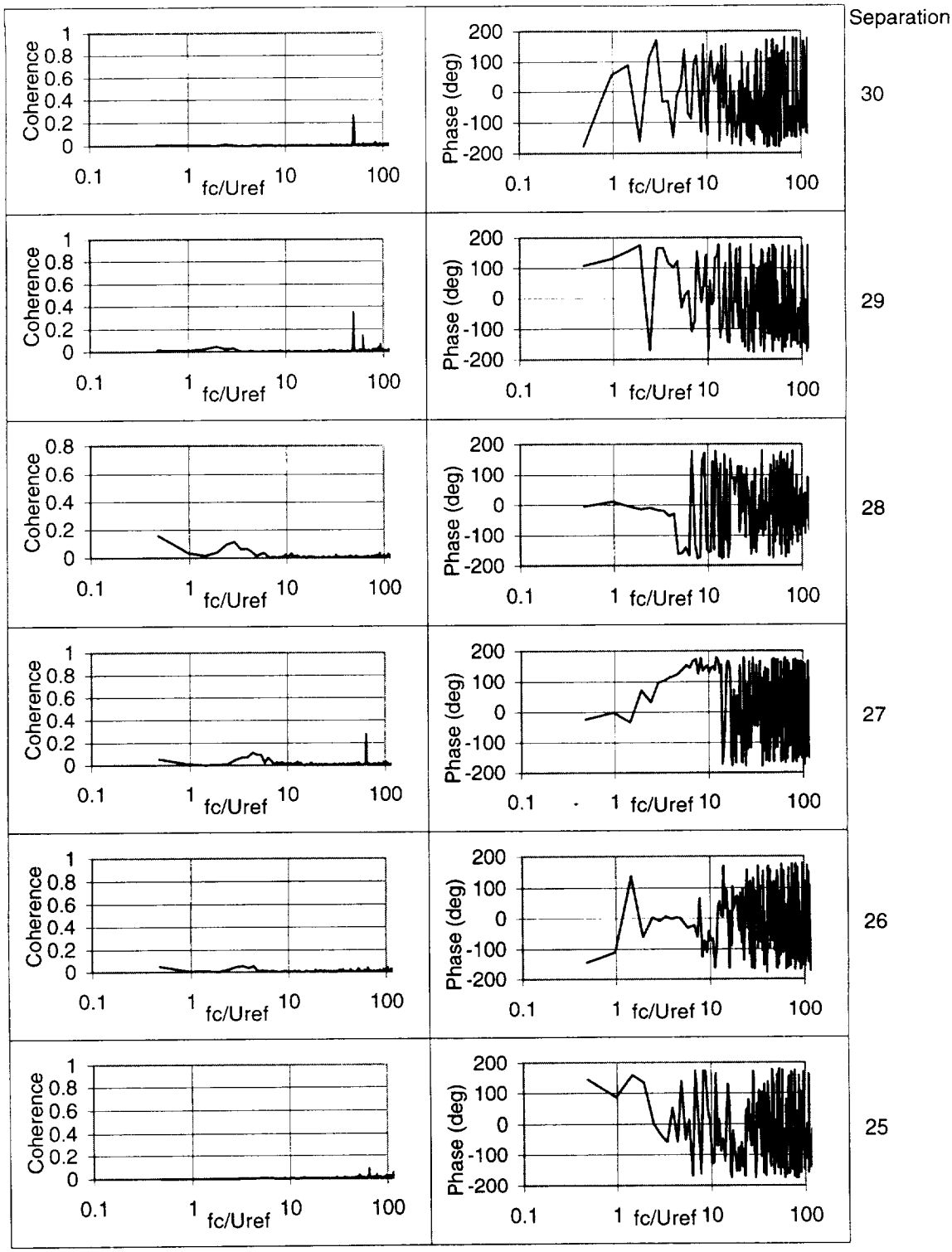

Figure 3.28: Coherence and phase between the axial (u) velocity component between selected locations along profile T5 and location E (see Figure 3.4)

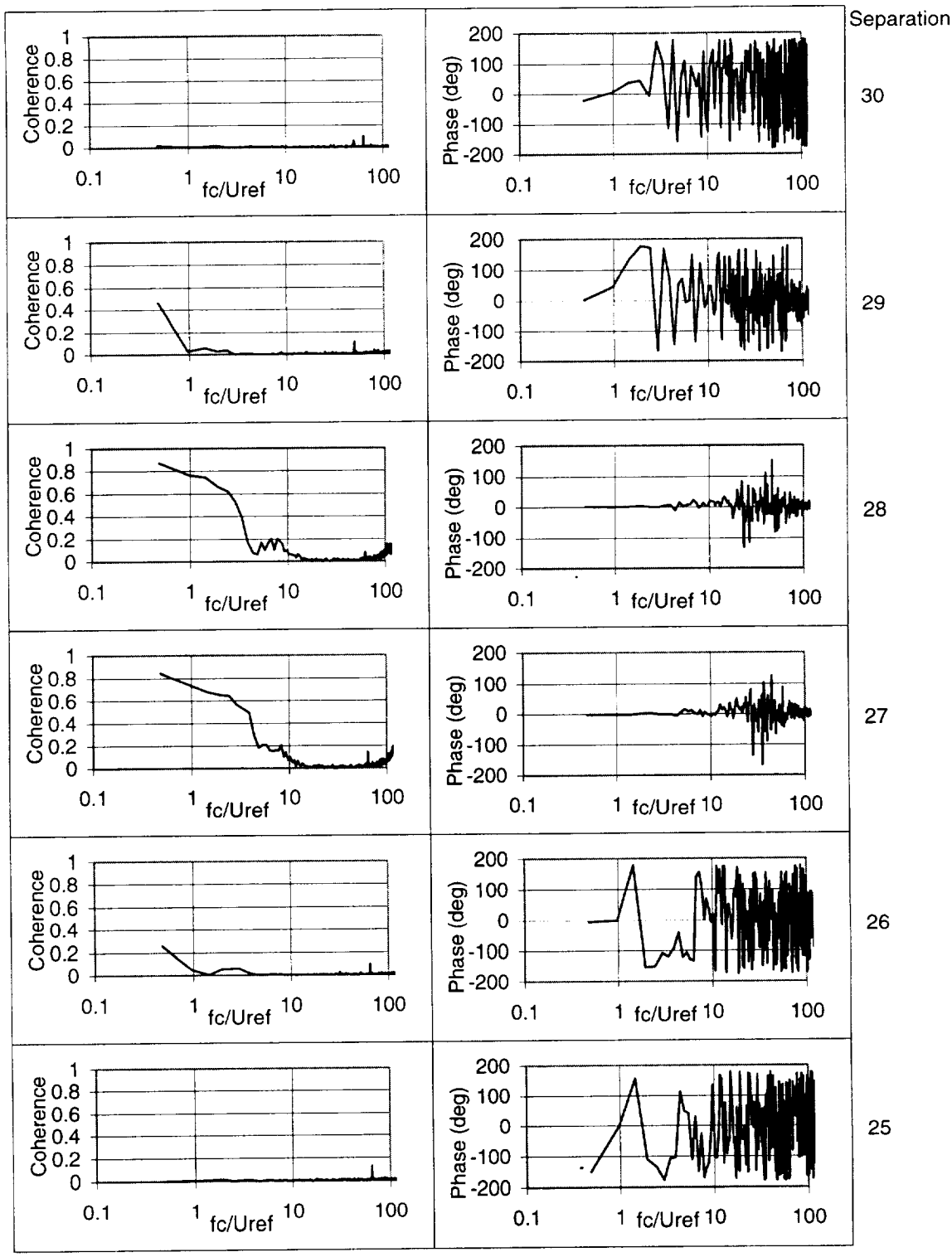

Figure 3.29: Coherence and phase between the spanwise (v) velocity component at selected locations along profile T5 and location E (see Figure 3.4)

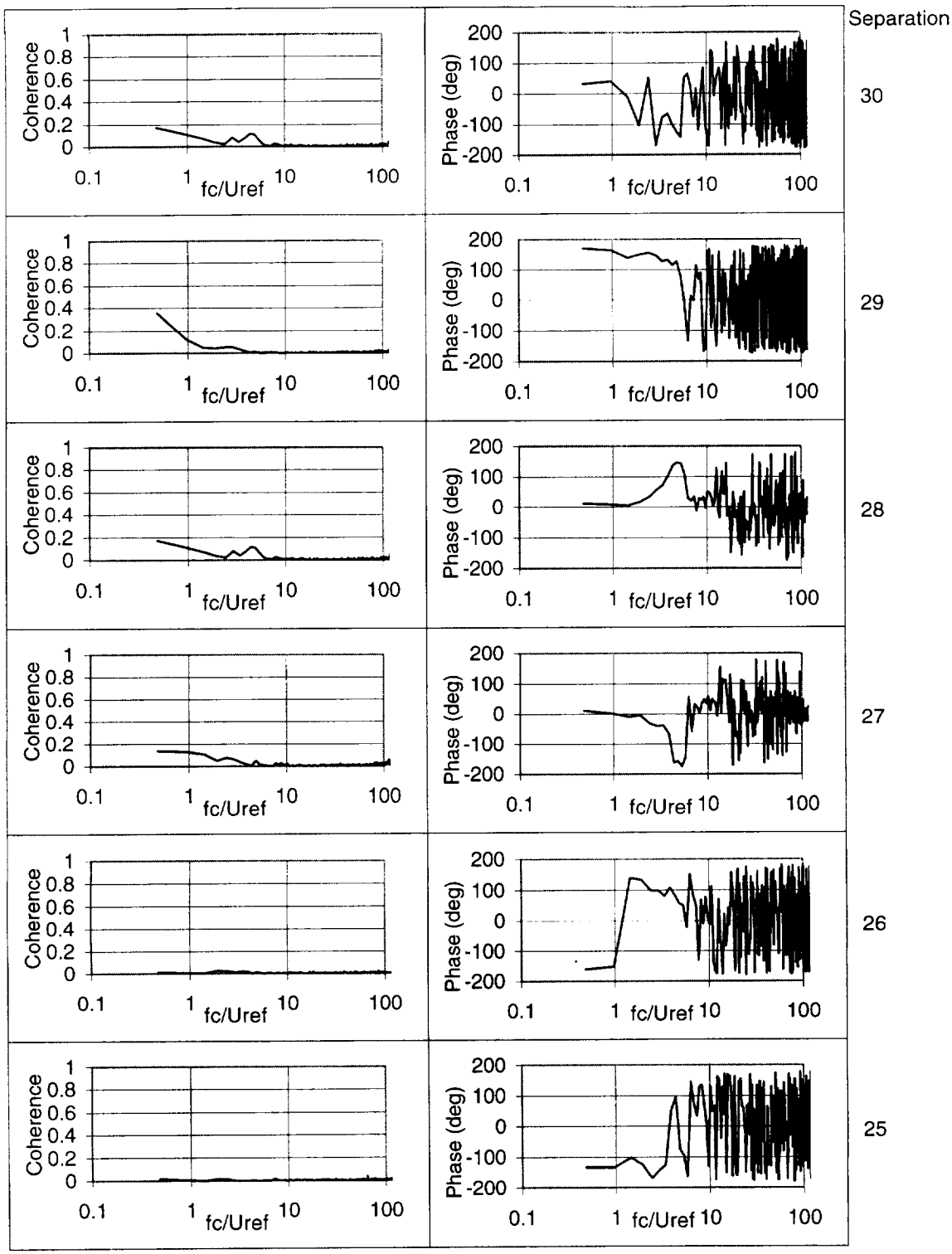

Figure 3.30: Coherence and phase between the upwash (w) velocity component at selected locations along profile T5 and location E (see Figure 3.4)

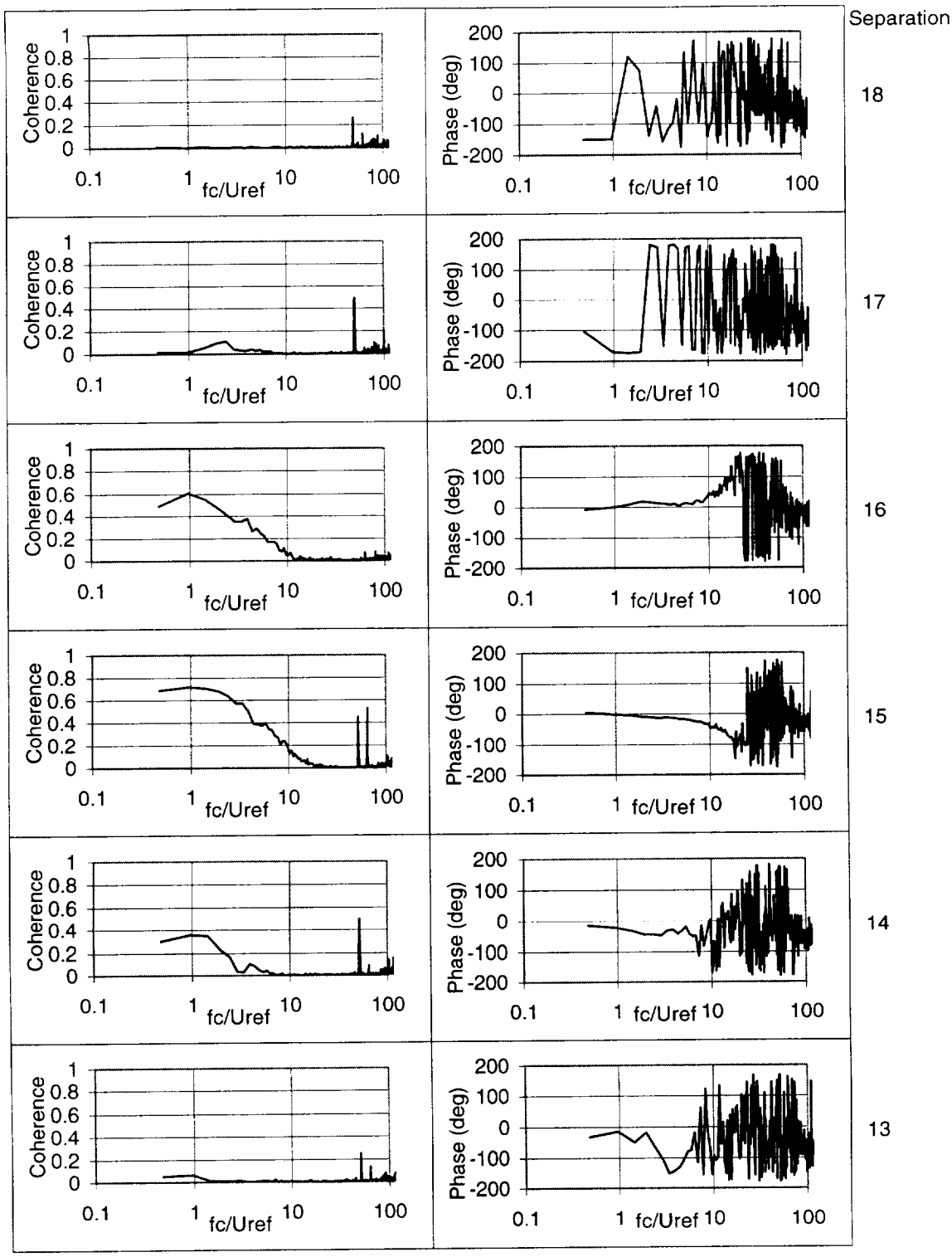

Figure 3.31: Coherence and phase between the axial (u) velocity component between selected locations along profile T3 and location C (see Figure 3.4)

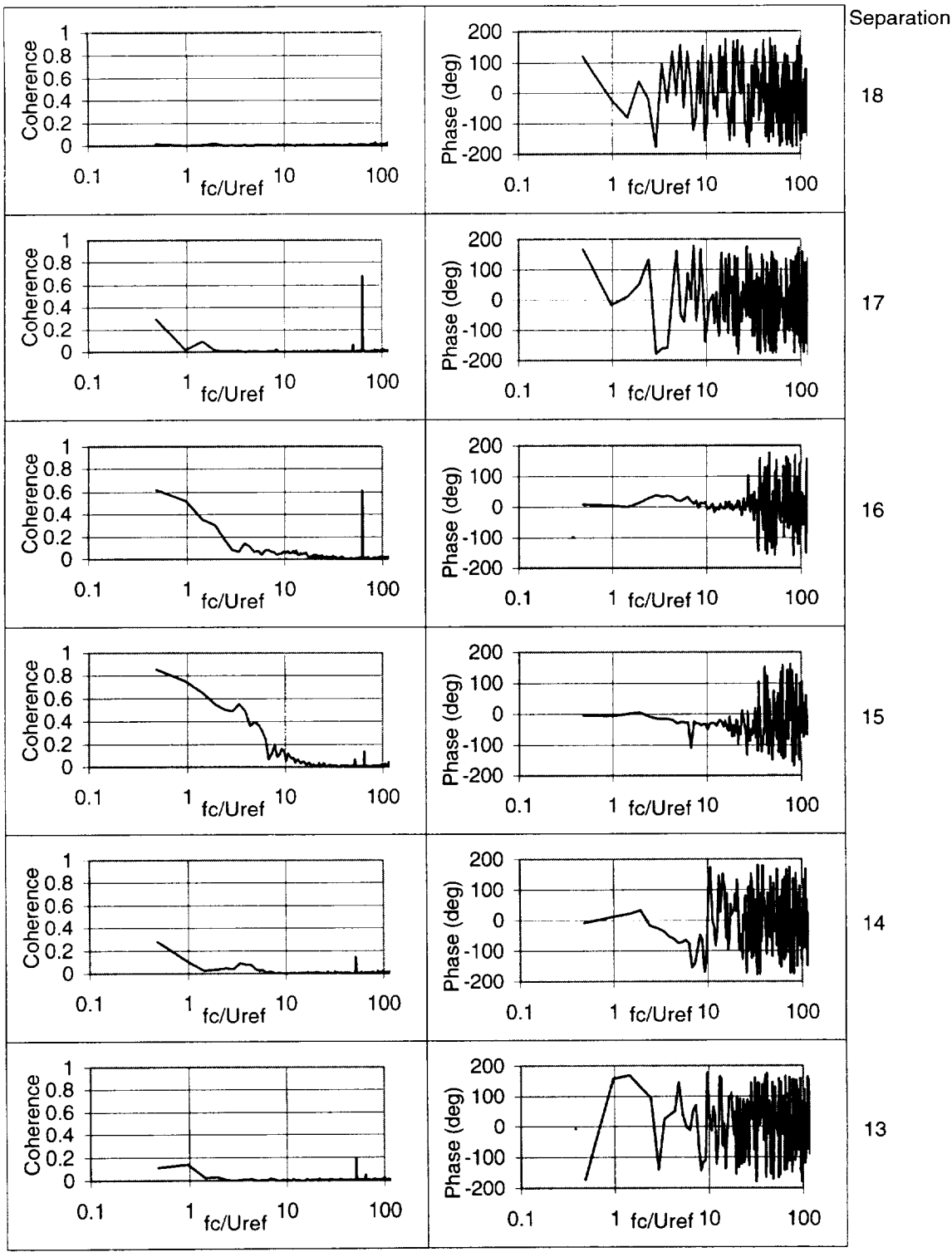

Figure 3.32: Coherence and phase between the spanwise (v) velocity component at selected locations along profile T3 and location C (see Figure 3.4)

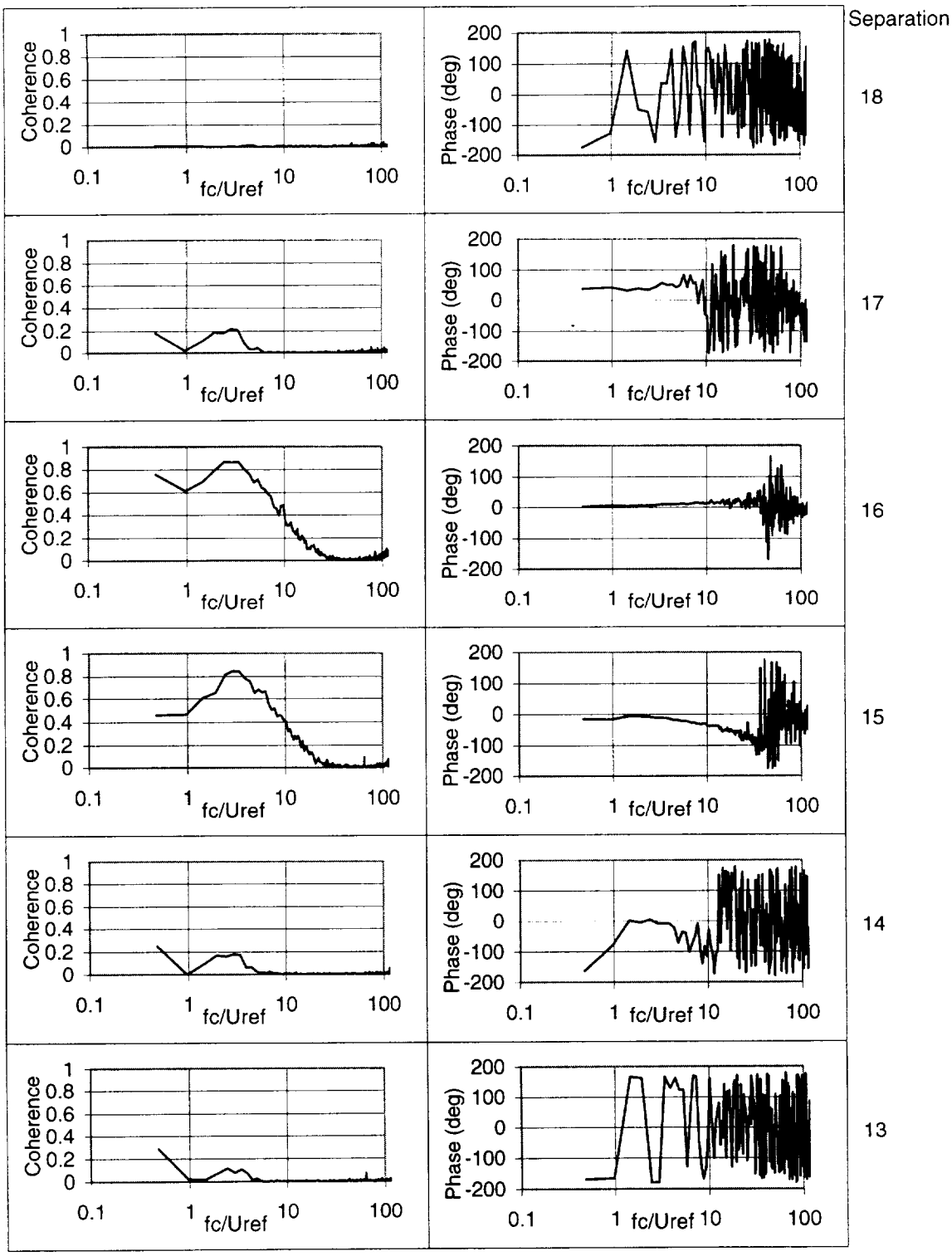

Figure 3.33: Coherence and phase between the upwash (w) velocity component at selected locations along profile T3 and location C (see Figure 3.4)

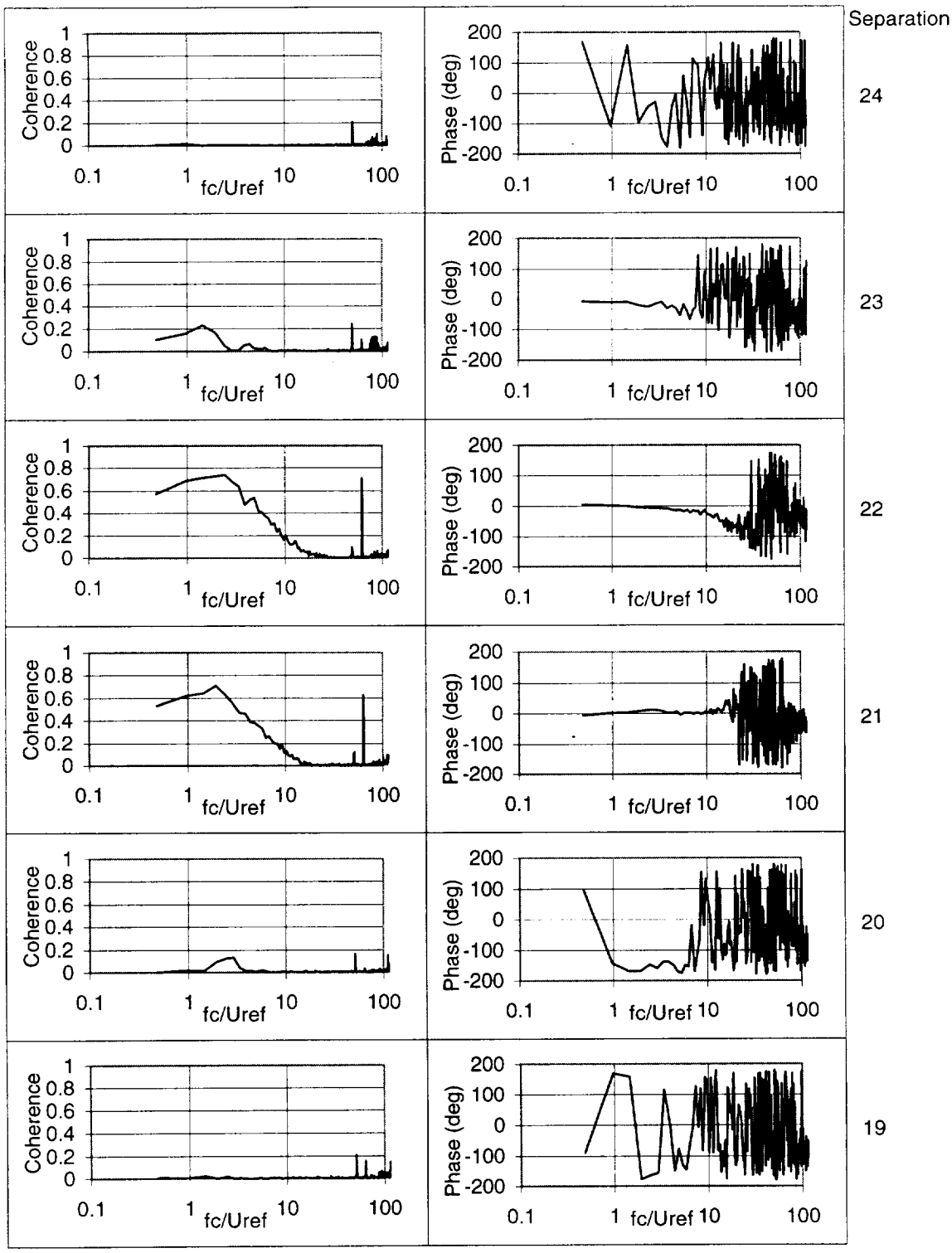

Figure 3.34: Coherence and phase between the axial (u) velocity component between selected locations along profile T4 and location D (see Figure 3.4) .

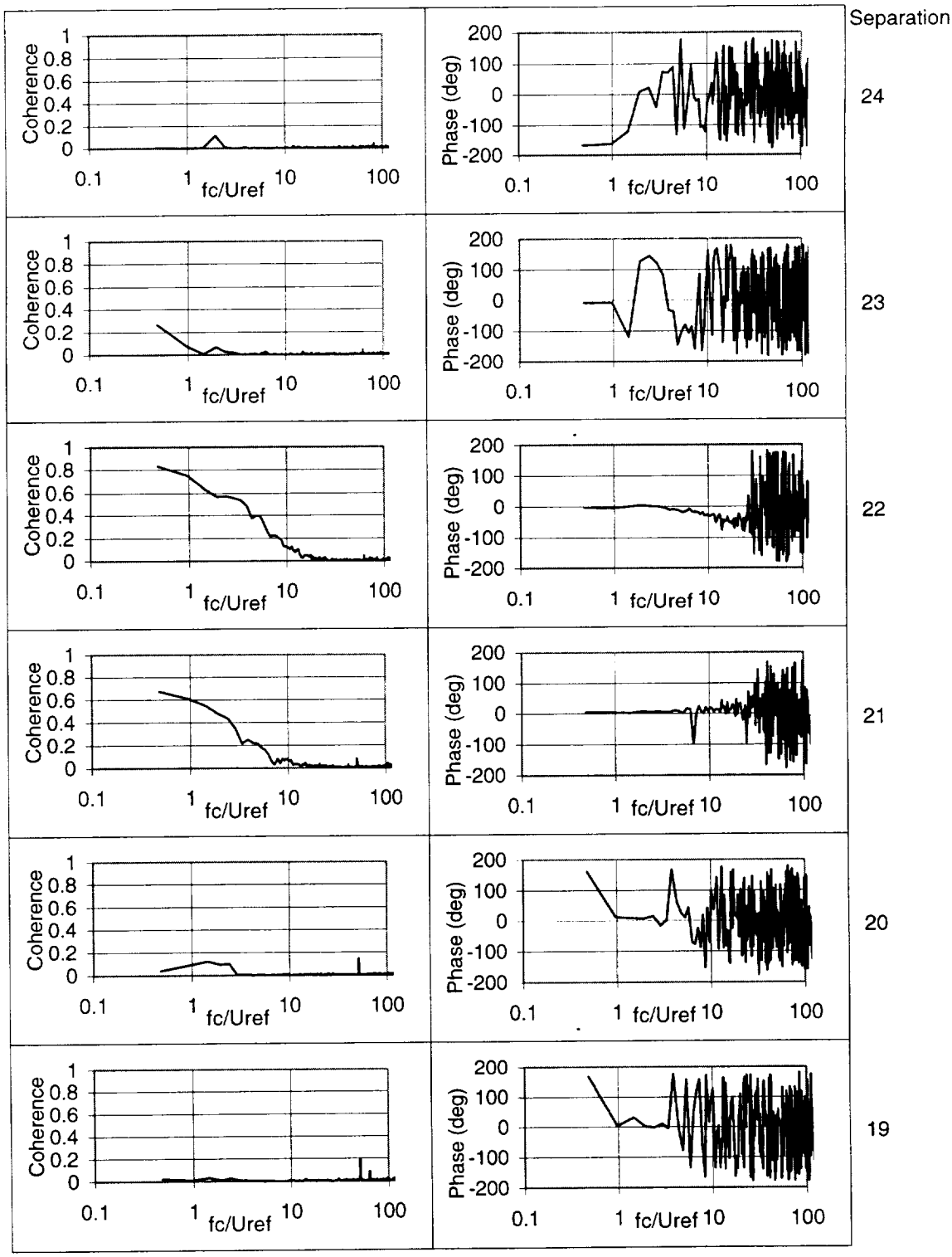

Figure 3.35: Coherence and phase between the spanwise (v) velocity component at selected locations along profile T4 and location D (see Figure 3.4)

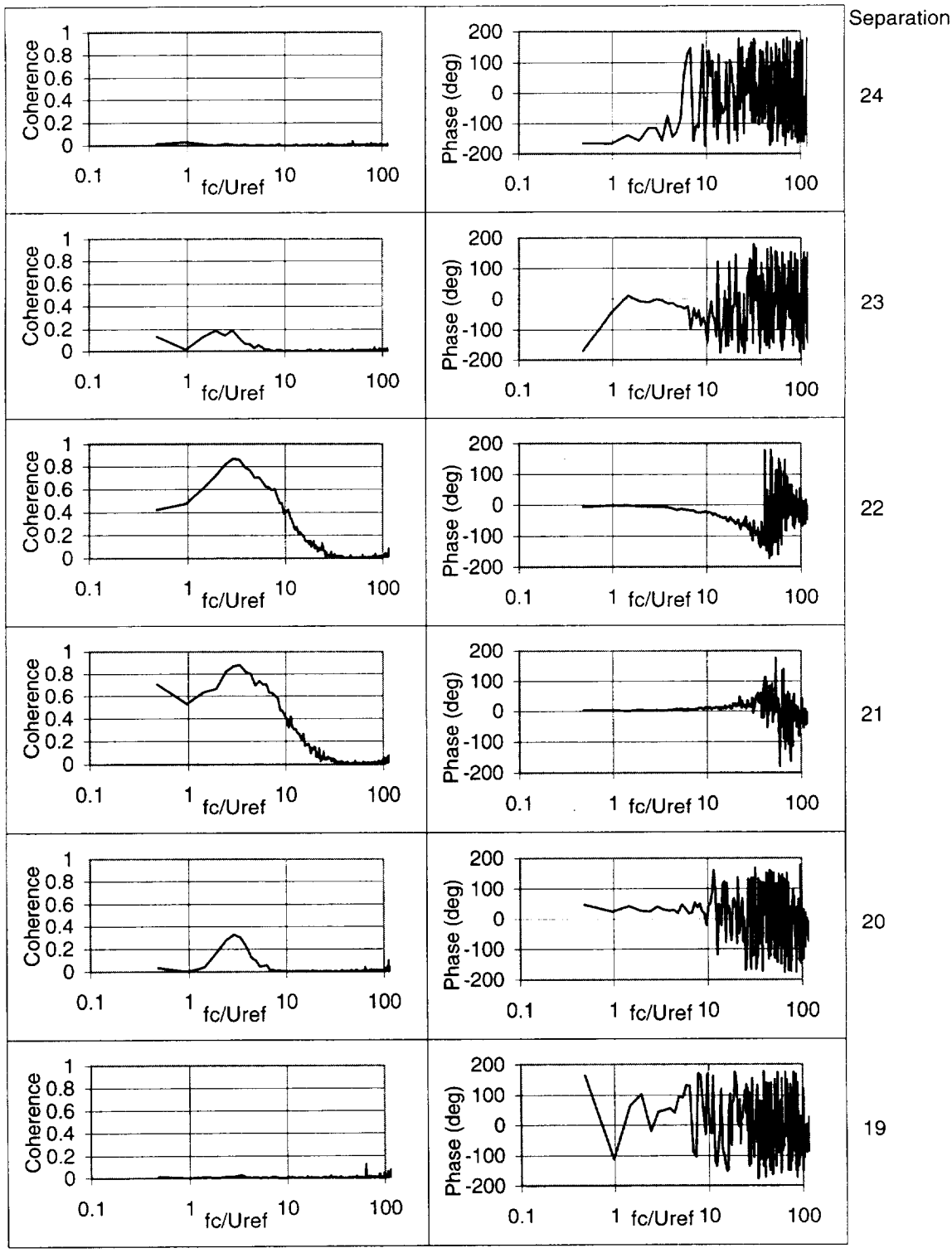

Figure 3.36: Coherence and phase between the upwash (w) velocity component at selected locations along profile T4 and location D (see Figure 3.4)

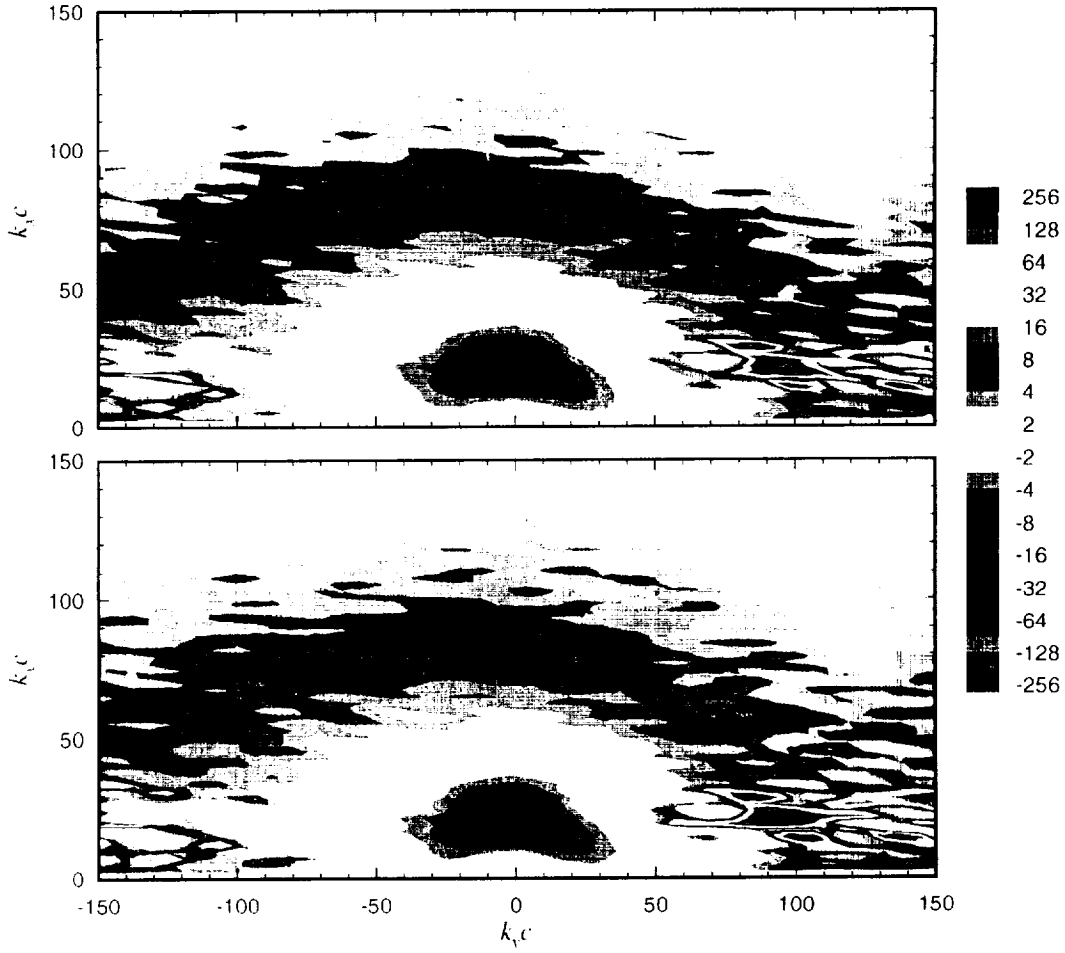

Figure 3.37: Comparison of the wave-number frequency spectrum of the upwash (w) velocity component measured by Miranda and Devenport [25] in the 3-D wake of an airfoil calcaulated with (top) and without (bottom) the use of the Liepman model. Contours are $\phi_{w'w'} U_\infty / (4\pi^2 c^2 \overline{w^2}) \times 10^6$.

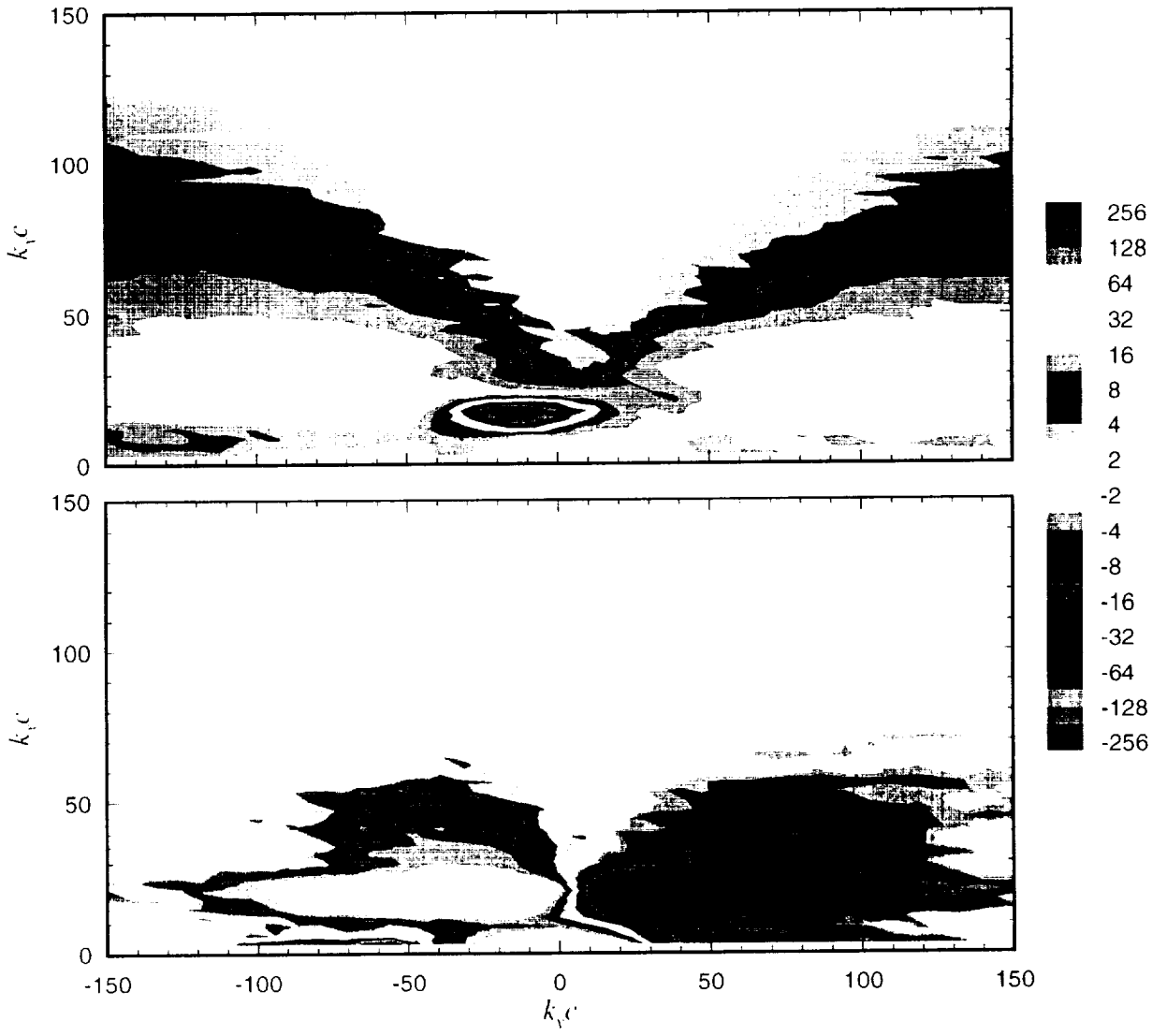

Figure 3.38: Wave number frequency spectrum of the axial (u) velocity component measured along the line T1 about point A shown in Figure 3.4. Contours of the real component of $\phi_{uu} U_\infty / (4\pi^2 c^2 \overline{u^2}) \times 10^6$ are shown at top; imaginary component on bottom.

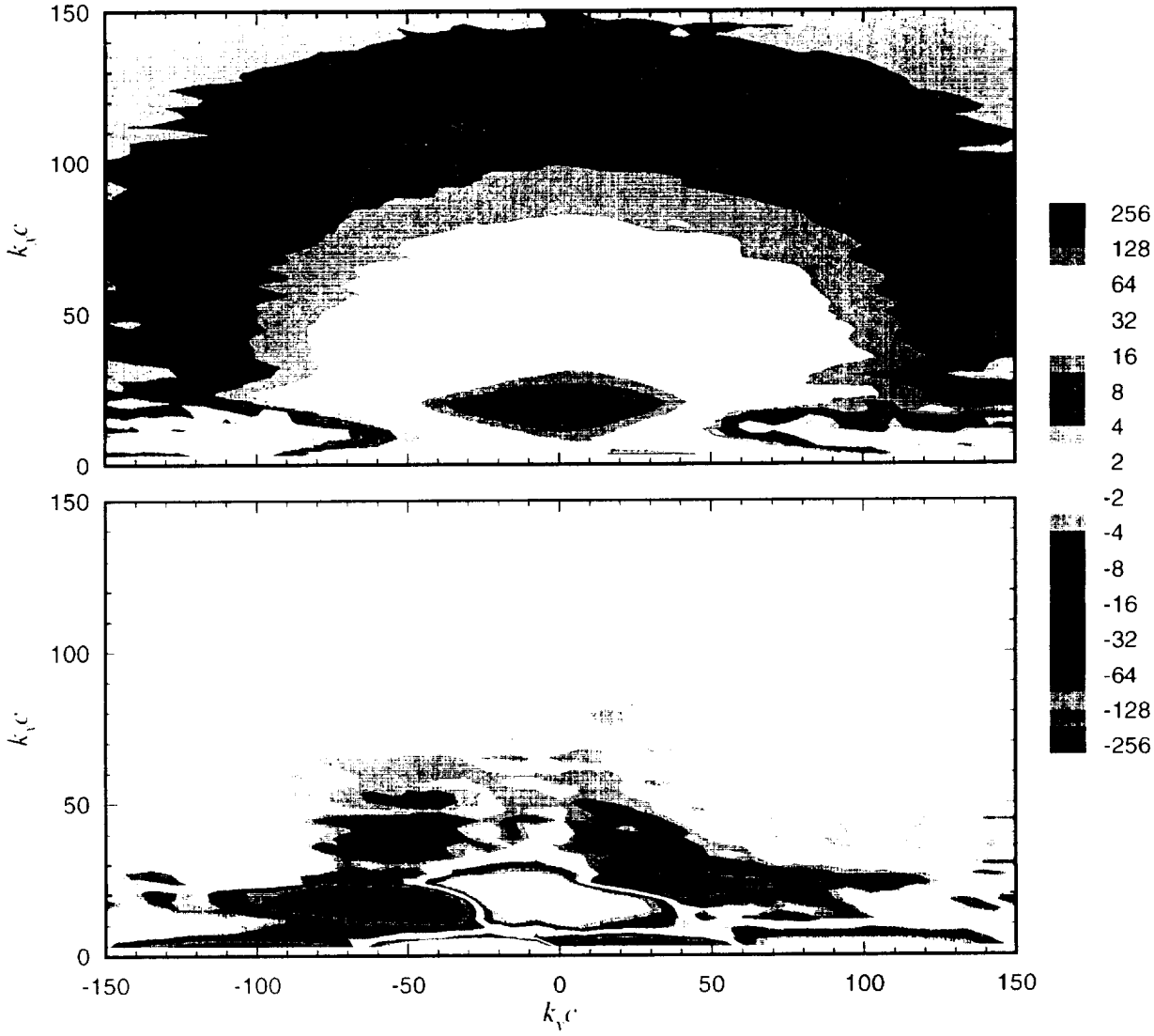

Figure 3.39: Wave number frequency spectrum of the spanwise (v) velocity component measured along the line T1 about point A shown in Figure 3.4. Contours of the real component of $\phi_{vv} U_\infty / (4\pi^2 c^2 \overline{v^2}) \times 10^6$ are shown at top; imaginary component on bottom.

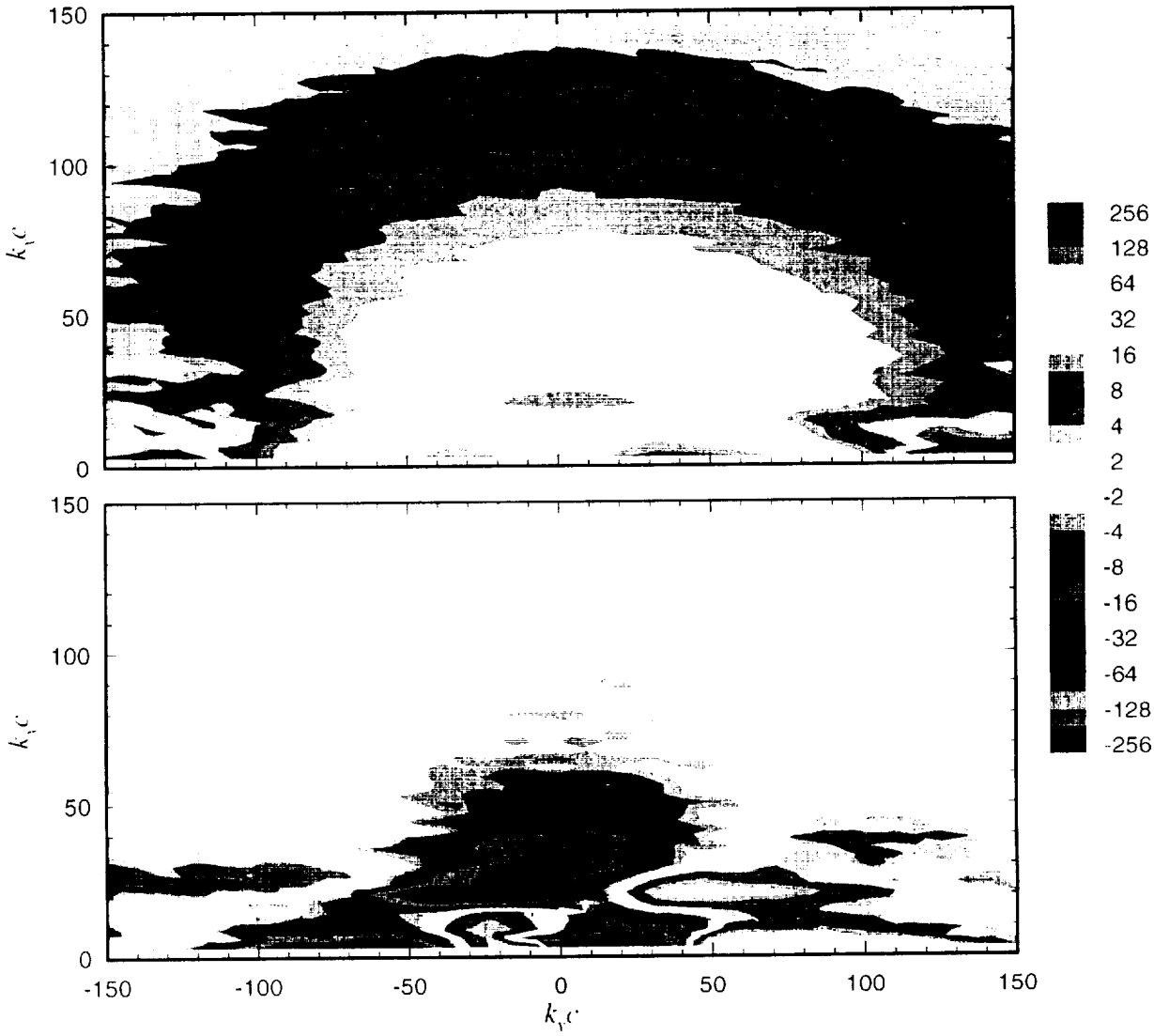

Figure 3.40: Wave number frequency spectrum of the upwash (w) velocity component measured along the line T1 about point A shown in Figure 3.4. Contours of the real component of $\phi_{ww} U_\infty / (4\pi^2 c^2 \overline{w^2}) \times 10^6$ are shown at top; imaginary component on bottom.

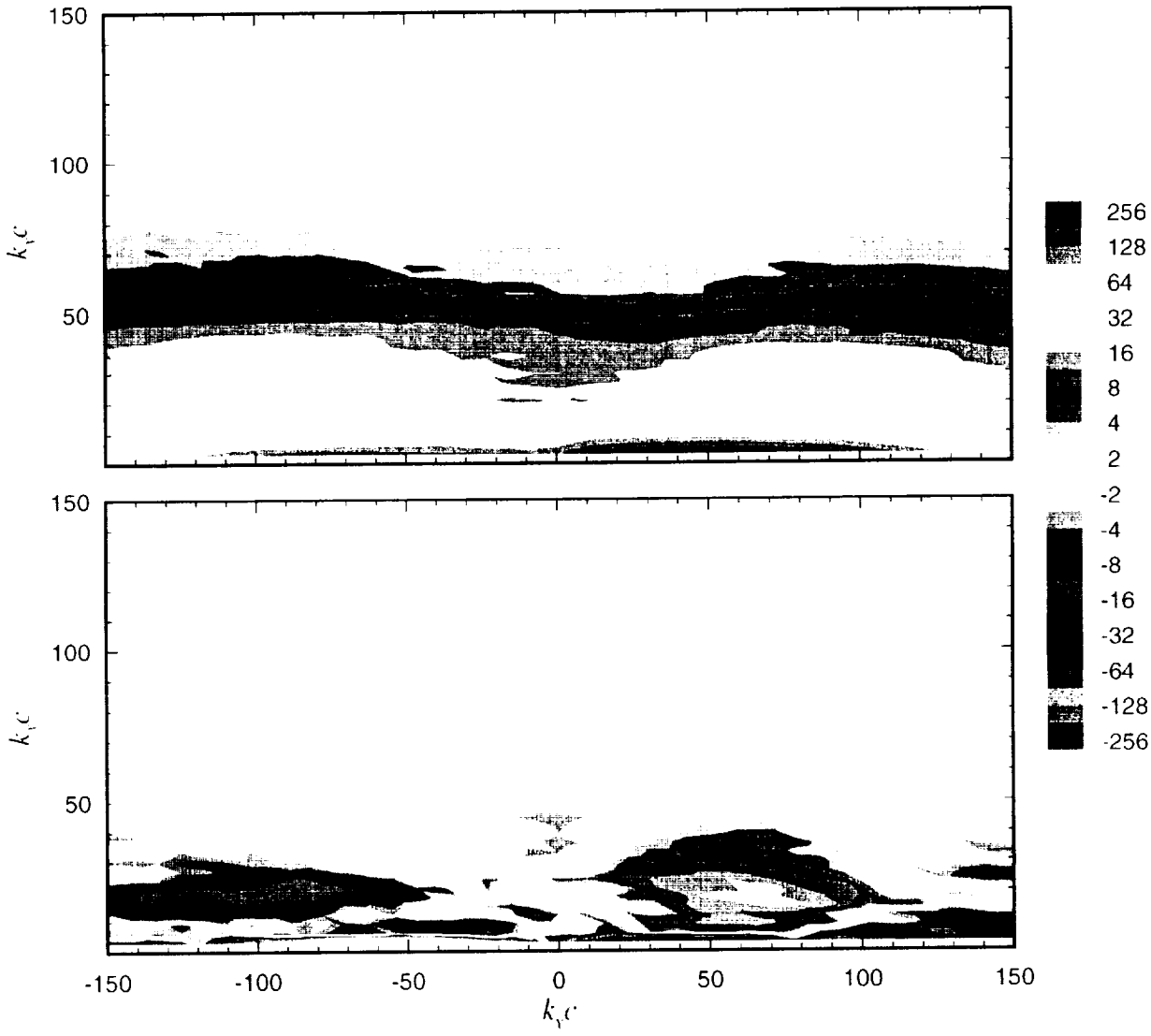

Figure 3.41: Wave-number frequency spectrum of the axial (u) velocity component measured along the line T2 about point B shown in Figure 3.4. Contours of the real component of $\phi_{uu} U_\infty / (4\pi^2 c^2 \overline{u^2}) \times 10^6$ are shown at top; imaginary component on bottom.

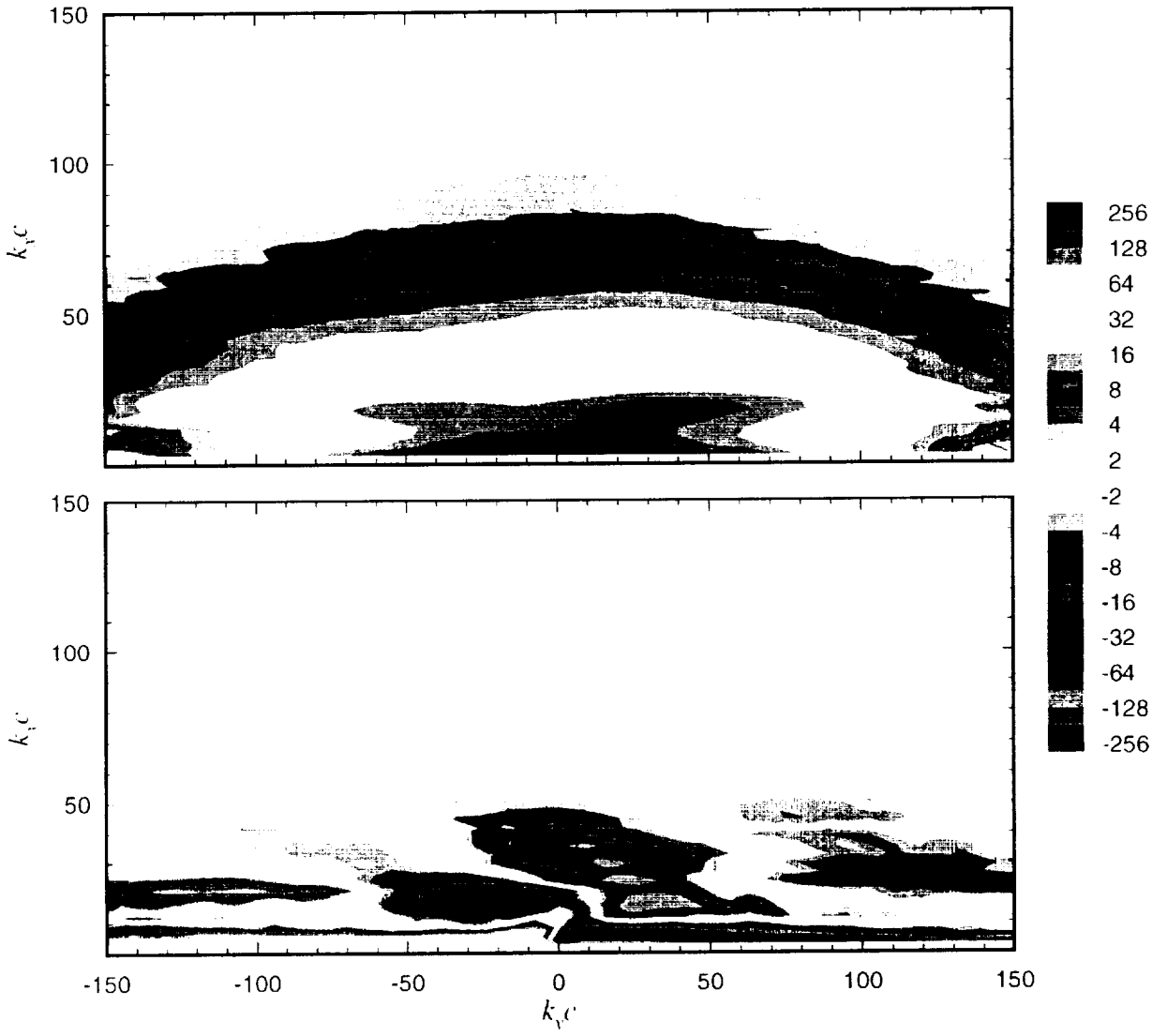

Figure 3.42: Wave-number frequency spectrum of the spanwise (v) velocity component measured along the line T2 about point B shown in Figure 3.4. Contours of the real component of $\phi_{vv} U_\infty / (4\pi^2 c^2 \overline{v^2}) \times 10^6$ are shown at top; imaginary component on bottom.

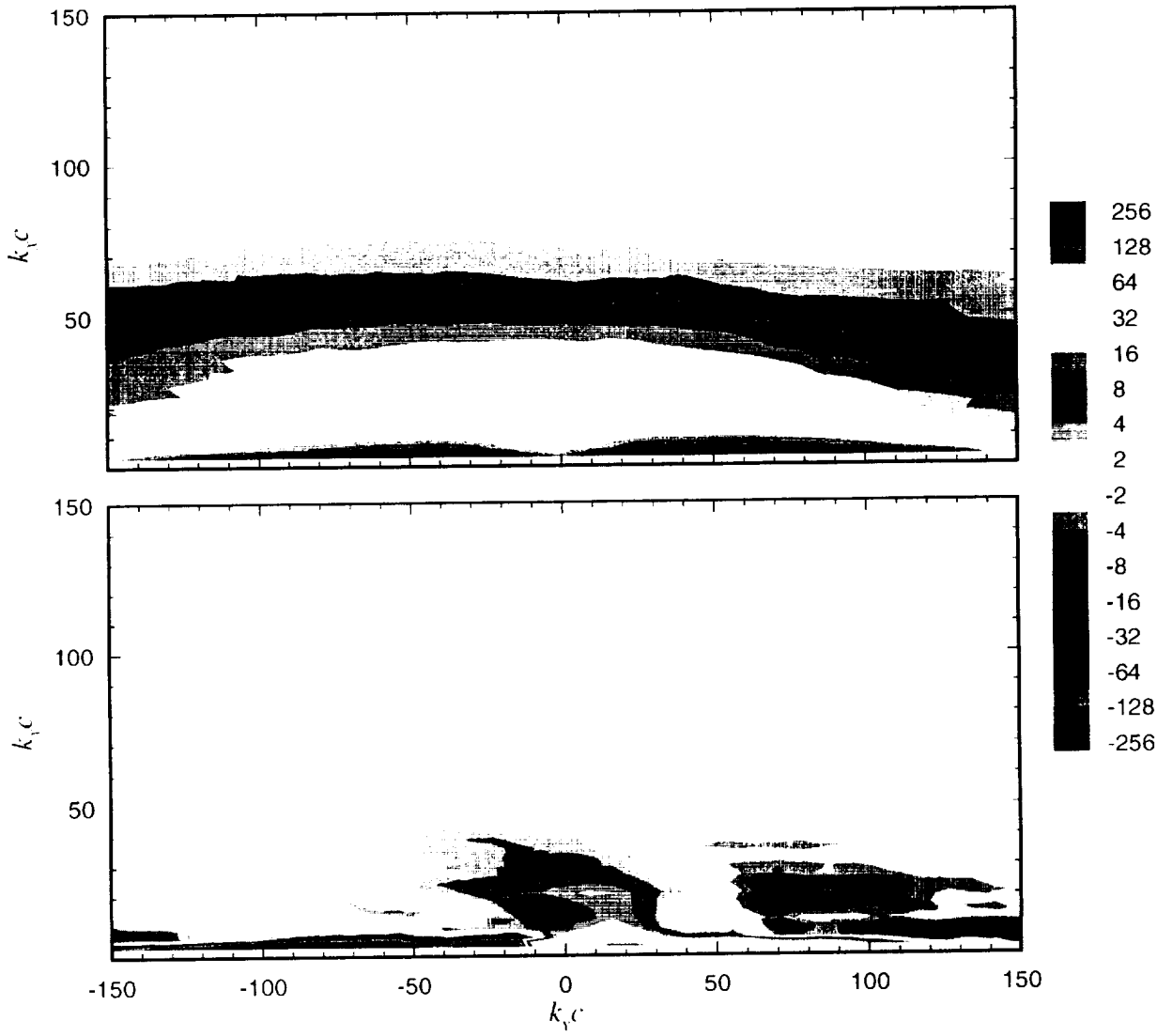

Figure 3.43: Wave-number frequency spectrum of the upwash (w) velocity component measured along the line T2 about point B shown in Figure 3.4. Contours of the real component of $\phi_{ww} U_\infty / (4\pi^2 c^2 \overline{w^2}) \times 10^6$ are shown at top; imaginary component on bottom.

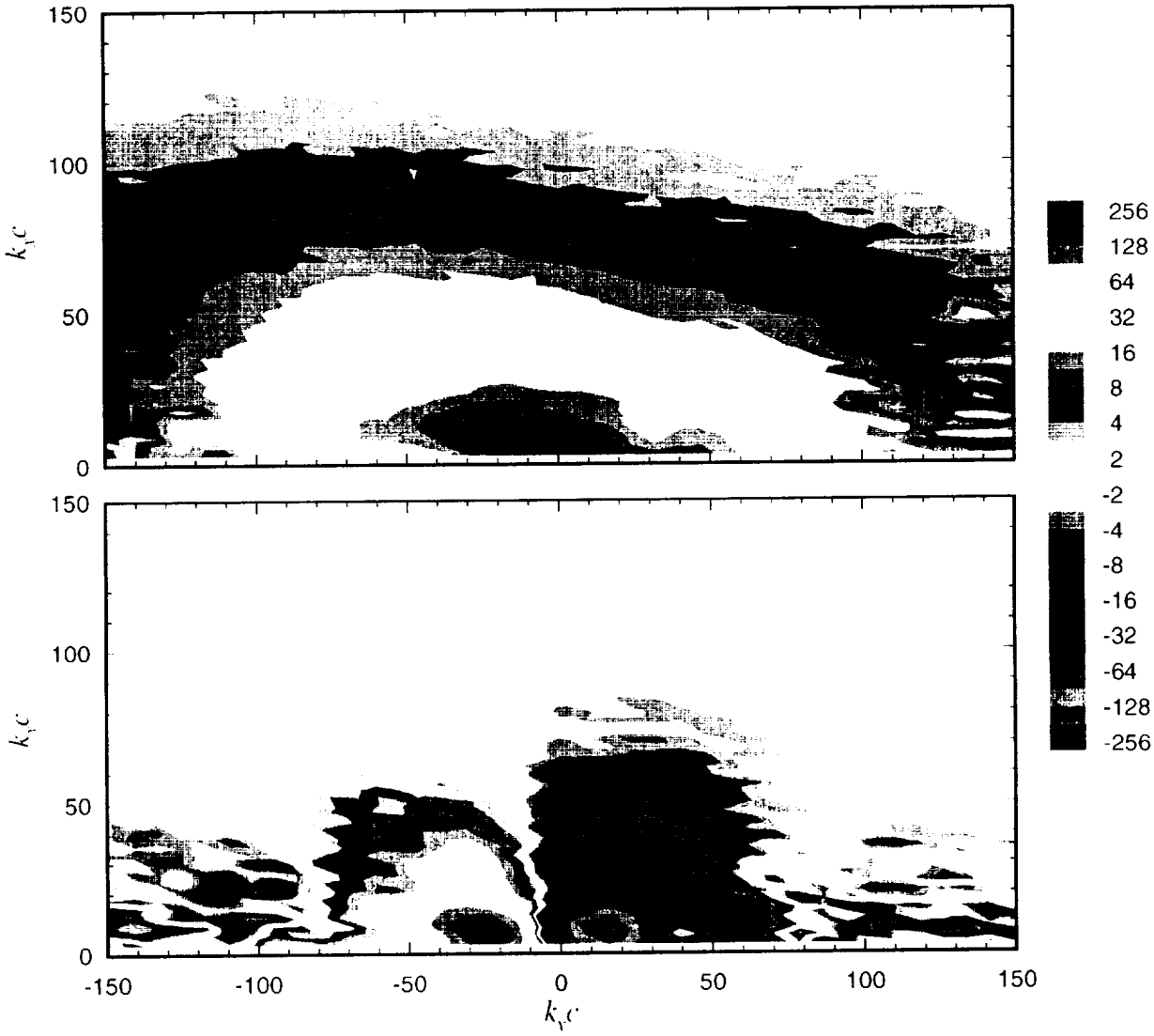

Figure 3.44: Wave-number frequency spectrum of the axial (u) velocity component measured along the line T3 about point C shown in Figure 3.4. Contours of the real component of $\phi_{uu} U_\infty / (4\pi^2 c^2 \overline{u^2}) \times 10^6$ are shown at top; imaginary component on bottom.

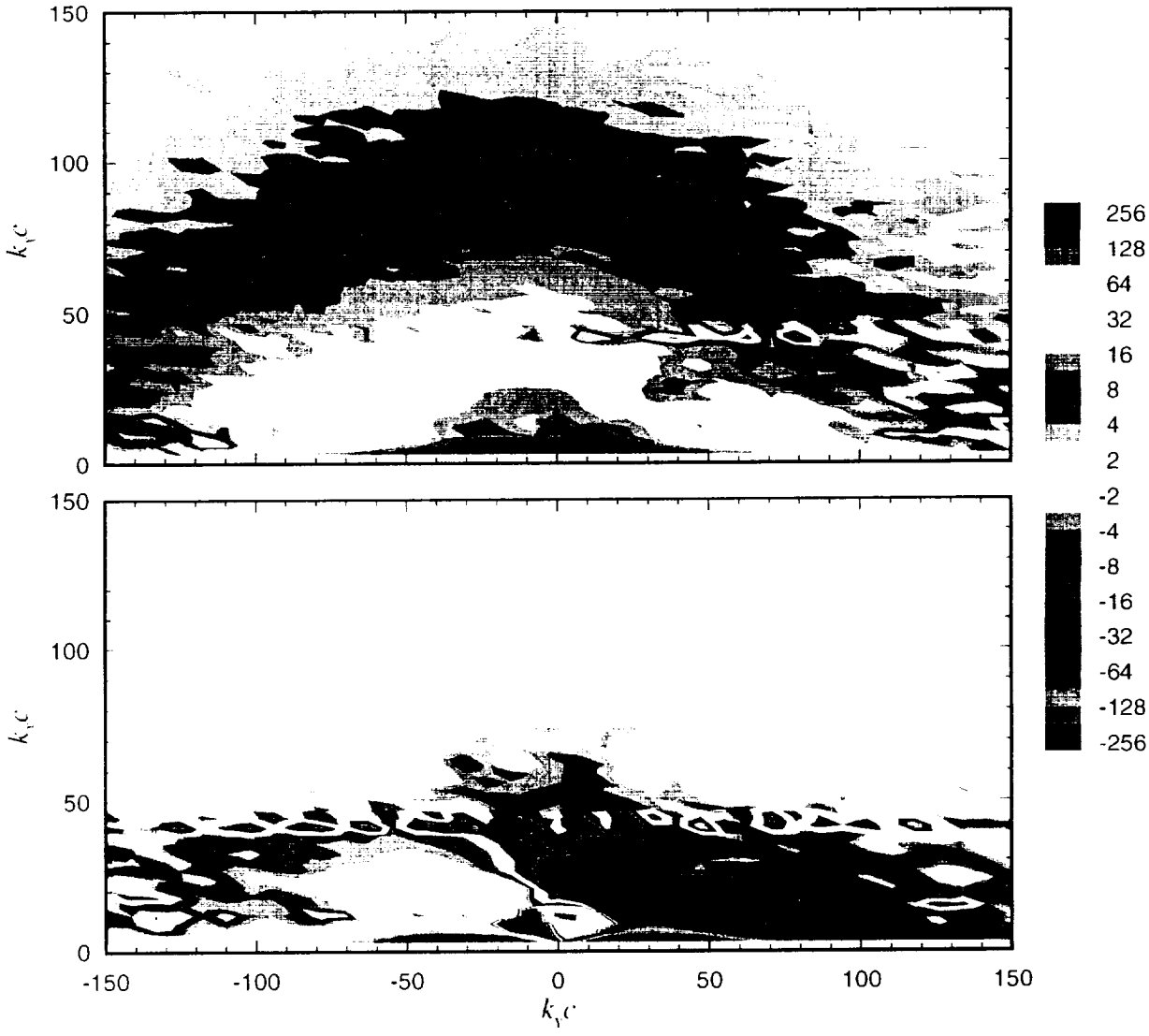

Figure 3.45: Wave-number frequency spectrum of the spanwise (v) velocity component measured along the line T3 about point C shown in Figure 3.4. Contours of the real component of $\phi_{vv} U_\infty / (4\pi^2 c^2 \overline{v^2}) \times 10^6$ are shown at top; imaginary component on bottom.

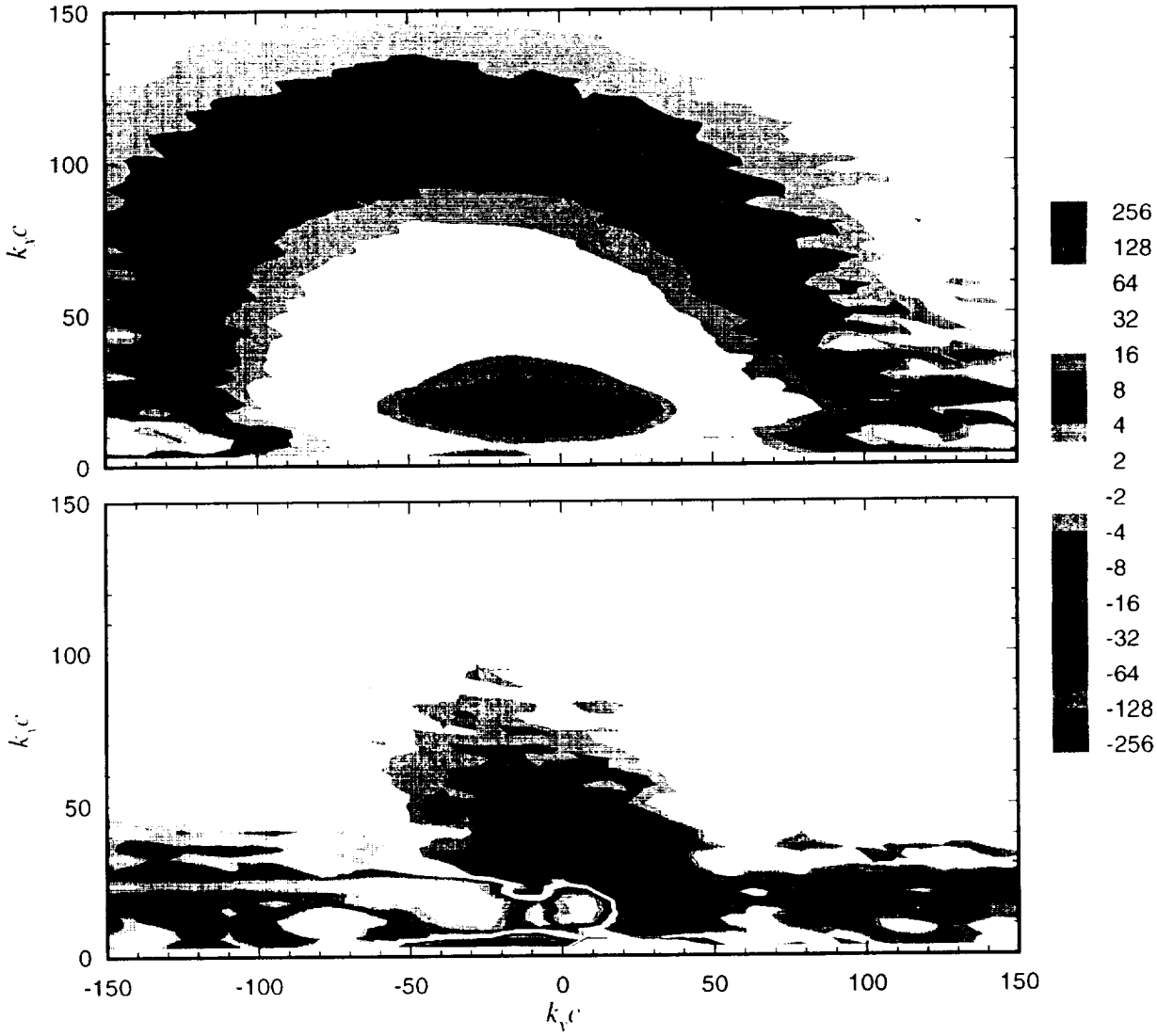

Figure 3.46: Wave-number frequency spectrum of the upwash (w) velocity component measured along the line T3 about point C shown in Figure 3.4. Contours of the real component of $\phi_{ww} U_\infty / (4\pi^2 c^2 \overline{w'^2}) \times 10^6$ are shown at top; imaginary component on bottom.

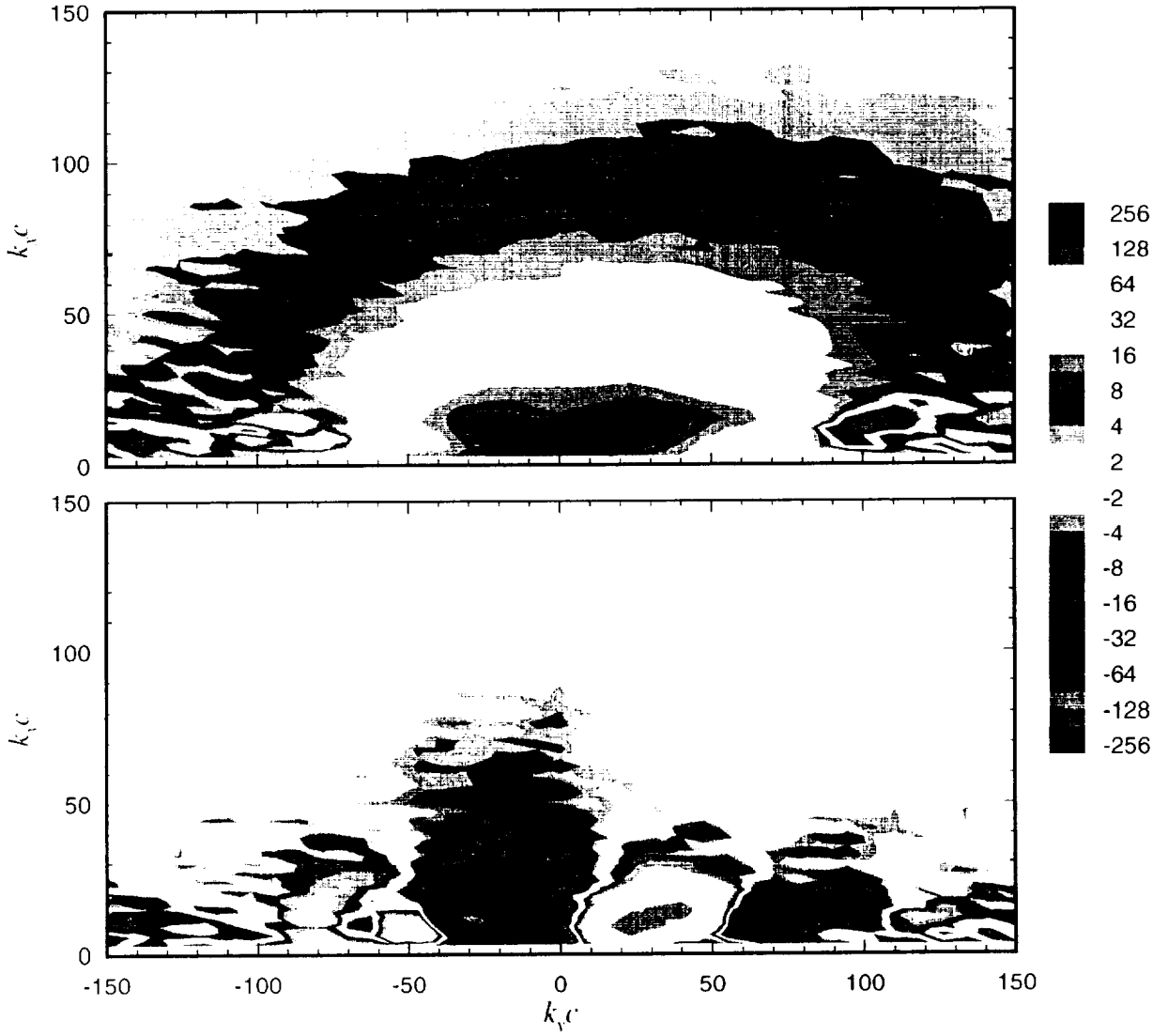

Figure 3.47: Wave-number frequency spectrum of the axial (u) velocity component measured along the line T4 about point D shown in Figure 3.4. Contours of the real component of $\phi_{uu}U_\infty/(4\pi^2c^2\overline{u^2}) \times 10^6$ are shown at top; imaginary component on bottom.

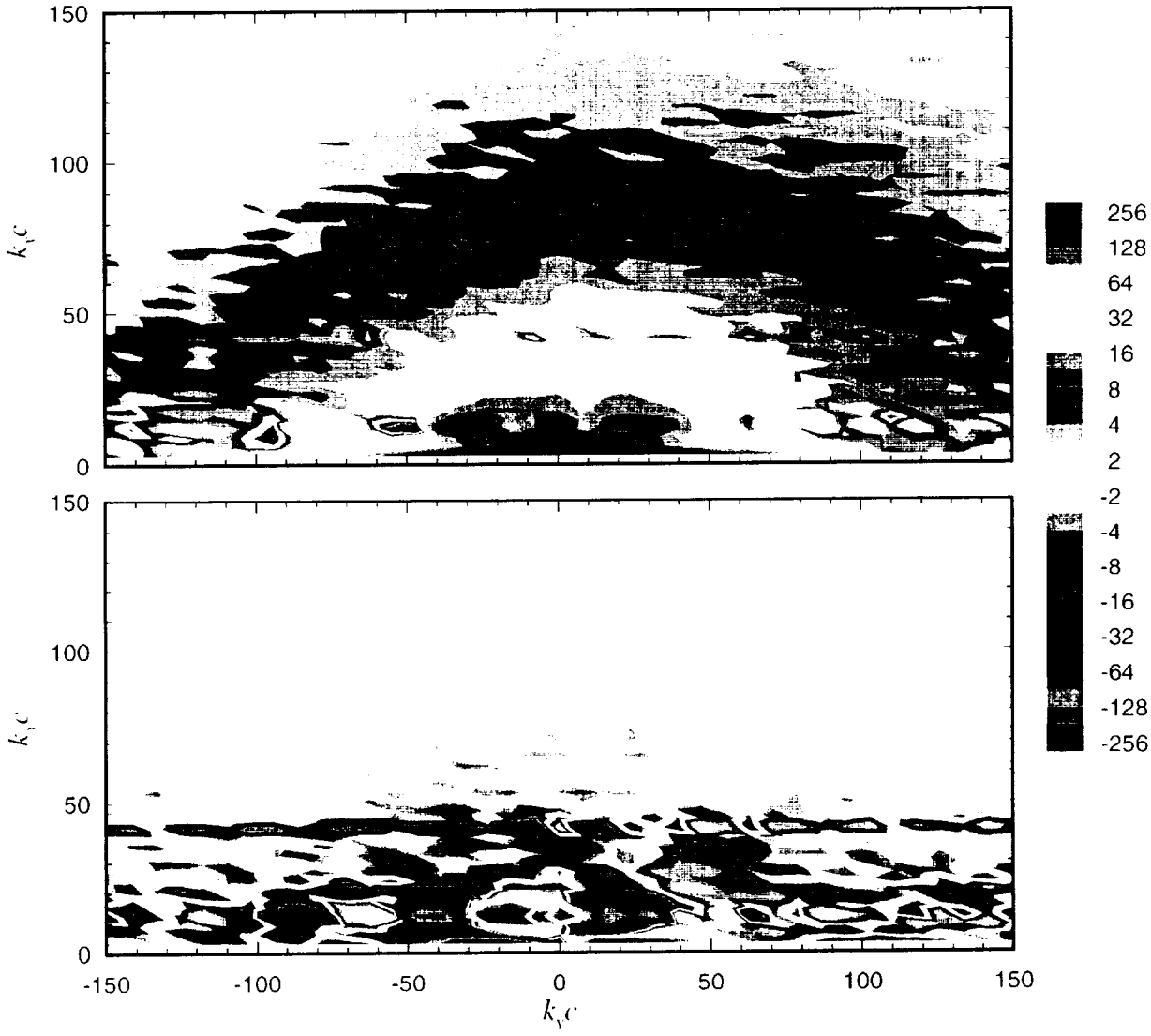

Figure 3.48: Wave-number frequency spectrum of the spanwise (v) velocity component measured along the line T4 about point D shown in Figure 3.4. Contours of the real component of $\phi_{vv} U_\infty / (4\pi^2 c^2 \overline{v^2}) \times 10^6$ are shown at top; imaginary component on bottom.

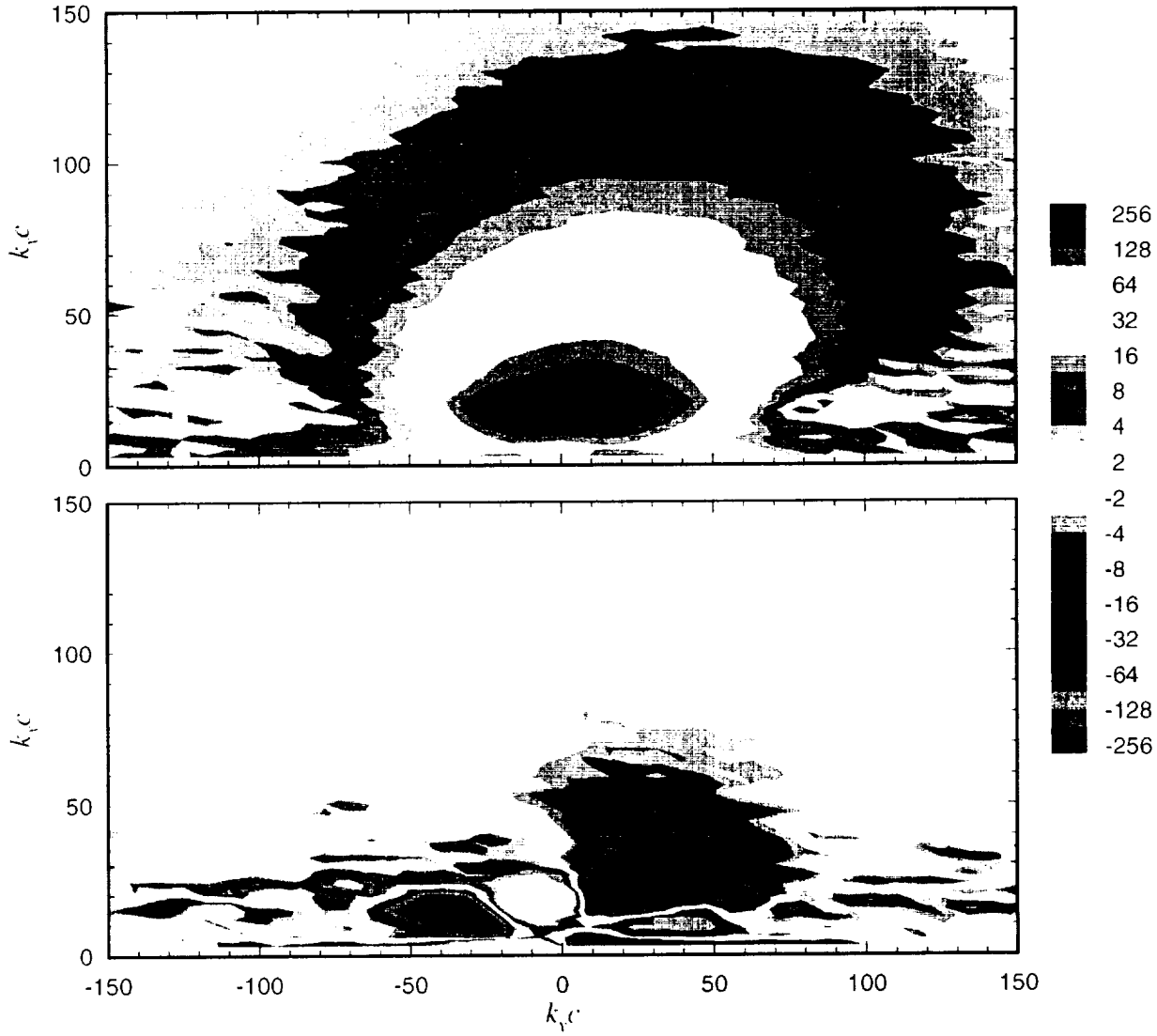

Figure 3.49: Wave-number frequency spectrum of the upwash (w) velocity component measured along the line T4 about point D shown in Figure 3.4. Contours of the real component of $\phi_{ww} U_\infty / (4\pi^2 c^2 \overline{w^2}) \times 10^6$ are shown at top; imaginary component on bottom.

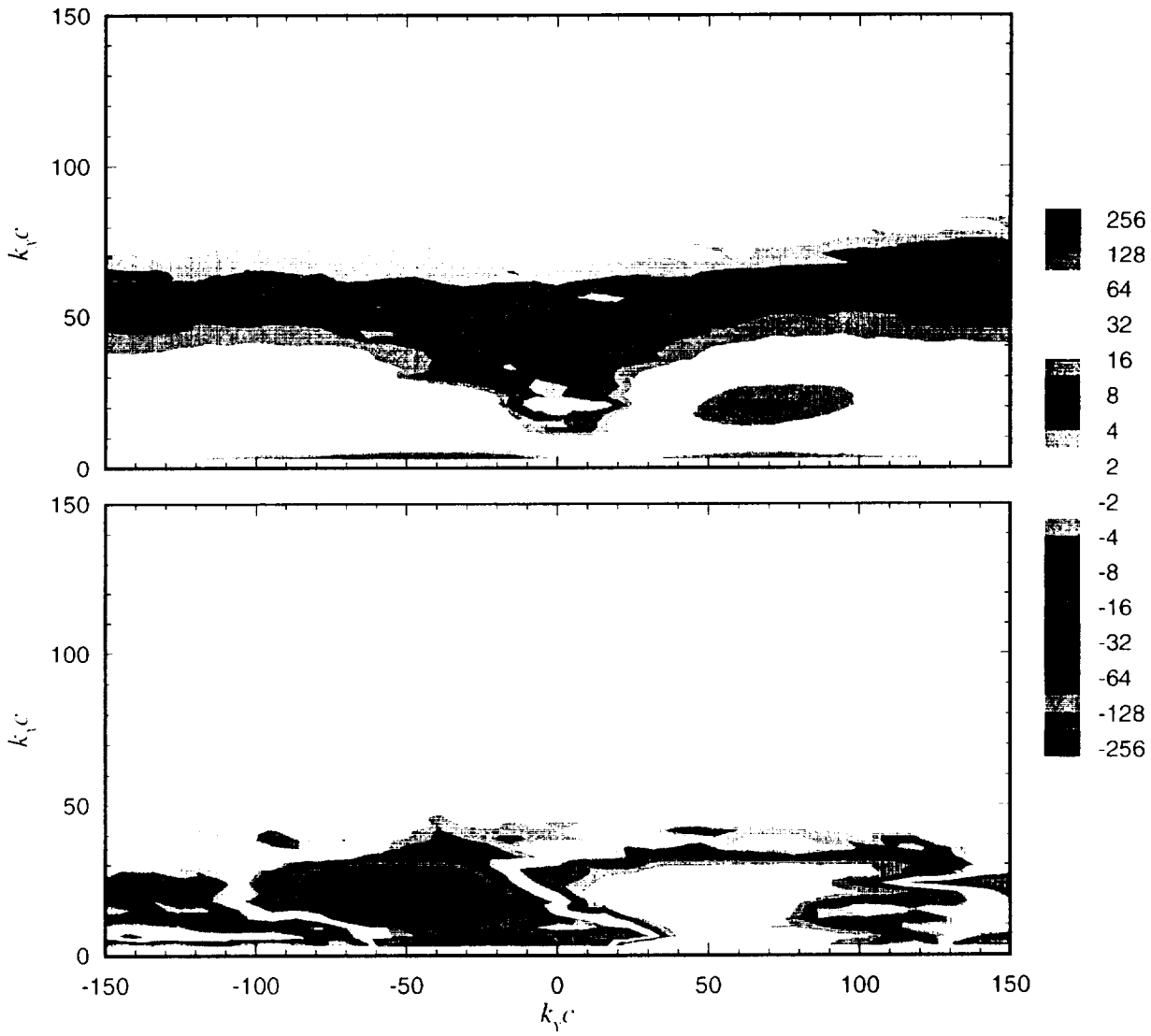

Figure 3.50: Wave-number frequency spectrum of the axial (u) velocity component measured along the line T5 about point E shown in Figure 3.4. Contours of the real component of $\phi_{uu}U_\infty/(4\pi^2c^2\overline{u^2}) \times 10^6$ are shown at top; imaginary component on bottom.

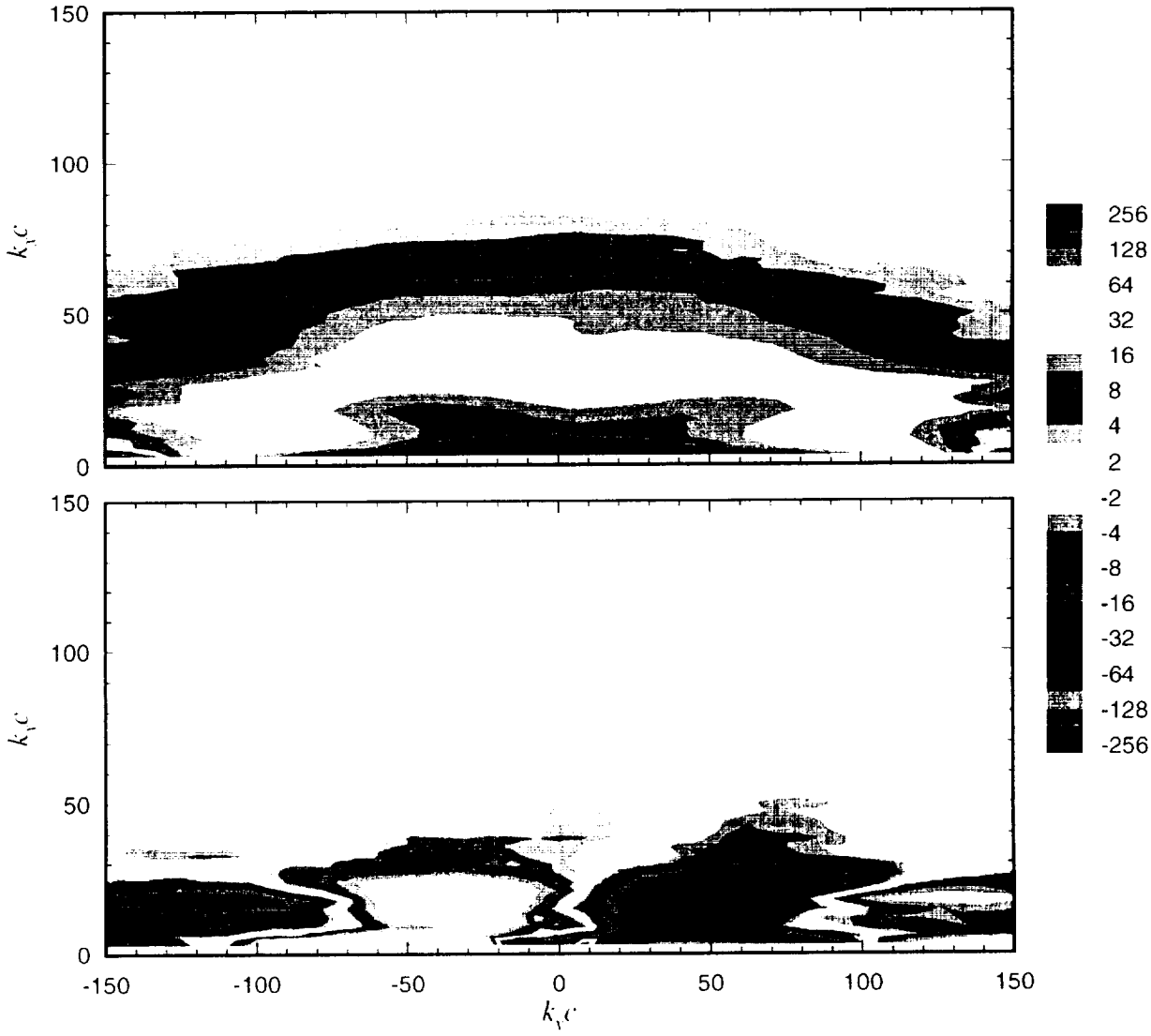

Figure 3.51: Wave-number frequency spectrum of the spanwise (v) velocity component measured along the line T5 about point E shown in Figure 3.4. Contours of the real component of $\phi_{vv} U_\infty / (4\pi^2 c^2 \overline{v^2}) \times 10^6$ are shown at top; imaginary component on bottom.

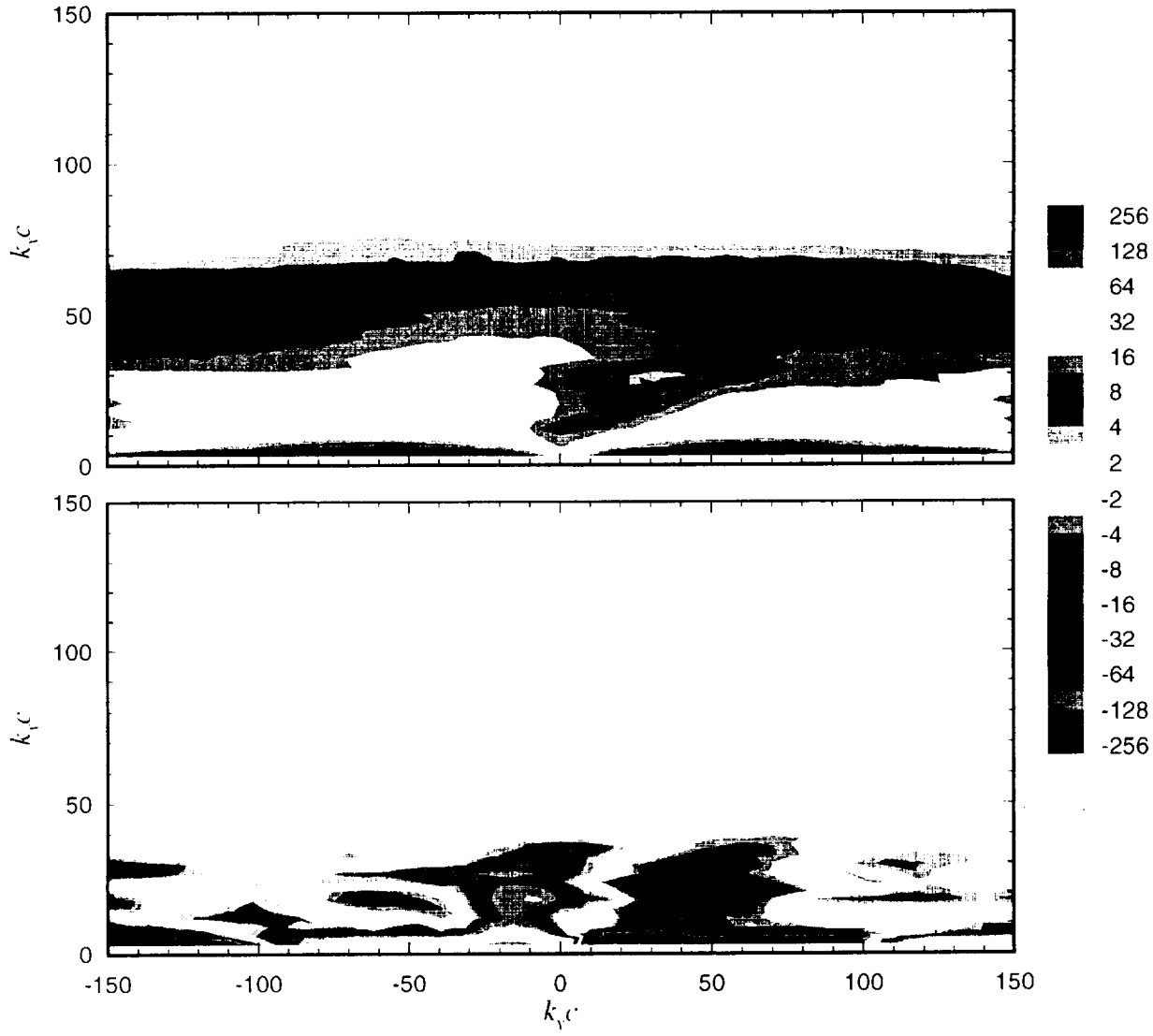

Figure 3.52: Wave-number frequency spectrum of the upwash (w) velocity component measured along the line T5 about point E shown in Figure 3.4. Contours of the real component of $\phi_{ww} U_\infty / (4\pi^2 c^2 \overline{w^2}) \times 10^6$ are shown at top; imaginary component on bottom.

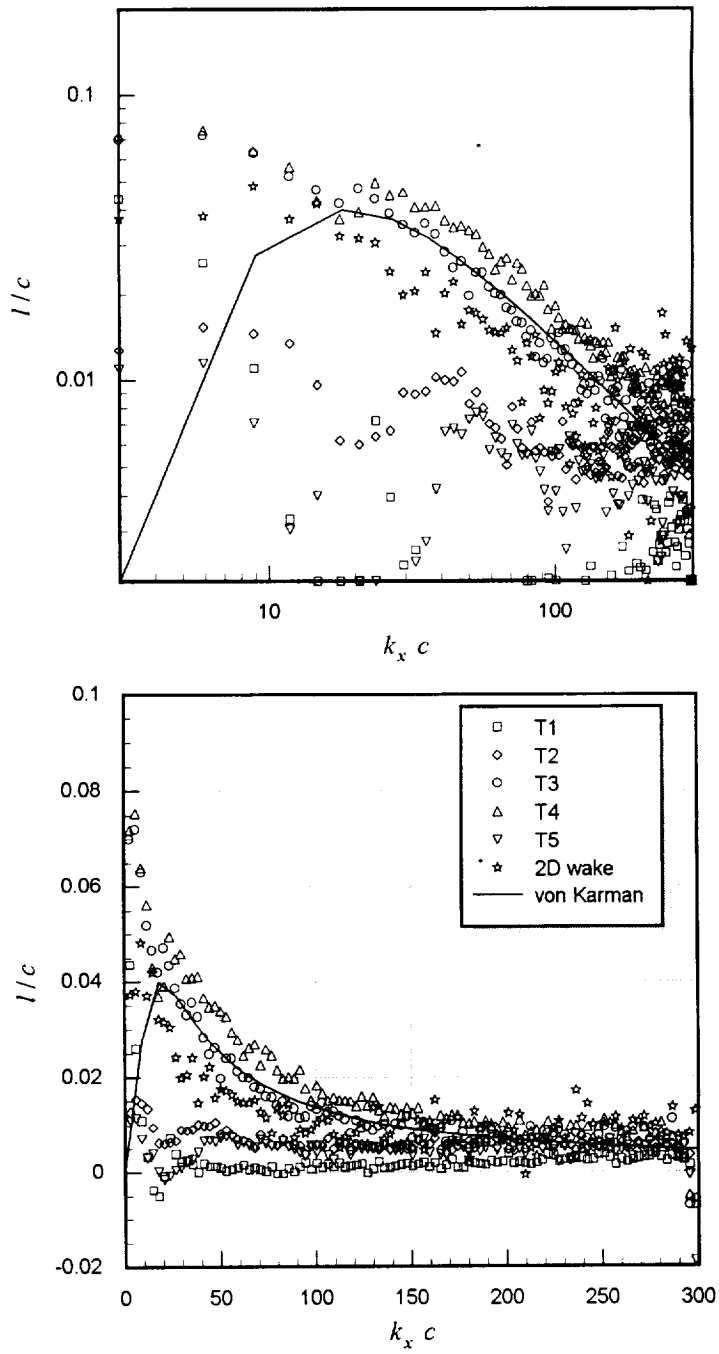

Figure 3.53: Spanwise length scale (l) of the axial (u) velocity component as a function of frequency

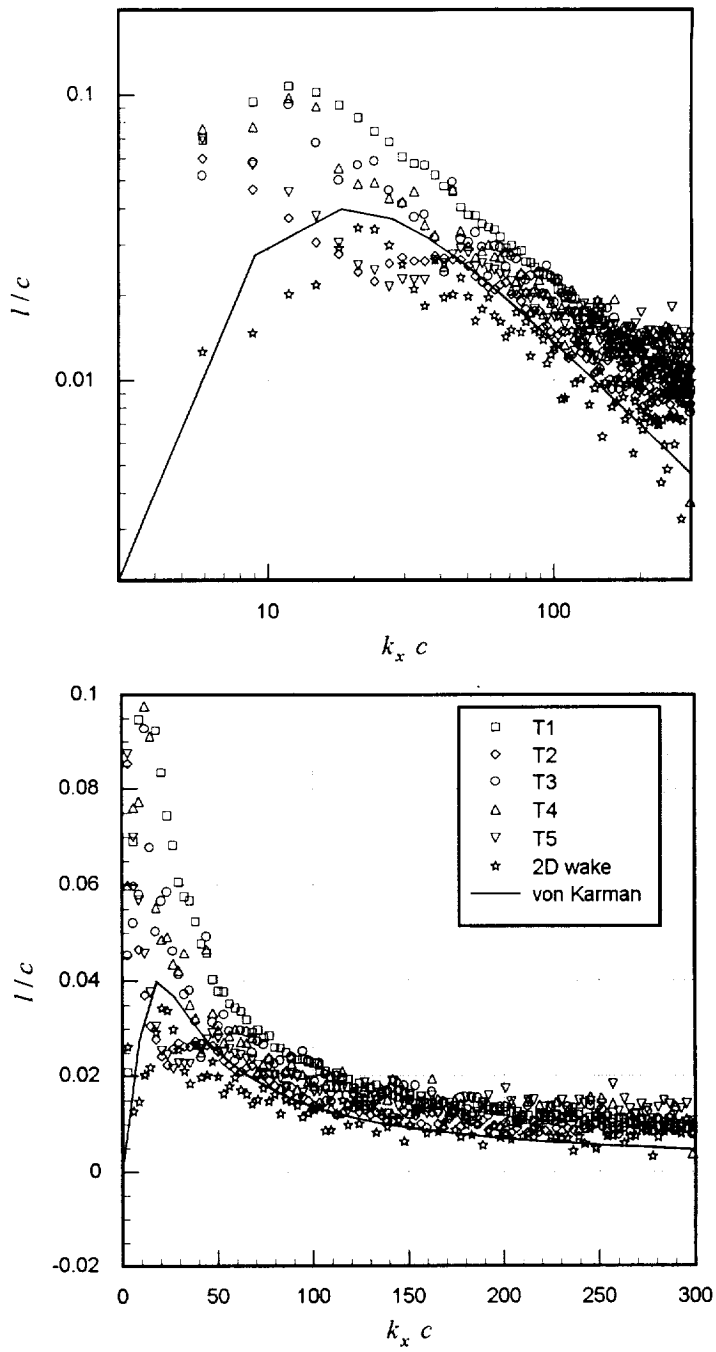

Figure 3.54: Spanwise length scale (l) of the spanwise (v) velocity component as a function of frequency

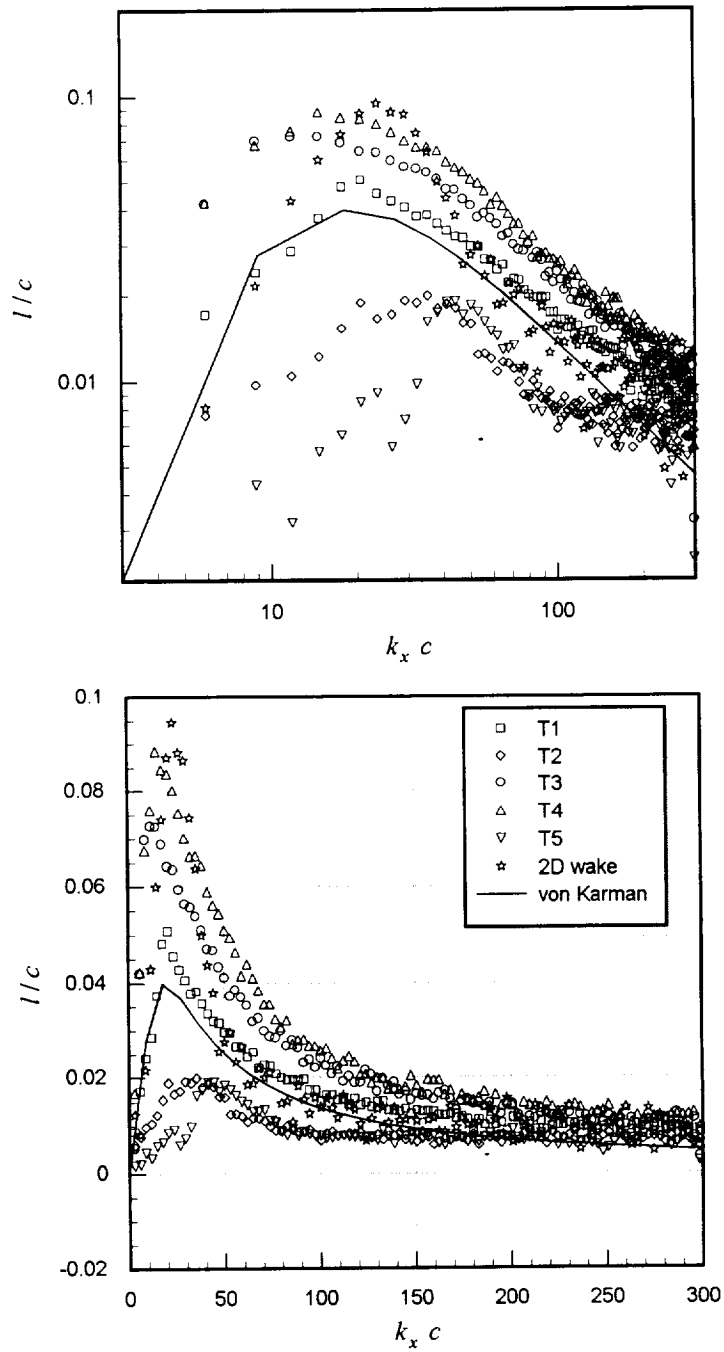

Figure 3.55: Spanwise length scale (l) of the upwash (w) velocity component as a function of frequency

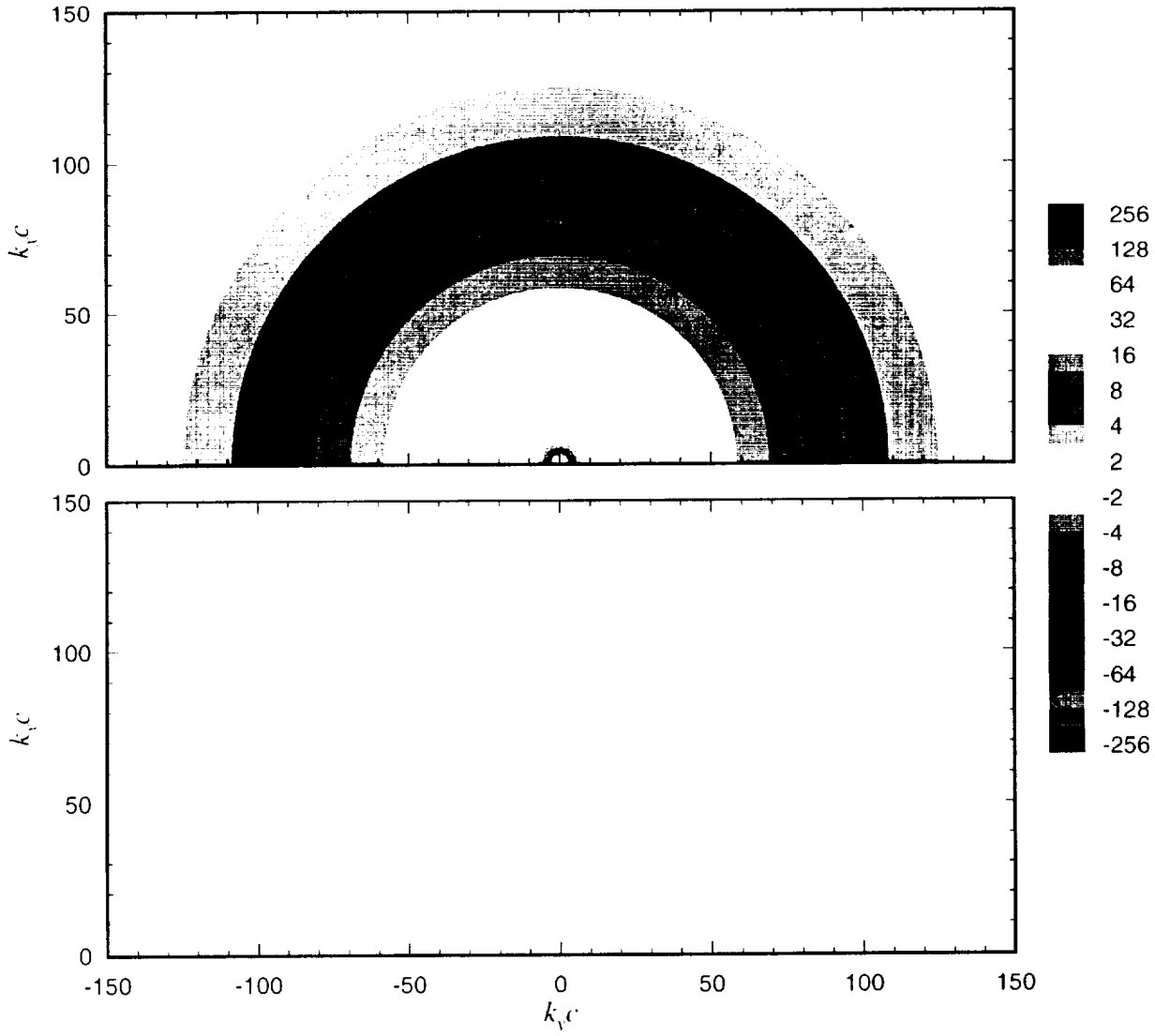

Figure 3.56: Wave-number frequency spectrum of von Karman's isotropic turbulence model. Contours of the real component of $\phi_{ww} U_\infty / (4\pi^2 c^2 \overline{w^2}) \times 10^6$ are shown at top; imaginary component on bottom.

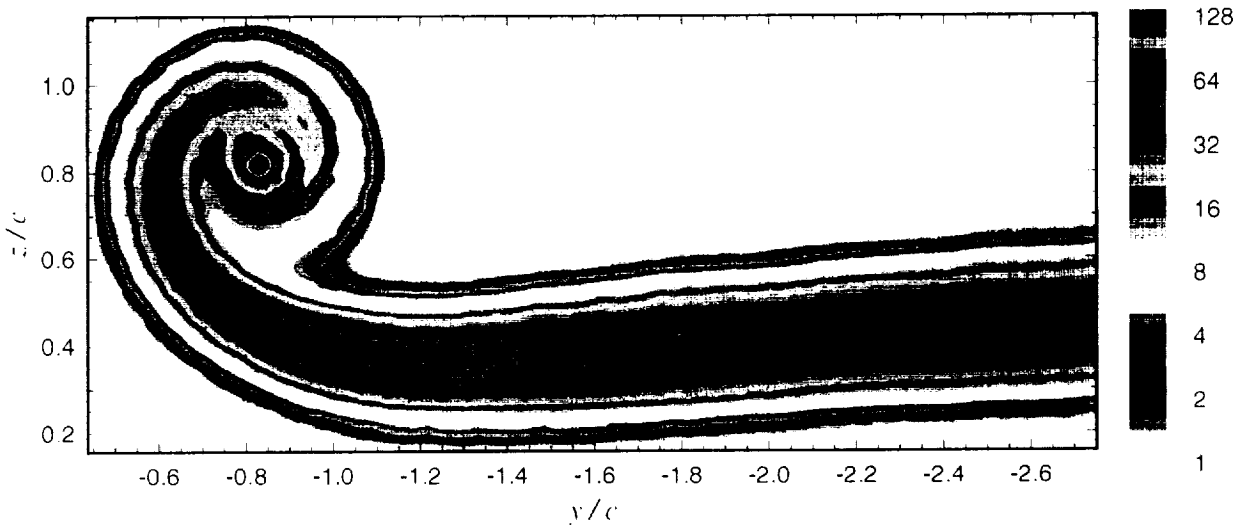

Figure 3.57: Contours of turbulence kinetic energy, $k/U_\infty^2 \times 10^5$, in the wake of a NACA 0012 blade at 5°, $x/c = 10$, $Re_c = 3.2 \times 10^5$. Data from Miranda and Devenport [25]. Two-point measurement profile in the near two-dimensional wake also shown (fixed probe location indicated by solid circle).

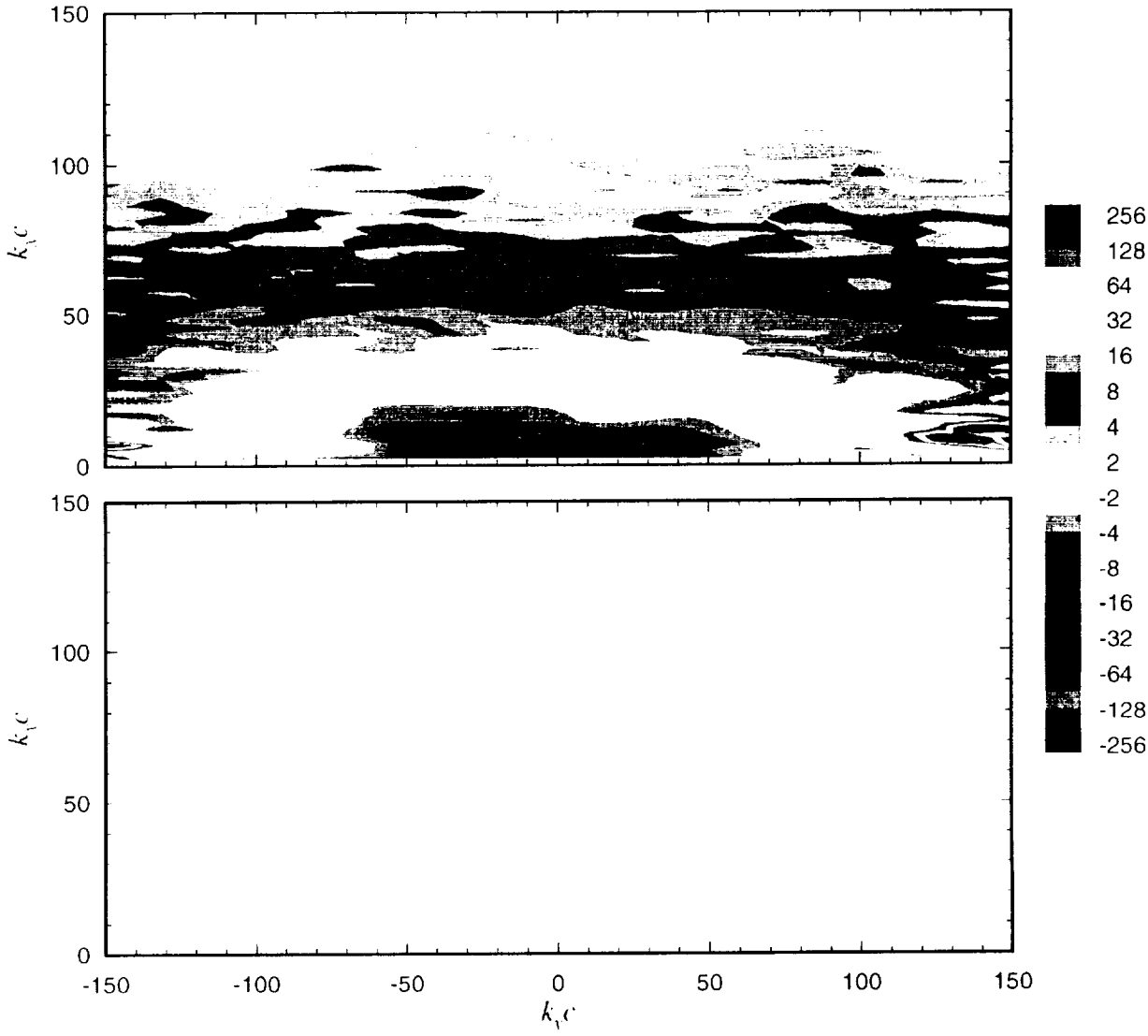

Figure 3.58: Wave-number frequency spectrum of the axial (u) velocity component measured in the two-dimensional wake of a lifting blade (see Figure 3.57). Contours are the real component of $\phi_{uu}U_\infty/(4\pi^2c^2\overline{u^2}) \times 10^6$ are shown at top. The imaginary component could not be calculated from this data set. Data from Miranda and Devenport [25].

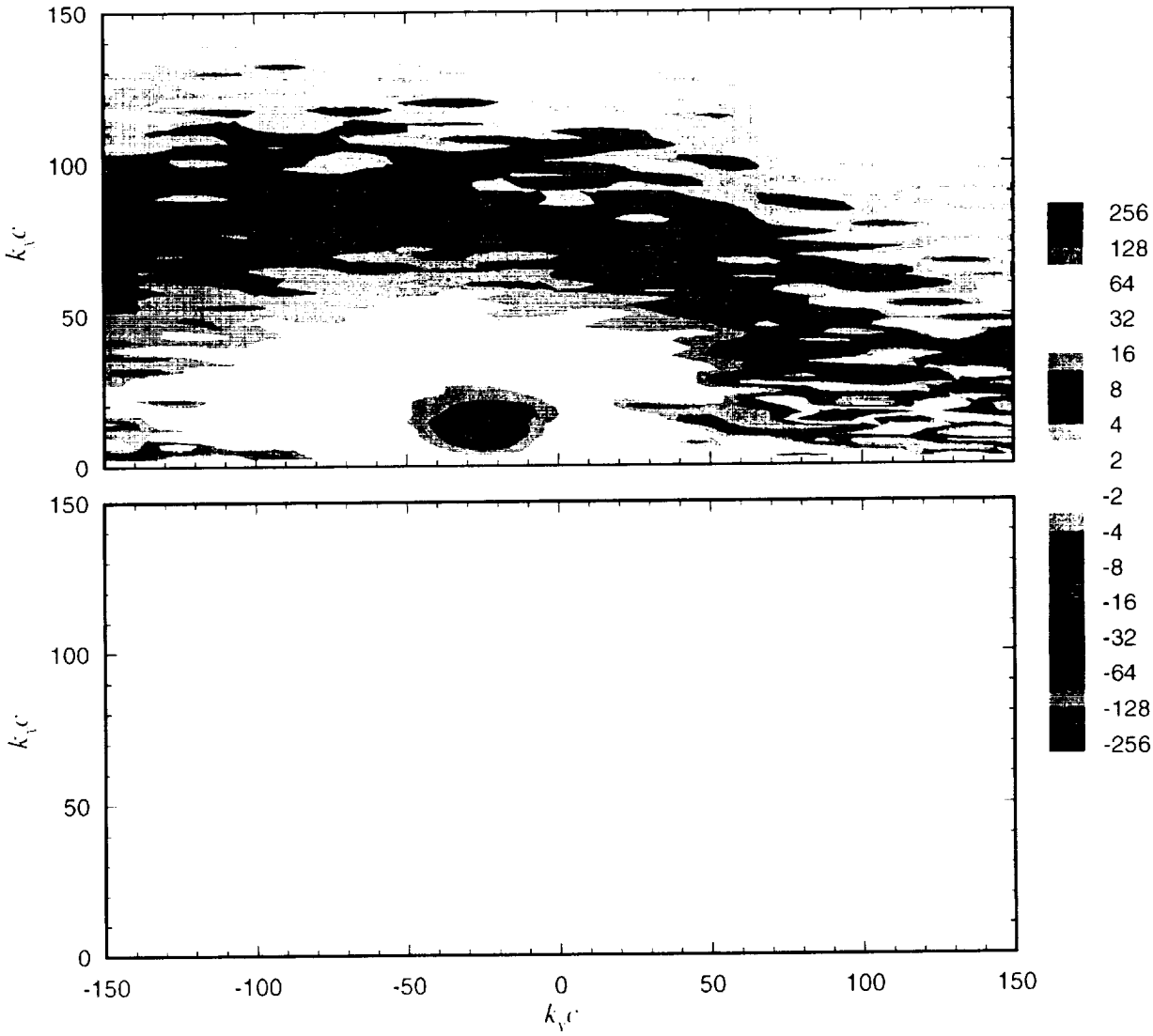

Figure 3.59: Wave-number frequency spectrum of the spanwise (v) velocity component measured in the two-dimensional wake of a lifting blade (see Figure 3.57). Contours are the real component of $\phi_{vv} U_\infty / (4\pi^2 c^2 \overline{v^2}) \times 10^6$ are shown at top. The imaginary component could not be calculated from this data set. Data from Miranda and Devenport [25].

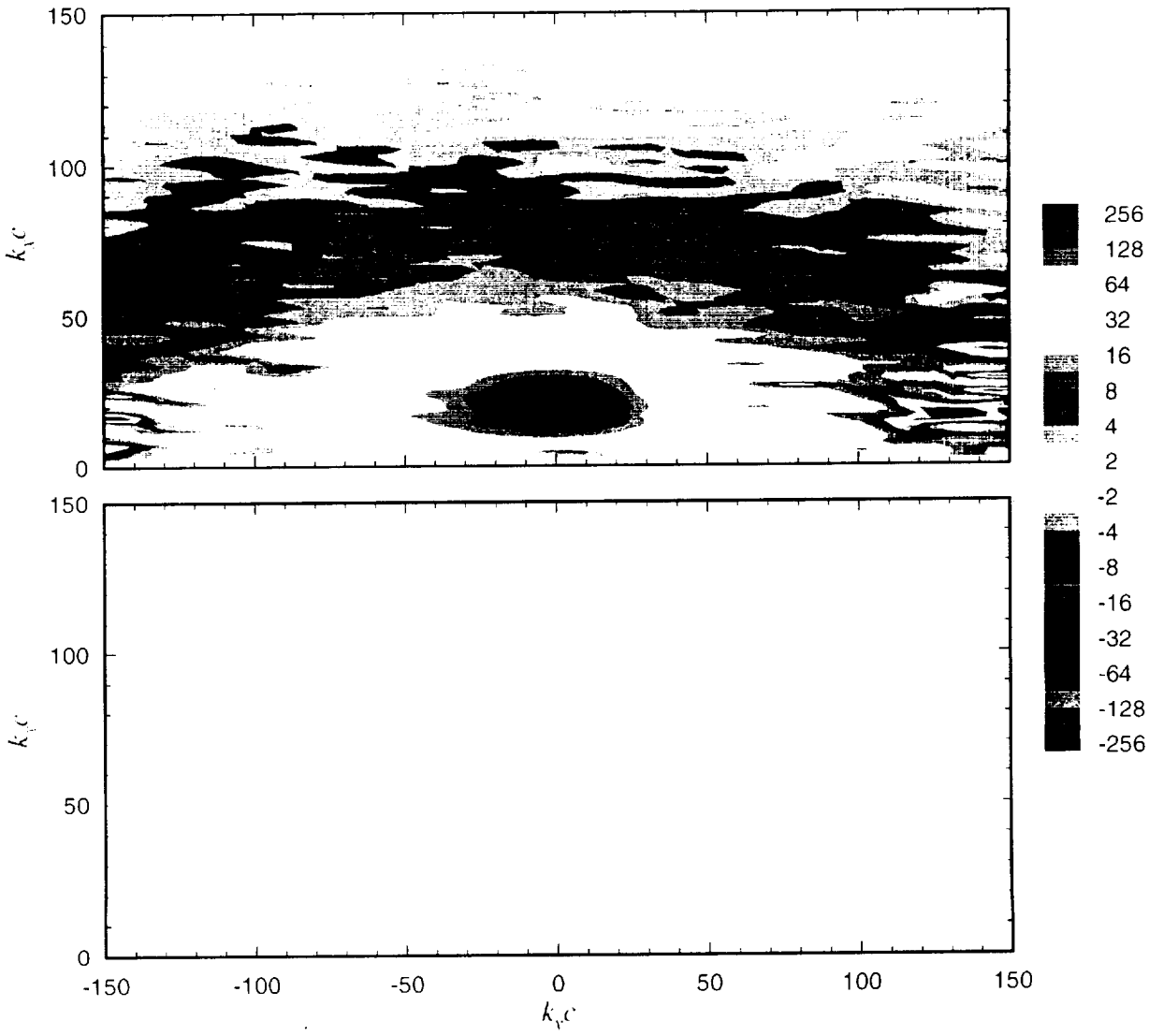

Figure 3.60: Wave-number frequency spectrum of the upwash (w) velocity component measured in the two-dimensional wake of a lifting blade (see Figure 3.57). Contours are the real component of $\phi_{ww} U_\infty / (4\pi^2 c^2 \overline{w^2}) \times 10^6$ are shown at top. The imaginary component could not be calculated from this data set. Data from Miranda and Devenport [25].

Chapter 4

Conclusions

The perpendicular interaction of a streamwise vortex with the tip of a lifting blade was studied in incompressible flow to provide information useful to the accurate prediction of helicopter rotor noise and the understanding of vortex dominated turbulent flows. The vortex passed 0.3 chord lengths to the suction side of the blade tip, providing a weak interaction. Single and two-point turbulence measurements were made using sub-miniature four sensor hot-wire probes 15 chord lengths downstream of the blade trailing edge; revealing the mean velocity and Reynolds stress tensor distributions of the turbulence, as well as its spanwise length scales as a function of frequency.

The single point measurements suggest the following flow features:

1. The flow downstream of the blade is dominated by the interaction of the original tip vortex and the vortex shed by the blade.

2. These vortices rotate about each other under their mutual induction, winding up the turbulent wakes of the blades.

3. This interaction between the vortices appears to be the source of new turbulence in their cores and in the region between them.

4. This turbulence appears to be responsible for some decay in the core of the original vortex, not seen when the blade is removed.

5. The region between the vortices is not only a region of comparatively large stresses, but also one of intense turbulence production.

6. Velocity autospectra measured near its center suggests the presence quasi-periodic large eddies with axes roughly parallel to a line joining the vortex cores.

Detailed two-point measurements were made on a series of spanwise cuts through the flow so as to reveal the turbulence scales as they would be seen along the span of an intersecting airfoil.

The measurements were made over a range of probe separations that enabled them to be analyzed not only in terms of coherence and phase spectra but also in terms of wave-number frequency (k-ω) spectra, computed by transforming the measured cross-spectra with respect to the spanwise separation of the probes. Some important results drawn from this data are as follows:

1. These data clearly show the influence of the coherent eddies in the spiral wake and the turbulent region between the cores.

2. These eddies produce distinct peaks in the upwash velocity k-ω spectra, and strong anisotropy manifested both in the decay of the k-ω spectrum at larger wave-numbers and in differences between the k-ω spectra of different components.

3. None of these features are represented in the von Karman spectrum for isotropic turbulence that is often used in broadband noise computations.

4. Wave-number frequency spectra measured in the cores appear to show some evidence that the turbulence outside sets up core waves, as has previously been hypothesized.

5. These spectra also provide for the first time a truly objective method for distinguishing velocity fluctuations produced by core wandering from other motions.

Acknowledgements

The authors would like to acknowledge the many helpful discussions with Dr. Stewart Glegg of Florida Atlantic University concerning the computation and interpretation of the wave-number frequency spectra, and length scale distributions.

Bibliography

[1] W. J. Devenport, S. A. L. Glegg, K. S. Wittmer, and M. C. Rife. Perpendicular blade vortex interaction and its implications for helicopter noise prediction. Report VPI-AOE-214, VPI&SU, Blacksburg, VA, 1994.

[2] K. S. Wittmer, W. J. Devenport, and M. C. Rife. Perpendicular blade vortex interaction. *AIAA Journal*, 33(9):1667–1674, September 1995.

[3] K. S. Wittmer and W. J. Devenport. Interaction of a streamwise vortex with a full-span blade. AIAA Paper 95-2214, June 1995.

[4] K. S. Wittmer and W. J. Devenport. Turbulence structure resulting from a perpendicular airfoil–vortex interaction. AIAA Paper 96-2014, June 1996.

[5] K. S. Wittmer. *Turbulent flowfield downstream of a perpendicular airfoil–vortex interaction.* PhD thesis, VPI&SU, Blacksburg, VA, 1996. Available at http://scholar.lib.vt.edu/theses/public/etd-31251021109643250/etd-title.html.

[6] A. J. Bilanin, M. E. Teske, and G. G. Williamson. Viscous effects in aircraft trailing vortices. NASA SP409: Wake-Vortex Minimization, 1976.

[7] A. J. Bilanin, R. S. Snedeker, and M. E. Teske. Interactions and merging of line vortices. AFOSR-TR-76-0873, 1976.

[8] S. A. Brandt and J. D. Iversen. Merging of aircraft trailing vortices. *Journal of Aircraft*, 14(12):1212–1230, 1977.

[9] A. J. Smits and R. P. Kummer. The interaction and merging of two turbulent line vortices. AIAA Paper 85-0046, January 1985.

[10] V. R. Corsiglia, V. J. Rossow, and D. L. Ciffone. Experimental study of the effect of span loading on aircraft wakes. *Journal of Aircraft*, 13(12):968–973, 1976.

[11] D. L. Ciffone. Vortex interactions in multiple vortex wakes behind aircraft. *Journal of Aircraft*, 14(6):440–446, 1977.

[12] V. R. Corsiglia, J. D. Iversen, and K. L. Orloff. Laser-velocimeter surveys of merging vortices in a wind tunnel. *Journal of Aircraft*, 15(11):762–768, 1978.

[13] J. S. Zsoldos and W. J. Devenport. An experimental investigation of interacting wing-tip vortex pairs. Report VPI-AOE-191, VPI&SU, Blacksburg, VA, 1992.

[14] J. S. Zsoldos and W. J. Devenport. An experimental investigation of interacting trailing vortex pairs. In *Proceedings of the 19th Symposium on Naval Hydrodynamics*, Seoul, South Korea, August 1992.

[15] C. M. Vogel and W. J. Devenport. The source and evolution of turbulence in trailing vortex pairs. Report VPI-AOE-217, VPI&SU, Blacksburg, VA, 1995.

[16] C. M. Vogel, W. J. Devenport, and J. S. Zsoldos. Turbulence structure of a pair of merging tip vortices, August 1995.

[17] K. Choi and R. L. Simpson. Some mean-velocity, turbulence, and unsteadiness characteristics of the VPI&SU Stability Wind Tunnel. Report VPI-AOE-161, VPI&SU, Blacksburg, VA, 1987.

[18] W. J. Devenport, S. A. L. Glegg, and G. Sharma. Turbulence measurements in trailing vortices for B.W.I. noise prediction. Report to NASA Langely under grant NAG-1-1119, 1992.

[19] L. S. G. Kovasznay. *Physical Measurements in Gas Dynamics and Combustion*, page 227. Princeton University Press, 1954.

[20] P. W. Bearman. Corrections for the effect of ambient temperature drift on hot-wire measurements in incompressible flow. *DISA Information*, (11):25–30, May 1971.

[21] J. C. Lasheras, J. S. Cho, and T. Maxworthy. On the origin and evolution of streamwise vortical structures in a plane free shear layer. *Journal of Fluid Mechanics*, 172:231–258, 1986.

[22] W. J. Devenport, M. C. Rife, S. I. Liapis, and G. J. Follin. The structure and development of a wing-tip vortex. *Journal of Fluid Mechanics*, 312:67–106, 1996.

[23] E. W. Mayer and K. G. Powell. Similarity solutions for viscous vortex cores. *Journal of Fluid Mechanics*, 238:487–507, 1992.

[24] I. Wygnanski, F. Champagne, and B. Marasli. On the large scale structures in two-dimensional small-deficit turbulent wakes. *Journal of Fluid Mechanics*, 168:31–71, 1986.

[25] J. A. Miranda and W. J. Devenport. The structure of a trailing vortex wake. Report VPI-AOE-233, VPI&SU, Blacksburg, VA, 1996.

[26] R. K. Amiet. Acoustic radiation from an airfoil in a turbulent stream. *Journal of Sound and Vibration*, 41(4):407–420, 1975.